THESIS FOR THE DEGREE OF DOCTOR OF PHILOSOPHY

Multiparametric Optical Characterization of Biological Nanoparticles using Evanescent Field Sensing

MATTIAS SJÖBERG

Department of Physics
CHALMERS UNIVERSITY OF TECHNOLOGY
Gothenburg, Sweden 2022

Multiparametric Optical Characterization of Biological Nanoparticles using Evanescent Field Sensing

MATTIAS SJÖBERG

ISBN 978-91-7905-691-9
Doktorsavhandlingar vid Chalmers tekniska högskola, Ny serie nr 5157
ISSN 0346-718X

Department of Physics
Chalmers University of Technology
SE-412 96 Göteborg
Sweden
Telephone +46(0)31-772 10 00

Printed at Chalmers Digitaltryck
Göteborg, 2022

Cover illustration: *Artistic representation of lipid nanoparticles on a supported lipid bilayer, illuminated by an evanescent field. Painting by Fredrik Höök.*

Multiparametric Optical Characterization of Biological Nanoparticles using Evanescent Field Sensing

MATTIAS SJÖBERG

Department of Physics
Chalmers University of Technology
Göteborg, Sweden 2022

Abstract

In light of the increasingly realized dependence of many biological functions on nanoscopic supramolecular assemblies, also including novel biotechnological applications, there is a need for advanced analysis methods capable of accurately quantifying different characteristics of these elusive entities. The prime aim of this thesis is the development and utilization of surface-based bioanalytical sensing methods for quantitative characterization of biological nanoparticles. The possibility to construct and use a waveguide-based evanescent light scattering microscopy instrument for investigation of various nanoparticle properties is explored through the study of liposomes and mRNA-containing lipid nanoparticles as well as polystyrene and silica nanoparticles. It is shown that through analysis of scattered light from such particles, single-particle-resolved information on their size, refractive index and interactions with surrounding protein solutions is obtainable, thus providing multiparametric characterization beyond the ensemble average. Additionally, this is combined with information gained from fluorescent labeling of certain biomolecular components, allowing nanoparticle content to be correlated with the other particle properties. The aforementioned systems were additionally investigated using a range of complementary methods, including nanoparticle tracking analysis, surface plasmon resonance sensing, and quartz crystal microbalance with dissipation monitoring. It was concluded that the waveguide microscopy method provides quantitative information in good agreement with established methods, but offers certain key advantages, such as the possibility to provide single-particle resolved label-free information on protein binding kinetics combined with simultaneous evanescent light fluorescence microscopy measurements, thus providing new insights regarding nanoparticle heterogeneity.

Keywords: Waveguide scattering microscopy, SPR, liposomes, lipid nanoparticles, protein corona, label-free, single-particle, mass quantification.

Appended papers

This thesis is based on the work contained in the following papers. The papers are referred to using their roman numerals throughout the thesis.

Paper I:

Low-temperature fabrication and characterization of a symmetric hybrid organic–inorganic slab waveguide for evanescent light microscopy

Björn Agnarsson, Mokhtar Mapar, Mattias Sjöberg, Mohammadreza Alizadehheidari and Fredrik Höök

Nano Futures 2(2), 025007. (2018).

My contribution: I was involved in the data analysis and in writing the manuscript.

Paper II:

Time-Resolved and Label-Free Evanescent-Light-Scattering Microscopy offers Mass Quantification upon Protein Binding to Single Lipid-Vesicles

Mattias Sjöberg, Björn Agnarsson, Antonius Armanious, Mokhtar Mapar, Vladimir P. Zhdanov, and Fredrik Höök.

Nano Letters, 21(11), 4622-4628. (2021).

My contribution: I was responsible for the design and planning of the experiments. I prepared the samples, performed the experiments, did the data analysis, and wrote the manuscript with input from the other authors.

Paper III:

Label-free quantification of protein binding to spherical entities using Transparent Waveguide Evanescent-Field Scattering Microscopy

Mokhtar Mapar, Mattias Sjöberg, Björn Agnarsson, Vladimir P. Zhdanov and Fredrik Höök

In manuscript.

My contribution: I was involved in experimental design, data analysis and writing the manuscript.

Paper IV:

Quantification of Refractive Index, Size, and mRNA Content of Individual Lipid Nanoparticles Using Surface-Sensitive Light-Scattering Microscopy

Mattias Sjöberg, Mokhtar Mapar, Erik Olsén, Sara Mohammadi, Petteri Parkkila, Yujia Jing, Lennart Lindfors, Björn Agnarsson, and Fredrik Höök

In manuscript.

My contribution: I was responsible for the design and planning of the experiments. I performed the experiments and data analysis, and wrote the manuscript with input from the other authors.

Paper V:

Differential Deformation of Fluid and Gel Phase Liposomes upon Multivalent Interaction with Cell Membrane Mimics Revealed using Dual Wavelength Surface Plasmon Resonance

Karin Norling*, Mattias Sjöberg*, Marta Bally, Vladimir P. Zhdanov, Nagma Parveen, Fredrik Höök

Langmuir, 38(8), 2550-2560. (2022).

My contribution: I performed some of the surface plasmon resonance measurements, took part in the sample preparation, was responsible for the data analysis and wrote parts of the manuscript. *Shared first authorship.

List of abbreviations

- **ApoE** - Apolipoprotein E
- **BNP** - Biological nanoparticle
- **CMOS** - Complementary metal oxide semiconductor
- **Cryo-TEM** - Cryogenic transmission electron microscopy
- **CTB** - Cholera toxin B subunit
- **DNA** - Deoxyribonucleic acid
- **DOPC** - 1,2-dioleoyl-*sn*-glycero-3-phosphocholine
- **DOPE** - 1,2-dioleoyl-*sn*-glycero-3-phosphoethanolamine
- **DSPE** - 1,2-distearoyl-*sn*-glycero-3-phosphoethanolamine
- **IgG** - Immunoglobulin G
- **LSPR** - Localized surface plasmon resonance
- **mRNA** - Messenger ribonucleic acid
- **MW** - Molecular weight
- **NP** - Nanoparticle
- **NTA** - Nanoparticle tracking analysis
- **PBS** - Phosphate buffered saline
- **PEG** - poly(ethylene glycol)
- **POPC** - 1-palmitoyl-2-oleoyl-*sn*-glycero-3-phosphocholine
- **QCM-D** - Quartz crystal microbalance with dissipation monitoring
- **RI** - Refractive index
- **RNA** - Ribonucleic acid
- **SBR** - Signal-background-ratio
- **siRNA** -Small interfering RNA

- **SLB** - Supported lipid bilayer
- **SNR** - Signal-noise-ratio
- **SOG** - Spin-on-glass
- **SPR** - Surface plasmon resonance
- **TIRFM** - Total internal reflection fluorescence microscopy

Contents

1

Introduction

> *"The light of the body is the eye: if therefore thine eye be sound, thy whole body shall be full of light."*
>
> — Matt 6:22

As a sound eye illuminates the whole body, sound microscopy brings light and understanding to biophysical phenomena with an intuitive quality the like of which is otherwise quite elusive. The saying *"to see is to believe"* has perhaps never been as clearly demonstrated as with the publication and wide spread of Robert Hooke's *Micrographia* in 1665[1], rich with illustrations of his microscopy observations of various biological structures in detail thitherto unseen and in which he coined the biological term *cell*. In the plethora of available instrumentation for investigating biological systems, generation of data in the form of images, as is possible with microscopy, often offers a shortcut to intuitive understanding and has since its introduction remained a central component in the scientific investigation of biological systems[2, 3].

What cannot be seen through optics does however not exclude measurements by other means. In an impressive collaborative effort, especially in the last few decades, a multitude of various biosensing technologies have emerged with the aim of application in a range of fields of immense societal importance such as diagnostics, drug development and fundamental biophysical research[4–7].

The thesis you are currently reading has in its core motivation questions on the nature and potential applicability of biological nanoparticles (NPs)[8], entities with dimensions $\lesssim 100\,\mathrm{nm}$ consisting of biological or biocompatible materials. With the goal of contributing to the ongoing effort of answering these questions, a number of technological and theoretical approaches are presented and demonstrated. In a general sense, increased understanding of biological nanoparticles brings with it potential for novel developments in prevention and treatment of disease[9]. A number of key examples of this relates to the COVID-19 pandemic, which over the last few years has been a hard lesson in the importance of understanding biological nanoparticles[10–12]. Viruses themselves fall into this category, as does a range of vaccine delivery systems used to combat viral infection[13]. The technology of lipid nanoparticles (LNPs), a relatively novel drug delivery concept which was widely implemented for COVID-19 mRNA vaccines[14, 15], is an example of the latter which figures in this thesis. There are currently considerable efforts put into widening the applicability of LNP technology and enabling its use as an increasingly general drug delivery system[16].

Another illustrative example of the importance of understanding biological NPs is the history of humanities comprehension of extracellular vesicles. After initially being considered cellular debris of limited interest, as these were eventually identified as important carriers of genetic, proteinaceous and lipidic material in the intercellular communication pathways[17, 18], a surge in method development and associated studies commenced[19]. Comprehension of the role of extracellular vesicles thus opened the door to this biological mechanism as a novel target for affecting the state of cells and their associated response, an effort constituting the principle of many drugs.

Nanoparticle-based drug delivery in general is a wide and rapidly changing field which encompasses nanosized objects both native and artificial, organic and inorganic[20, 21]. The field is vast and its main categories includes lipid-based[22, 23], polymeric[24] and metallic NPs[25, 26] to mention a few.

Successful design and choice of novel nanoparticle-based delivery systems hinges upon a number of questions, many of which relate to *surface interactions*, both in the context of entities interacting with the surface of nanoparticles (paper II, III and IV) and in the context of nanoparticles interacting with other surfaces (paper V), not least the surfaces of their intended target, often being the cytoplasmic membrane. A major topic related to the former is that of protein corona formation, the adhesion of a thin layer of biological matter to a particle exposed to in vivo environments[27] while the latter relates to, for example, transmembrane delivery through polyvalent interactions[28–30].

This thesis concerns the development and use of a number of measurement approaches for furthering our understanding of biological NP properties. One method, *waveguide evanescent light microscopy*, stands out as the main focus in a majority of the appended papers. A large portion of the thesis is thus dedicated to describing the working principles of this method, its theoretical and technological basis and theoretical models for interpreting the data it is designed to generate. In addition, this thesis work also includes the use of a number of other methods, both for stand-alone investigations or for generating complementary data to the waveguide measurements. This assortment includes ensemble average methods such as *surface plasmon resonance sensing* (SPR)[31, 32] and *quartz crystal microbalance with dissipation monitoring* (QCM-D)[33], as well as methods which, like waveguide microscopy, provide single-particle-resolved data, e.g. *nanoparticle tracking analysis* (NTA)[34].

The work presented in this thesis is summarized in five scientific papers. The main focus of papers I, III and IV is the development and demonstration of the technology of the waveguide evanescent light microscopy method, which is also the main experimental method of papers I-IV. Paper I presents a detailed protocol for manufacturing the hybrid organic–inorganic slab optical waveguide chip which is the foundation of the measurement technique. A quantitative comparison is made by observing polystyrene nanoparticles using regular epi-illumination and the scattering and fluorescence signals produced through the waveguide based evanescent light illumination.

Paper II concerns the investigation of protein binding to biotinylated lipid vesicles through waveguide microscopy with an emphasis on studying particles at an individual level, combined with SPR measurements, which provide additional information at an ensemble average level. The waveguide microscopy method provides the opportunity to simultaneously observe light emitted from fluorescently labeled proteins and changes in light scattering, i.e. a signal independent of labels, from the vesicles. It is shown that label-free single-particle-resolved scattering microscopy provides quantitative data interpretable as mass of a protein film formed on the outer surface of the vesicles, with values in good agreement with those obtained from the complementary ensemble average measurements. The nature of the scattering data, with the potential of simultaneous observation of a multitude of individual particles, allows for a signal-to-noise-ratio (SNR) increase upon data ensemble averaging comparable to the other methods but with the benefit of active background exclusion.

Paper III explores a number of modifications of the waveguide microscopy technology, including the development of a liquid handling system, an addition to the method which considerably expands the range of investigations possible with the instrument. The use of this capability is demonstrated by observing and quantifying binding of cholera-toxin B to individual glycosphingolipid $\mathrm{G_{M1}}$ modified vesicles.

Paper IV further investigates the possibilities of the waveguide evanescent light microscopy as a single-particle-resolved method as a means to elucidate heterogeneities in nanoparticle samples, in particular surface immobilized LNPs. By varying the refractive index (RI) of the surrounding solution using a new fluid exchange design, it was possible to determine the size and refractive index of individual LNPs based on their light scattering signal and to correlate this information with fluorescence signals of different labeled particle components.

Surface plasmon resonance sensing provides data on changes in refractive index near a sensor surface, which can be utilized for studying surface-bound nanoparticles in terms of adsorbed mass and sample dimensions. Both papers II and V use dual-wavelength SPR measurements for this purpose, analyzing mass of proteins bound to vesicles and thereby induced structural changes as well as potential deformation of vesicles due to interactions with an underlying supported lipid bilayer. Paper V specifically focuses on liposomal deformation upon polyvalent interactions with proteins bound to a cell membrane mimic and how this relates to the phase behavior of the liposome lipid bilayer. It is shown that this method offers the possibility to investigate and potentially disentangle the effects of nanoparticle deformation and interaction valency, effects that are expected to play an important role in cellular uptake-related process.

This thesis begins with two chapters describing the foundation of the project in terms of its biological and theoretical background. The next chapter discusses the experimental methods utilized in this work after which a chapter summarizing the five appended papers follows. With a base in the presented results, the thesis ends with concluding remarks and an outlook for possible future directions for development of the technology and its application for investigations of biological nanoparticles.

2

Biological Background

"Var dag den första — Var dag ett liv."
— Dag Hammarskjöld

THE INCREASING FUNDAMENTAL UNDERSTANDING OF life, its building blocks and the biophysical processes it involves has been accompanied by the development of successively more effective approaches and technology for treatment of disease. This vast route from humourism-inspired treatments[1], through the advent of germ theory and bacteriology all the way to the achievements of modern medicine has been marked with increasingly more advanced measurement technologies.

One of the current knowledge frontiers in life-science concerns the behavior of biological systems at the nanoscale. This relates both to nanoscopic structures native to biology as well as artificial objects originating from advancements in nanotechnology, i.e. nanobiotechnology. The maturation of this field, i.e. technology associated with structures and methods in the $\lesssim 100\,\mathrm{nm}$ diameter range, has brought with it the possibility and promise of harnessing or mimicking a vast variety of biological processes, including a range of important cellular communication pathways[36]. One of the major expressions of this advancement is the use of NPs. Particles which fall under this broad category and that have been applied in biotechnology include artificially produced organic and inorganic particles such as LNPs[15, 37], metal–organic framework-based[38] or silica-based[39] particles as well as particles already present in biological systems such as viruses, extracellular vesicles or lipoprotein particles[40–46]. Biological applications of NPs include drug delivery[21], photothermal therapy[47], diagnostics[48, 49] and biosensing[50].

Of great importance for the development and utilization of NPs for technological applications in biology is access to tools for investigating the properties that determine their function. This thesis focuses on the development, investigation and implementation of such tools, with the main focus being the waveguide evanescent light microscopy method[51].

---

[1] The outdated and misguided theory, with ancient roots, that health is governed by the internal balance of a number of fluids, or humors. Practices based on this idea, such as bloodletting as near-universal treatment, lasted well into the 1800s and the emergence of modern medicine[35].

This technology is applicable for investigating a wide range of questions for different types of NPs but also other samples such as cells. When choosing samples to investigate for exploring and demonstrating the further development of the technology in the appended papers, there is however in this thesis a focus on lipid-based nanoparticles (vesicles or LNPs). The methods and theory developed are in many ways directly applicable also to other types of samples; such as solid inorganic or metal NPs, but details in data interpretation will in many cases require some adaptation[2]. The tools presented are applied for elucidating nanoparticle properties resolved at an individual level and for investigating interactions between particles and their environment, which in this context often consists of aqueous suspensions containing biological material and biological interfaces such as mimics of the cytoplasmic membrane.

The choice of focusing on lipid-based nanoparticles in these studies was motivated by their great relevance in e.g. cell signaling and drug delivery. One of the major purposes of biologically native nanoparticles in general is that of delivery, the internal transportation of cargo[52]. As indicated above, this includes signaling pathways using e.g. extracellular vesicles and pathogenic processes induced by viruses. These particles share a function of immense interest in the context of biomimicry for medical applications, that of site-specific transmembranal delivery of otherwise immunogenic or quickly degraded entities[30, 53, 54]. Using such particles, either directly or after modifications, or particles designed to mimic their function, is thus a route for targeted delivery directly into cells of drug compounds previously very challenging to use. This includes the so-called high-molecular-weight drugs, which have come to constitute an increasing part of current medical research efforts[54–56], not least in the sub-category of nucleic acid therapeutics[57].

The following sections provide a basic review of lipidic structures of relevance to this work, including lipid vesicles and LNPs, followed by a brief introduction to other biological concepts of particular interest.

2.1 Lipids, membranes and vesicles

Lipids is a loosely defined term for a category of biomolecules soluble in non-polar solvents, whose biological function includes energy storage, signaling and to act as structural components of the cellular membrane[58]. The latter function is in large part fulfilled by the subset called *phospholipids* which generally consists of two hydrophobic fatty acid tails and a hydrophilic phosphate head-group, linked together through a glycerol moiety (see figure 2.1). The dual nature of the phospholipid components makes phospholipids *amphiphilic*, which means that while it is often energetically favorable for the hydrophilic headgroup to incorporate into the hydrogen bond network present in polar solutions such as water, this is not the case for the hydrophobic tails. This results in the spontaneous formation of a variety of lipidic structures upon placing phospholipids in an aqueous environment, the

---

[2] For instance, the optical theory for interpreting the light scattering signal from the lipid-based nanoparticles builds on assumptions which, in general, does not hold for e.g. metallic nanoparticles.

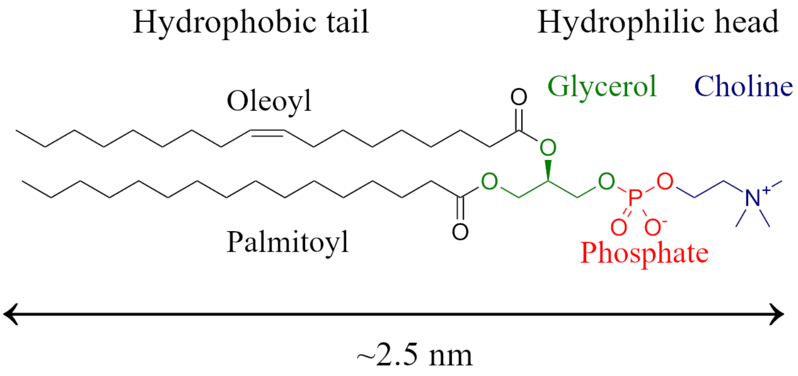

Figure 2.1: The chemical structural formula of a phospholipid, a molecule consisting of a two hydrophobic fatty acid tails and a hydrophilic phosphate group containing head. More specifically, this is 1-palmitoyl-2-oleoyl-*sn*-glycero-3-phospho-choline, abbreviated as POPC. Note the double-bond in the oleoyl tail, the presence of which makes it unsaturated; while the palmitoyl tail is saturated. The different parts are colored for clarity. In many illustrations, the head is drawn as a circle and the tails as lines (see e.g. figure 2.2).

apparent purpose of which is to hide the hydrophobic tails from the polar water molecules, usually by arrangements directing the tails against each other. Depending on a range of variables defining the physicochemical properties of the lipids, such as tail composition, length and saturation, and their environment, these structures spontaneously form micellar and bilayer enclosed vesicle particles of various shapes, sizes and lamellarity[3][58, 59], as well as surface associated structures such as the supported lipid bilayer (SLB) (see figure 2.2). Lipid vesicles[4], spherical bilayer structures enclosing a liquid core, figures abundantly in this thesis. These occur naturally and fulfill a range of roles in biology, e.g. as carriers of information in intra- and intercellular communication[60] but also serve technological roles as drug delivery vehicles[16] or for use as building blocks for forming SLBs[61].

One of many purposes of lipids is to, in combination with associated proteins, form the bilayer-structured *cellular membranes*, which make up essential components of life as we know it. By constituting a hydrophobic barrier through which different molecules and ions can be selectively translocated, the membrane allows for biological systems to be compartmentalized into regions of vastly different chemical conditions, e.g. cells and some of their indwelling organelles. The contrasts between these different compartments is of crucial importance for a multitude of biological activities. The cell membrane is highly complex both in its varying compositions and in its varying states, which in turn depend on

---

[3] Consisting of one (monolamellar) or multiple (multilamellar) bilayers. A multilamellar vesicle can thus be seen as multiple mutually concentrically enclosing vesicles.

[4] A few words on terminology; In some contexts, care is taken to distinguish between *vesicles* and *liposomes*, with the former being of natural origin and the latter artificially produced. From a characterization method perspective, this difference is of little importance and the terms are thus in this thesis used synonymously.

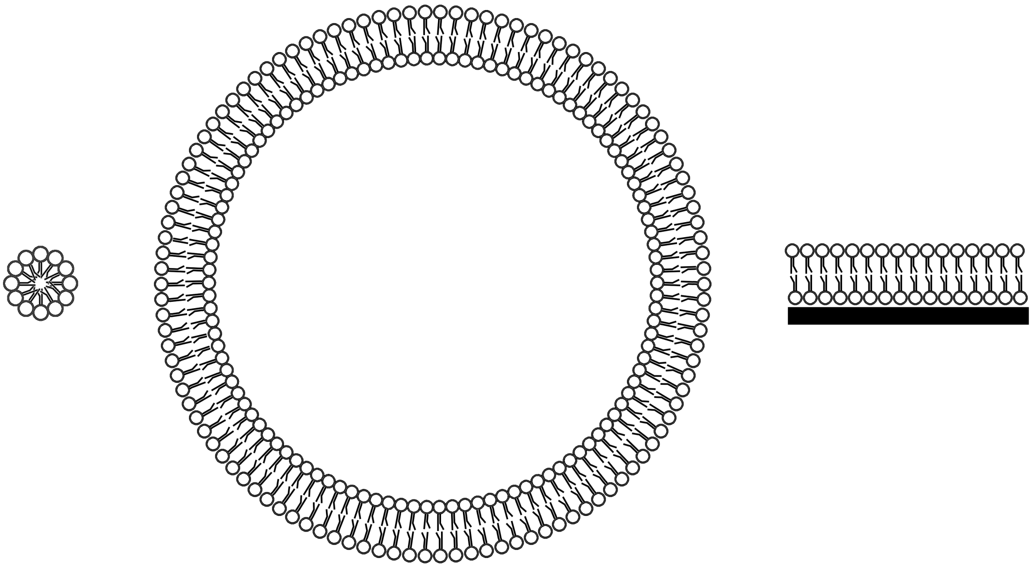

Figure 2.2: Two-dimensional illustrations of lipidic structures in the form of, from left to right: A micelle, a monolamellar vesicle and a supported lipid bilayer.

environmental factors. In many cases it can be considered a two-dimensional fluid, in which the components such as lipids and membrane proteins diffuse, forming both permanent and transient small-scale structures[52]. One of the parameters which distinguishes bilayer structures composed of different types of lipids is the temperature where it transitions between a fluid and gel phase, a process which significantly affects component mobility[62]. The temperature at which this transition occurs is mainly dependent on the strength of the Van der Waals interactions between the lipid tails in a bilayer, which in turn depends on the lipid tail length and degree of saturation.

Research aimed at understanding fundamental properties of the cellular membrane which uses surface sensitive measurement methods often use SLBs as cell membrane models[63]. Although a rather dramatic simplification compared to the natural cell membrane, it allows for controlling the sample in terms of composition and distance to the used sensor. In paper V we use this approach to investigate how the membrane fluid- and gel phases affect the interactions between vesicles and SLBs. More specifically, the interplay between interaction valency (i.e. number of ligand-receptor bonds) and vesicle rigidity (which varies with lipid phase) is investigated. Vesicles of different phase but with equal number of receptors are observed during interaction with ligand-functionalized SLBs (see figure 2.3 for an overview and section 5.5 for more details).

Many studies, including those presented in this thesis, models the cell membrane and native lipid-based structures through systems consisting of a limited number of chosen

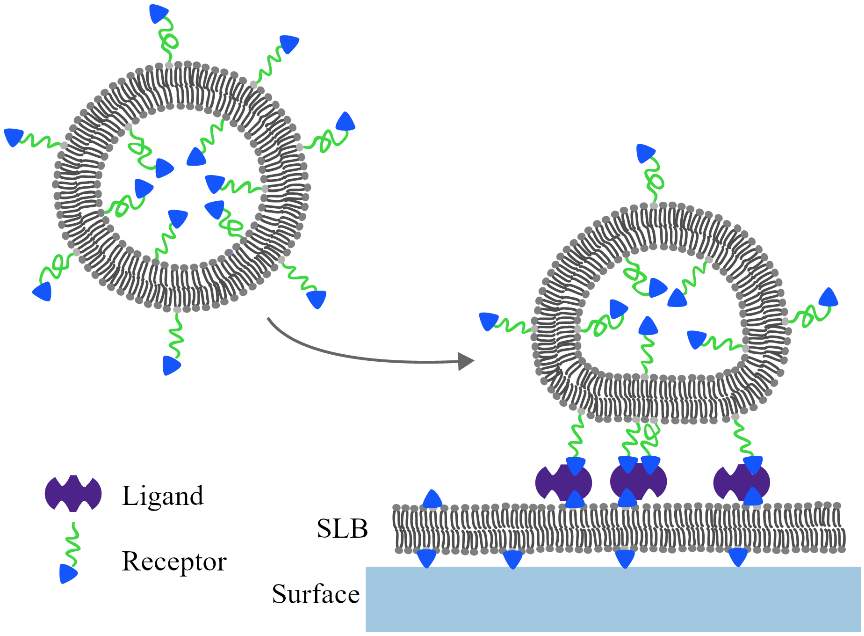

Figure 2.3: Illustration of the system under investigation in paper V. Vesicles containing receptors interact with ligands on an underlying supported lipid bilayer which causes vesicle deformation. The dependence of vesicle deformation on the vesicle lipid phase and the number of available ligands is investigated by measuring the vertical dimensions of the system (i.e. the height).

components in order to reduce complexity and disentangle specific properties and effects of interest. In this work lipid vesicles and supported lipid membranes consisting of various combinations of the lipids denoted POPC[5], DOPC[6], DSPC[7] and DSPE[8] were used (see figure 2.1 for a structural formula example), the latter lipid with the headgroup conjugated to a polyethylene glycol (PEG)-biotin group to allow for selective binding of biotin-compatible compounds.

Paper II also utilizes the concept of DNA-tethers for binding vesicles to the underlying surface. These 30 base pairs long double-stranded polymers are in one end biotinylated and in the other modified with a cholesterol moiety, which respectively can be utilized for binding to streptavidin and self-incorporating the tether into a lipid bilayer[64].

Artificial vesicles used in this work are made using established protocols[65]. The basic idea consists of generating a dry film of lipids that is subsequently hydrated, leading to the creation of vesicles of various sizes and lamellarity. When a homogeneous sample of narrow size distribution and monolamellarity is desired, the vesicles are freeze-thawed, i.e. alternatingly frozen in liquid nitrogen and thawed in a warm water bath, after which

---

[5] 1-palmitoyl-2-oleoyl-*sn*-glycero-3-phosphocholine

[6] 1,2-dioleoyl-*sn*-glycero-3-phosphocholine

[7] 1,2-distearoyl-*sn*-glycero-3-phosphocholine

[8] 1,2-Distearoyl-*sn*-glycero-3-phosphorylethanolamine

they are extruded, repeatedly pressed through a polycarbonate membrane with a defined pore size. This produces a vesicle solution of relatively homogeneous size distribution and lamellarity[66].

Because of their versatility and biocompatibility[67], vesicles have been identified as suitable for biological applications, not least that of drug delivery[53, 68, 69]. This great versatility is in part due to the amphiphilic nature of the vesicle components, which makes it possible to incorporate for delivery either hydrophobic, hydrophilic or amphiphilic compounds[68, 70]. Additionally, the structural similarities between vesicles and various biologically native structures, such as the membranes of cells and endosomes, makes these particles highly useful for applications targeting these structures. This applicability makes understanding the minute details of these systems highly desired, which in turn motivates the need for new advanced characterization methods.

2.2 Lipid nanoparticles

Another lipid-based nanoparticle delivery system of current high interest is the so called lipid nanoparticles, structures with a lipid-based core instead of the aqueous core as those characterizing lipid vesicles[9][14]. In contrast to vesicles, LNPs do not occur naturally but are specifically developed for drug delivery into cells. In general, as the intended cargo molecules become larger (e.g. proteins or nucleic acids), vesicles become less effective for encapsulation and delivery, in part due to the cargo not being able to incorporate solely into just the hydrophobic bilayer interior or the aqueous core[71]. LNPs were developed to fill this niche and build on the idea of a more direct interaction between cargo and particle constituents, often via electric charge interactions[72].

One of the important innovations that enabled LNPs as a delivery system is the use of cationic or ionizable lipids as a particle component[73]. In this context, a cationic lipid carries a permanent positive charge while an ionizable lipid is neutral at pH 7 but becomes positively charged at a decreased pH. The possibility to modulate the lipid charge of ionizable lipids and thus having them initially neutral upon injection has been found to increase biocompatibility and delivery efficiency[74, 75]. Many current LNP formulation methods thus use ionizable lipids and a low pH process step where they carry a positive charge and readily interact with negatively charged cargo, such as RNA or DNA. Besides the ionizable lipid and the cargo, LNPs additionally consist of a number of other lipid components which support particle stability and delivery efficiency[14]. For instance, DSPC and cholesterol have been shown to increase particle stability[76, 77] while PEG-lipids seem to regulate particle size and zeta-potential[78, 79] as well as preventing LNP aggregation and prolonging circulation time in vivo[80].

---

[9] The terminology is somewhat confused since vesicles are nanoparticles consisting of lipids but are not encompassed by the term *lipid nanoparticles*. In this thesis, *lipid-based nanoparticles* is used as the broad term covering both.

There are a number of methods for forming LNPs[81], including sonication, homogenization and microfluidic mixing. The latter has recently gained popularity since it loads cargo upon formation and does not require harsh post-formation loading protocols while simultaneously offering superior reproducibility[82–84].

The route LNPs and their cargo are designed to take between administration and producing a functional response in a cell is varying, complex and involves a multitude of complicated processes and details. A thorough discussion on this is beyond the scope of this thesis, and the interested reader is referred to the literature[14, 74, 85]. This text will give a very brief overview of this route, with focus on the steps which are of particular relevance for the presented results.

In order to fulfill their function of delivering nucleic acid cargo into (usually) either the cytosol or nucleus of target cells, LNPs need to overcome a number of physiological barriers. The particles must reach their intended target cells and thus need to avoid prior degradation and/or clearance[74, 75]. After reaching its target, LNPs face the barrier of cellular internalization, a process which depending on cell and particle type can occur through various mechanisms[14, 86]. These include the, so-called, endocytic pathways and commonly involves the internalized particles being taken up into the *endosomes*, dynamic intracellular vesicles that over time matures into, so called, lysosomes. During this process, where the endosomal pH gradually decreases, its contents are sorted and either delivered to various location in the cell or degraded. An internalized LNP must thus deliver its cargo out into the cytosol during this process. This is referred to as endosomal escape. The ionizable lipids of the LNPs play an important role in this process to facilitate escape, since they upon a decrease in pH become positively charged, which is intended to induce electrostatic interactions with the negatively-charged inner endosomal membrane[87].

The endosomal escape has been identified as one of the main bottlenecks in LNP mediated drug delivery. For example, it has been shown that LNPs designed for siRNA display a cargo loss of 98% between reaching a target cell and a functional response in the cytosol[88], and the loss is expected to be even higher in the case of high molecular weight mRNA[89, 90]. Since LNP delivery efficiency has been shown to be highly dependent on a range of particle parameters, such as size[87, 91], structure[92] and composition[87], it is likely that also particle heterogeneity might be a crucial part of the explanation for the low efficiency of a prepared LNP batch.

The current gold standard for LNP preparation, microfluidic mixing, can generate a reproducible mean particle size, but it is important to note that the half-width-half maximum of the size distribution is generally broad, with magnitudes approaching the mean diameter of the LNPs[78, 82, 83]. Since the average LNP size is controlled by the lipid composition, significant structural differences within individual LNP batches can be expected. Consequently, different LNPs in a single batch may display large differences in their capacity to produce a functional biological response. It can thus be speculated that the observed low delivery efficiency must not originate from all LNPs, but that certain sub-populations in an individual LNP batch are more efficient than others. The focus of paper IV is to demonstrate and use waveguide scattering microscopy to explore if it is possible to identify intra-batch particle heterogeneity through single particle-resolved multiparametric characterization.

2.3 The protein corona

Upon exposure to a complex biological solution, NPs are with few exceptions, rapidly covered by a dense layer of biomolecular compounds, often referred to as the *protein corona*[93]. This few nm thick[94], biofilm contains a subset of approximately 100-200 proteins, of which immunoglobulin G, serum albumin, fibrinogen, clusterin and apolipoproteins are especially common, as well as other biomolecules such as nucleic acids, carbohydrates and lipids[95–97]. The exact composition of a protein corona is expected to depend on a range of parameters including NP material, size, shape, charge and environmental factors such as solution composition, temperature and pH, and both the coverage and relative abundance of different types of proteins vary with time[93]. This complex variety of adherents severely complicates the utilization of biological NPs for medical purposes since it is very difficult to predict a final surface identity profile based on design criteria. In addition, there is emerging evidence for a both spatially and temporarily diverse corona e.g. the low affinity-high exchange rate *soft* and the high affinity-low exchange rate *hard* corona[98], the properties of which are far from properly understood from an application perspective. Methods for qualitative and quantitative investigation of protein binding and interaction with nanoparticle surfaces is thus an important key to improved understanding and applicability of practical usage of nanoparticles in vivo.

Two processes of particular interest which concerns the barriers prior to the endosomal escape of LNPs are PEG-shedding and protein corona formation. The latter is expected to play an important role for the binding and cellular internalization processes[93]. For instance, the presence of bound apolipoprotein E (ApoE) in the LNP protein corona has been found to enhance cellular uptake[99]. An interesting mechanism to consider in relation to LNP delivery is that of particle PEGylation. Adding PEG to the surface of an NP significantly changes its binding properties and thus its protein corona[79, 80]. In order to investigate the role of PEG, particles with lipids of different alkyl chain lengths (14 and 18 carbon molecules, respectively) were compared[100]. Formulations with the shorter lipid tails exhibited both shorter circulation times and higher delivery efficiency. It is believed that these lipids shed over time and are thus removed from the particles, a process which causes a temporally varying protein corona, initially suited for circulation and later suited for cellular uptake. From a methodological perspective it is interesting to note that these two phenomena, PEG-shedding and protein corona formation, and their correlation relates to loss and gain of particle mass. This is a process the waveguide scattering microscopy method is designed to investigate. Binding of protein to NPs is investigated this way in papers II and III and is further discussed in the Additional Results section of this thesis.

Questions related to protein corona formation have been addressed with a wide range of methods, including ensemble average methods such as dynamic light scattering[101], mass-spectrometry[102, 103] and surface sensitive methods like the quartz crystal microbalance (QCM)[104] and surface plasmon resonance (SPR) sensing[105, 106] as well as methods with single nanoparticle resolution such as cryogenic transmission electron microscopy (Cryo-TEM)[101] and flow cytometry[107]. Together, these methods offer multiparametric information with respect to protein coverage and identity, changes in NP size as well as corona-induced structural changes. Despite this fairly broad assortment of analytical methods, there is still a pronounced gap with respect to reliable methods capable of investigating the dynamics of protein-corona formation with single nanoparticle resolution, label-free readout and quantitative determination of changes in biomolecular mass.

One vision of this thesis work was to contribute a means to investigate protein-nanoparticle interactions at a single-particle-resolved level. As proof of principle, paper II presents a system of biotinylated vesicles (as described in the previous section) serving as model NPs to which the proteins *streptavidin* and *anti-biotin IgG* were bound under observation. Streptavidin is a 52.8 kDa tetrameric protein, in many ways similar to avidin, and exhibits in its affinity to biotin one of the strongest non-covalent binding interactions known in nature[108]. Anti-biotin is an immunoglobulin G antibody, of 150 kDa, binding to biotin as well. These two proteins differ in size and affinity and thus provides different situations to explore in the measurements performed. Similar results are shown in paper III for cholera-toxin B protein complex subunit (CTB) binding to G_{M1} modified vesicles. While paper IV was focused on the use of media refractive index modulation to provide multiparametric characterization of LNPs with respect to size, refractive index and cargo content, preliminary data on ApoE binding is shown in section 6.1.

3

Optical Theory

> *"As long as you are content with walks on the beach, your own glimpses are far more fun than looking at a map [of the Atlantic]. But the map is going to be of more use than walks on the beach if you want to get to America."*
>
> — C.S Lewis

EXPERIMENTS SANS THEORY tend to suffer from imprecision and excessive heuristics while theory without experiments risks ambling into the realm of speculation. In some fields of physics necessity dictates the need to live in one of these extremities, and there is undeniable value and beauty there, but physics in its most satisfactory manifestations combines both aspects in a mutually reinforcing interplay. This thesis is in essence based on experimental and analytical work, but prior to discussing methodology, a theoretical foundation must be lain.

3.1 Traveling light through optical theory

At the heart of this thesis lies a number of experimental methods whose operational principles relate to the nature of light-matter interactions. Although a full discussion on the rather intricate theoretical foundations of these phenomena is beyond the scope of this text it is both necessary and illuminating to meander through optical theory with a number of sojourns to pick up some ideas of special relevance and applicability with respect to this work. For the reader desiring more extensive theory there is a multitude of excellent literature on the subject. If you seek an overview for intuitive understanding, read Feynman[109]. For rigor, read Hecht[110, 111] and Bohren & Huffman[112]. The latter reference is especially useful for understanding the Rayleigh-Debye-Gans theory breifly discussed below. The reader interested in the theoretical details of fluorescence is referred to Lakowicz[113].

One of the main ways of approaching a discussion on the nature of light is to start with the

Maxwell equations[1]. These are often expressed as a set of coupled partial differential equations and describe the macroscopic generation and temporal evolution of electromagnetic fields. They can be expressed as follows:

$$\nabla \cdot \boldsymbol{E} = \frac{\rho}{\varepsilon} \tag{3.1}$$

$$\nabla \cdot \boldsymbol{B} = 0 \tag{3.2}$$

$$\nabla \times \boldsymbol{E} = -\frac{\partial \boldsymbol{B}}{\partial t} \tag{3.3}$$

$$\nabla \times \boldsymbol{B} = \mu\Big(\boldsymbol{J} + \varepsilon \frac{\partial \boldsymbol{E}}{\partial t}\Big) \tag{3.4}$$

Here, $\boldsymbol{E}$ is the electric field, $\boldsymbol{B}$ the magnetic field, $\boldsymbol{J}$ the electric current density, ρ the free charge density, t time, $\varepsilon = \varepsilon_0 \varepsilon_\mathrm{r}$ the permittivity and $\mu = \mu_0 \mu_\mathrm{r}$ the permeability[2]. ε_0 and μ_0 are the electric and magnetic constants and ε_r and μ_r the relative permittivity and permeability. $\boldsymbol{J}$ relates to electrical conductivity, σ, as $\boldsymbol{J} = \sigma \boldsymbol{E}$.

These four equations, together with the Lorentz force law, which describes the electromagnetic force $\boldsymbol{F}$ exerted on a point charge of charge q and velocity $\boldsymbol{v}$:

$$\boldsymbol{F} = q(\boldsymbol{E} + \boldsymbol{v} \times \boldsymbol{B}), \tag{3.5}$$

form the foundation of classical electromagnetic theory.

A consequence of the nature of the electromagnetic fields, as became evident with the formulation of the Maxwell equations, is the possibility and existence of self-perpetuating electromagnetic waves; a varying electric field will generate a magnetic field and vice versa. Hidden in this system of equations one can thus suspect the presence of a wave equation, which is indeed the case. In free space, in the absence of sources and currents (i.e. $\rho = \boldsymbol{J} = 0$) taking the curl of equation (3.3) and utilizing the vector identity $\nabla \times (\nabla \times \boldsymbol{E}) = \nabla(\nabla \cdot \boldsymbol{E}) - \nabla^2 \boldsymbol{E}$ results in a homogeneous wave equation:

$$\nabla^2 \boldsymbol{E} = \varepsilon\mu \frac{\partial^2 \boldsymbol{E}}{\partial t^2} \tag{3.6}$$

This equation describes an electromagnetic wave propagating in space with the phase velocity $1/\sqrt{\varepsilon\mu}$. One of the remarkable discoveries of Maxwell as he formulated these equations is that ε and μ, constants describing the electromagnetic field properties in specific media, combined this way coincided precisely with the experimentally determined speed of light, $c = 1/\sqrt{\varepsilon\mu}$. The important conclusion was that light itself is in fact an

---

[1] Alternative approaches usually begin either in antecedent wave propagation theory or later developed quantum theory.

[2] For an isotropic medium, μ and ε are scalars. For anisotropic media, they are instead tensors.

electromagnetic wave. Two physical phenomena, previously considered separate, had been elegantly unified.

A well known set of solutions to the Maxwell equations which satisfies the wave equation and from which, through superposition, all other solutions can be formed, are plane waves[110]:

$$\boldsymbol{E} = \boldsymbol{E}_0 e^{-i\boldsymbol{k}\cdot\boldsymbol{x} - i\omega t} \tag{3.7}$$

where ω is the field angular frequency, $|\boldsymbol{E}| = E_0$ is the amplitude and $\boldsymbol{k} = \boldsymbol{k'} + i\boldsymbol{k''}$ is the complex wave vector which describes the wave spatial frequency, direction of propagation and attenuation, with $|\boldsymbol{k}| = 2\pi/\lambda$ and λ the light wavelength.

Analogue to the above reasoning the magnetic field can be similarly expressed as:

$$\boldsymbol{B} = \boldsymbol{B}_0 e^{-i\boldsymbol{k}\cdot\boldsymbol{x} - i\omega t} \tag{3.8}$$

Considering the equations (3.3) and (3.4) for this plane wave gives:

$$\boldsymbol{k} \times \boldsymbol{E}_0 = \omega \boldsymbol{B}_0 \tag{3.9}$$

$$\boldsymbol{k} \times \boldsymbol{B}_0 = -\omega\varepsilon\mu \boldsymbol{E}_0 \tag{3.10}$$

These equations reveal the fact that electromagnetic radiation consists of an electric and a magnetic field, both perpendicular to each other as well as to the direction of propagation $\boldsymbol{k}/|\boldsymbol{k}|$.

The plane wave solutions additionally allow the reformulation of the wave equation (3.6) as:

$$\nabla^2 \boldsymbol{E} + \varepsilon\mu\omega^2 \boldsymbol{E} = 0 \tag{3.11}$$

or

$$\nabla^2 \boldsymbol{E} + \boldsymbol{k}^2 \boldsymbol{E} = 0 \tag{3.12}$$

This time-independent expression of the wave equation, known as the Helmholtz equation is, as we shall see, very useful when discussing phenomena of interest for this thesis.

3.2 Light and matter

Explaining physical phenomena often comes down to choice of explanatory model. What is unreasonably simplistic in one context is perfectly suitable in another. Realizing what to neglect and what to include in a model is crucial for producing intuitive understanding. For the purposes of the following discussion, matter can be modeled as a collection of discrete charges existing in a world of classical physics. In a material subjected to an electromagnetic wave, its free charges will be driven into oscillatory motion. As seen in the Maxwell equations this generates further oscillating electromagnetic fields, otherwise known as secondary radiation or *scattered* light[112]. A number of phenomena usually not thought of as scattering can be understood through this model. As atoms are subjected to an electric field, the negatively charged electrons and the positively charged nuclei are driven out of positional equilibrium due to the field induced generation of an oppositely directed force[3]. It can be thought of as the electrons being attached to the nuclei with a spring and thus acting as driven damped oscillators. They will, in other words, act as a dipole antennas and thus elastically absorb and emit electromagnetic radiation as *dipole scatterers*. Matter subjected to light, oscillating electromagnetic fields, thus acts as a collection of oscillating charges which themselves generates oscillating fields. In other words, they will radiate electromagnetic energy; scatter light. The force a single electron in a material is subjected to is thus the combined effect of the incoming electric field and what is generated from all other electrons. The interactions of these coupled oscillators, making up matter, thus boils down to a rather complicated electromagnetic many-body problem whose solutions describe a wide range of phenomena such as specular and diffuse reflection, diffraction by slits and gratings and refraction between different media[112].

The above background provides a framework for the following discussion of three concepts of particular interest for this work: refractive index, dielectric media and Rayleigh-Gans-Debye (RGD) scattering theory[112].

3.3 Refractive index and dielectric media

At this point the time is come to introduce one of the central concepts of this thesis, the *refractive index*. This material property is defined as the ratio between the in vacuo speed of light and its medium phase velocity. This in media phase velocity change can be derived as a direct result of the above discussed electromagnetic model. The combination of an incoming field and the scattered light it induces in a material is manifested as an apparent decrease in phase velocity[112]. Besides this, there are a number of intricacies to this parameter upon which many methods and results rely.

Building upon section 3.1, an interesting result is obtained by taking the cross product of $\boldsymbol{k}$ with equation 3.9.

$$\boldsymbol{k} \times (\boldsymbol{k} \times \boldsymbol{E}_0) = \omega \boldsymbol{k} \times \boldsymbol{B}_0 = -\omega^2 \varepsilon \mu \boldsymbol{E}_0 \tag{3.13}$$

---

[3] Note that it is primarily the electrons that move due to their lower mass.

This, through the previously introduced useful vector identity, gives:

$$\boldsymbol{k} \cdot \boldsymbol{k} = \omega^2 \varepsilon \mu \tag{3.14}$$

and thus an expression for $\boldsymbol{k}$:

$$|\boldsymbol{k}| = \omega\sqrt{\varepsilon\mu} = \frac{\omega}{c}\sqrt{\varepsilon_r \mu_r} = \frac{\omega}{c}N \tag{3.15}$$

With N being the complex refractive index of the medium in which the wave is propagating.

$$N = \frac{c}{\omega}(k' + ik'') = \sqrt{\varepsilon_r \mu_r} = \sqrt{\frac{\varepsilon\mu}{\varepsilon_0 \mu_0}} = n + i\kappa \tag{3.16}$$

where the real part $\Re(N) = n$ is commonly referred to as the refractive index whereas $\Im(N) = \kappa$ is a parameter governing attenuation. The latter is evident when considering the $-i\boldsymbol{k} \cdot \boldsymbol{x}$-term in the field expression exponents (e.g. equations 3.7 and 3.8), where the imaginary part of $\boldsymbol{k}$ produces a negative exponent and thus spatially decaying fields.

Many materials, including those of interest in this thesis, are practically non-magnetic and consequently have a relative permeability μ_r close to unity. In these cases the refractive index can be approximated as $\sqrt{\varepsilon_r}$. One convenient route to comprehension of N is thus to understand the ε_r-parameter, the relative permittivity of a material.

The reader is hence encouraged to recall the features of the relative permittivity as it thus translates to N and is of high importance in the following context. In the case of a dielectric material, by definition where $\boldsymbol{k'} \gg \boldsymbol{k''}$, the complex relative permittivity, $\varepsilon_r(\lambda) = \varepsilon'(\lambda) - i\varepsilon''(\lambda)$ is a wavelength dependent quantity whose real part is a measure of the material electric polarizability, the extent to which the material is polarized upon exposure to an electric field, while its imaginary part describes the attenuation of electric fields passing through the material, the latter often manifested as *absorption* of light. ε' thus describes how much the material electrons are displaced from equilibrium to counteract the applied field; the spring constant in the above analogy of electronic springs. A higher refractive index does consequently, besides the decreased light phase velocity, denote weaker internal electric fields.

In the case of dielectric solutions, the refractive index relates to the convenient relation referred to as the *refractive index increment*, $\partial n/\partial c$, which highlights its dependence on solute mass concentration. The fact that the refractive index increment is near constant in a wide concentration range for biological compounds, such as proteins and phospholipids, has promoted thorough investigation and tabulation of its material specific values[114]. This can accordingly be utilized for calculating protein film surface mass concentration, Γ, through the, so called, de Feijter's formula:

$$\mathit{\Gamma} = \frac{\Delta d_{\mathrm{p}}(n_{\mathrm{p}} - n_{\mathrm{m}})}{\partial n/\partial c} \tag{3.17}$$

where n_{p} and n_{m} are the refractive indices of the protein film and the bulk solution, respectively, and d_{p} the protein film thickness[115].

It has been shown that the refractive index increment of protein can, with great accuracy, be predicted based on its constituent amino acid composition[114]. The expression uses the mass weighted average values (referred to with subscript i) of two known amino acid specific parameters, refraction per gram R_{a} and specific volume $\bar{\nu}_{\mathrm{a}}$ (i.e inverse density), expressed as follows[114]:

$$R_i = \frac{\sum_{\mathrm{a}} R_{\mathrm{a}} M_{\mathrm{a}}}{\sum_{\mathrm{a}} M_{\mathrm{a}}} \tag{3.18}$$

$$\bar{\nu}_i = \frac{\sum_{\mathrm{a}} \bar{\nu}_{\mathrm{a}} M_{\mathrm{a}}}{\sum_{\mathrm{a}} M_{\mathrm{a}}} \tag{3.19}$$

where M_{a} is the amino acid molar mass.

These parameters relate to the protein refractive index as

$$n_{\mathrm{p}} = \sqrt{\frac{2R_i + \bar{\nu}_i}{\bar{\nu}_i - R_i}} \tag{3.20}$$

which in turn relates to the refractive index increment as

$$\partial n/\partial c = \frac{3}{2}\bar{\nu}_i n_0 \frac{n_{\mathrm{p}}^2 - n_0^2}{n_{\mathrm{p}}^2 + 2n_0^2} \tag{3.21}$$

with n_0 being the refractive index of the solution[114]. This relation is utilized in paper II to calculate protein refractive index.

3.4 Waveguide theory

A phenomenon of immense use in biophysical research is that of a, so called, *evanescent field* for illumination of near-surface nanoscopic objects. When a propagating electromagnetic wave encounters an interface with a discrete decrease in refractive index, e.g. light passing from glass to water or water to air; *total internal reflection*, the reflection of all incoming energy, occurs above a certain critical incident angle[110]. This angle can be found through Snells law,

$$n_1 \sin\theta_1 = n_2 \sin\theta_2, \tag{3.22}$$

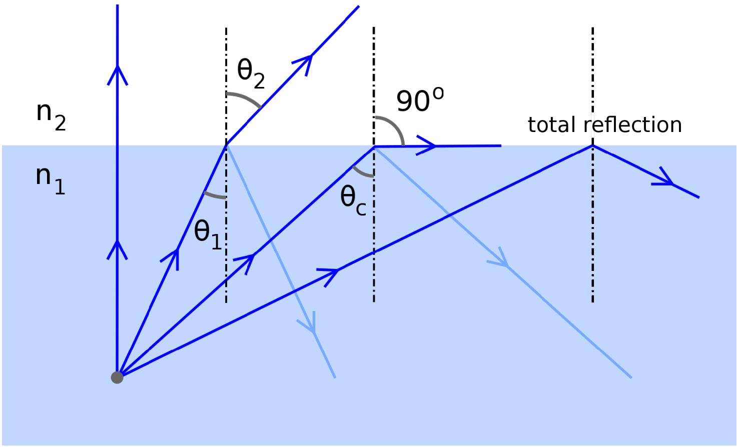

Figure 3.1: The phenomenon of total reflection, which occurs above a critical angle θ_c for light incident on an interface to a medium of higher refractive index.

which relates the angles of incidence, θ_1, and refraction, θ_2, at an interface, to the refractive indices of the two materials, n_1 and n_2. With $n_1 > n_2$ there will be a critical incidence angle θ_c above which θ_2 exceeds $90°$ and all light is reflected (see figure 3.1).

Total reflection of light is however not a discrete phenomenon but is a far-field consequence of the incident light inducing charge oscillations which under these conditions interact to have destructive interference in the forward direction. While this indeed results in total reflection in the far-field, the oscillating charges actually produce a local near-field, a propagating field along the interface which decays exponentially with orthogonal distance from the interface, the evanescent field. This thin field of light, which in common practical microscopy setups has a penetration depth of a few hundred nanometers, is conveniently utilized for illumination of surface bound entities e.g. in total internal reflection fluorescence microscopy (TIRFM)[116] (see sections 3.6 and 4.1.1). One of the main motivations for utilizing this type of illumination scheme is that by solely illuminating near-surface entities, signals stemming from the bulk are minimized.

Another technological approach to generate and use an evanescent field is the use of a structure consisting of adjacent slabs of materials of different refractive indices, a planar waveguide. Figure 3.2 shows an illustration of the relevant situation, highlighting the *waveguide core* (of refractive index n_2) sandwiched in-between layers of lower refractive index material (n_1) referred to as the *cladding* layers. Light propagating in the x-direction in the core in this situation can be approximated as a plane wave according to equation 3.7 (assuming a thin waveguide core, and thus solely a single guided mode), but noting that the materials extending semi-infinitely in the z-direction allows for the expression of the time-independent electric field independently of this dimension, i.e.:

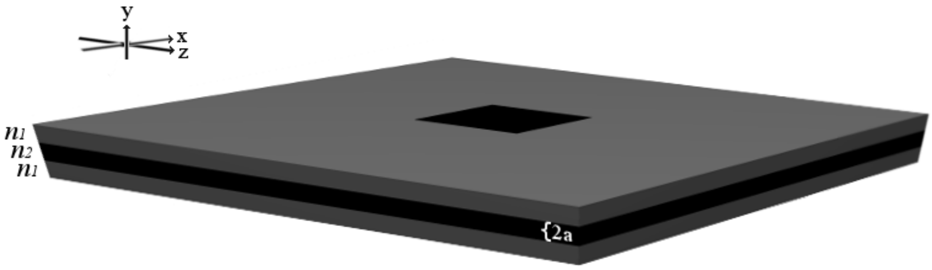

Figure 3.2: Illustration of a waveguide chip as used in papers I and II. A (black) core layer of refractive index n_2 is enveloped by the (grey) cladding layers of refractive index n_1. Confinement of light in the core is possible if $n_2 > n_1$. Note that this image is not to scale and that the core and cladding layers having a thickness of approximately 0.4 µm and 3 µm, respectively; deposited on a ∼ 500 µm silicon wafer. The core thickness is here defined as $2a$, with the y-coordinate zero being placed in its center.

$$\boldsymbol{E}(\boldsymbol{r}) = \boldsymbol{E}(y)e^{-i\beta x}, \tag{3.23}$$

where $\beta = k_0 n_{\text{eff}}$ is the wavenumber of light traveling in the waveguide in the x-direction, with n_{eff} being an effective refractive index of the waveguide structure.

This expression in combination with equation (3.12) gives:

$$\frac{\partial^2 \boldsymbol{E}}{\partial y^2} + (k^2 - \beta^2)\boldsymbol{E} = 0. \tag{3.24}$$

With $n_2 > n_1$, the $(k^2 - \beta^2)$-factor will be positive for the core and negative for the cladding. This results in equation (3.24) having the following solutions:

$$E = \begin{cases} A\cos(a\sqrt{k^2 n_1^2 - \beta^2} - \varphi)e^{-\sqrt{\beta^2 - k^2 n_2^2}(y-a)} & y > a \\ A\cos(x\sqrt{k^2 n_1^2 - \beta^2} - \varphi) & -a < y < a \\ A\cos(a\sqrt{k^2 n_1^2 - \beta^2} + \varphi)e^{\sqrt{\beta^2 - k^2 n_2^2}(y+a)} & y < -a \end{cases} \tag{3.25}$$

where a is half the thickness of the core layer; A is a constant that can be derived from the boundary condition of the electric field and φ a phase term[117]. Depending on a, n_1, n_2 and the boundary conditions due to the geometry of a certain waveguide, there can be one or multiple values of β which satisfy the above expressions. These denote the multiple discrete bound modes supported by the waveguide. The geometry and material properties for the waveguide structure used in this thesis is chosen such that a single mode is supported for the light wavelengths used.

Consideration of these equations reveal a propagating field in the waveguide core and the exponentially decaying evanescent fields in the cladding layers. A convenient quantitative characterization of these types of decaying fields is that of a decay length or penetration depth, δ, defined as the distance where the field magnitude has decreased with a factor of $1/e$ (or, equivalently, where the intensity of the field has decreased with a factor $1/e^2$):[4]

$$\delta = \frac{1}{\sqrt{\beta^2 - k_{\text{cladding}}^2}} = \frac{\lambda_0}{2\pi\sqrt{n_{\text{eff}}^2 - n_1^2}} \tag{3.26}$$

Paper I-IV use a waveguide microscopy platform for investigation of surface bound nanoparticles. It consists of a silica core ($n_2 = 1.42$) enveloped in cladding layers of the fluorinated polymer material CYTOP ($n_1 = 1.34$). With 488 nm TE-polarized light and a core thickness of 450 nm, this results in a decay length of $\sim 200\,\text{nm}$. Details of the experimental setup is found in section 4.1.

3.5 Scattering of light by dielectric nanoparticles

Scattering of light, the excitation of charge oscillations and consequent elastic[5] reemission of electromagnetic radiation due to refractive index contrasts, is rigorously described through the Maxwell equations[112]. However, a thorough phenomenological discussion of scattering using this foundation directly risks distracting from the special cases of interest in this work, namely scattering of light by dielectric nanoparticles in the $\sim 50 - 200\,\text{nm}$ diameter range as discussed in paper I-IV.

3.5.1 Rayleigh scattering

An appropriate starting point for the modeling of this special case is the scattering intensity of an infinitesimal oscillating dipole, which can be expressed as[118]:

$$\boldsymbol{I}_{\text{s}} = |\alpha|^2 \frac{\pi^2 c |\boldsymbol{E}|^2}{2\varepsilon_s \lambda^4} \left(\frac{\sin\theta}{r'}\right)^2 \hat{\boldsymbol{r}} \tag{3.27}$$

where α is the particle polarizability, c the in media speed of light, λ the incident light wavelength[6], $\boldsymbol{E}$ the applied electric field, ε_s the relative permittivity of the scattering object, $\hat{\boldsymbol{r}}$ a unit vector and r' and θ being spherical coordinates. The $\sin\theta$-factor describes

---

[4] A consequence of this definition is that the distance at which the intensity has decreased by a factor $1/e$ is half the distance at which the field has decreased by $1/e$.

[5] I.e. where the kinetic energy is conserved.

[6] The λ^4-factor here is of fame as being the main explanation for why molecules scattering light in our atmosphere make it look blue[119].

the apparent dipole moment dependence on the angle of observation. Depending on experimental setup, it is necessary to integrate over an appropriate angle range to find correct values, i.e. considering just the light reaching the camera used to observe the scattering object. For the purposes of discussing light scattering microscopy as used in this thesis, where nanoparticles are observed using the same illumination in the same microscope geometry, all factors except α can be considered a constant, A, and the expression simplified to

$$I_{\mathrm{s}}^{0} = A\left|\alpha\right|^{2}, \tag{3.28}$$

where the superscript "0" indicates the infinitesimal dipole approximation, i.e. that we do not yet consider and correct for effects due to particle size.

Assuming an object to behave as an infinitesimal scattering dipole does, together with the assumption of a refractive index close to 1, produce the premises for the Rayleigh scattering model[110], which was developed in the 1800s[120]. Particles in this size and refractive index range (basically, non-metallic particles with a size $\sim 1/10$ of the light wavelength) can be considered small enough to have a negligible internal phase shift. In other words, it is assumed that the incident field, although changing over time, is uniform over the particle volume, and thus that all induced charge oscillations in a particle are in phase.

Understanding the relative scattering intensity of particles in the Rayleigh regime is thus a question of expressing their polarizability α. For a spherical solid particle of radius r and permittivity ε_s, in a medium of permittivity ε_{m} this is[112]:

$$\alpha = 4\pi r^3 \frac{\varepsilon_s - \varepsilon_{\mathrm{m}}}{\varepsilon_s + 2\varepsilon_{\mathrm{m}}} \tag{3.29}$$

Expressing the polarizability of particles of more complex structure and geometry, for instance optically inhomogeneous and non-spherical particles, is in most cases difficult. See Bohren & Hoffman[112] chapter 5 for an instructional derivation of the polarizability of a coated ellipsoid. Beyond the few analytically solvable cases it is common to utilize effective medium approximations[121].

An important case to consider in the context of this thesis is that of a coated sphere, i.e. a core of permittivity ε_1 surrounded by a spherical shell of permittivity ε_2, in a medium of permittivity ε_{m}. With a total radius r, the polarizability for this structure is expressed as:

$$\alpha = 4\pi r^3 \frac{(\varepsilon_2 - \varepsilon_{\mathrm{m}})(\varepsilon_1 + 2\varepsilon_2) + \varphi(\varepsilon_1 - \varepsilon_2)(\varepsilon_{\mathrm{m}} + 2\varepsilon_2)}{(\varepsilon_2 + 2\varepsilon_{\mathrm{m}})(\varepsilon_1 + 2\varepsilon_2) + \varphi(2\varepsilon_2 - 2\varepsilon_{\mathrm{m}})(\varepsilon_1 - \varepsilon_2)} \tag{3.30}$$

where φ is the fraction of the particle volume occupied by the core.

In paper II, this expression is adapted for the case of a lipid vesicle (with polarizability α_v), modeled as a hollow sphere (consisting of a lipid bilayer of thickness Δ_l and permittivity ε_l). In this case the core and the medium have the same permittivity ($\varepsilon_1 = \varepsilon_\mathrm{m}$) and the above expression becomes:

$$\alpha_\mathrm{v} = 4\pi r^3 \frac{(2\varepsilon_\mathrm{l} + \varepsilon_\mathrm{m})(\varepsilon_\mathrm{l} - \varepsilon_\mathrm{m})(1-\varphi)}{(\varepsilon_\mathrm{l} + 2\varepsilon_\mathrm{m})(\varepsilon_\mathrm{l} + \varepsilon_\mathrm{m}) - 2(\varepsilon_\mathrm{l} - \varepsilon_\mathrm{m})^2\varphi} \tag{3.31}$$

where $\varphi = (r - \Delta_\mathrm{l})^3/r^3$. Since the bilayer is thin compared with the dimension of the vesicle, $\Delta_\mathrm{l} \gg r$, we can use the approximations $1-\varphi = 3\Delta_\mathrm{l}/r$ and $\varphi = 1$ in the numerator and denominator, respectively. This yields:

$$\alpha_\mathrm{v} = \frac{4\pi r^2 \Delta_\mathrm{l}(2\varepsilon_\mathrm{l} + \varepsilon_\mathrm{m})(\varepsilon_\mathrm{l} - \varepsilon_\mathrm{m})}{3\varepsilon_\mathrm{l}\varepsilon_\mathrm{m}} \tag{3.32}$$

When considering the case of proteins binding to a vesicle, the particle can be viewed as a two-shell system, where to the lipid bilayer an external shell of thickness Δ_p and permittivity ε_p is added. Still under the assumption of small shell thicknesses in comparison with the vesicle radius r, the two shells can be replaced by one effective shell with the thickness

$$\Delta_\mathrm{lp} = \Delta_\mathrm{l} + \Delta_\mathrm{p} \tag{3.33}$$

and permittivity

$$\varepsilon_\mathrm{lp} = \frac{\varepsilon_\mathrm{l}\Delta_\mathrm{l} + \varepsilon_\mathrm{p}\Delta_\mathrm{p}}{\Delta_\mathrm{l} + \Delta_\mathrm{p}} \tag{3.34}$$

Consequently, the vesicle protein complex has a polarizability of

$$\alpha_\mathrm{v,p} = \frac{4\pi r^2 \Delta_\mathrm{lp}(2\varepsilon_\mathrm{lp} + \varepsilon_\mathrm{m})(\varepsilon_\mathrm{lp} - \varepsilon_\mathrm{m})}{3\varepsilon_\mathrm{lp}\varepsilon_\mathrm{m}} \tag{3.35}$$

The ratio of scattering intensity increase to initial scattering intensity, can be expressed

$$\frac{\Delta I_\mathrm{s}}{I_0} = \frac{I_\mathrm{s}(\alpha_\mathrm{v,p}) - I_\mathrm{s}(\alpha_\mathrm{v})}{I_\mathrm{s}(\alpha_\mathrm{v})} = \frac{\alpha_\mathrm{v,p}^2 - \alpha_\mathrm{v}^2}{\alpha_\mathrm{v}^2} \tag{3.36}$$

Measuring this scattering intensity ratio thus provides, through equations 3.32, 3.35 and 3.36, a relation between the thicknesses and permittivities of the protein layer and lipid bilayer which to the first order approximation is independent of vesicle size. As demonstrated in this expression, considering an intensity ratio rather than absolute intenisty values allows for eliminating the A-factor of equation 3.28. This approach is used in paper II and III to quantify protein adsorption to vesicles.

3.5.2 Phase and evanescence

When waveguide scattering microscopy is used for observing particles with a size that approaches the excitation light wavelength, we leave the regime of Rayleigh scattering and need to take two additional phenomena into account: i) phase effects and ii) the exponential decay of the evanescent field. For particles in the size and RI regime of interest here[7], the phase effects are considered using, so called, Rayleigh-Gans-Debye (RGD) theory. In this approximation, a particle is considered a collection of volume elements which all act as independent dipole scatterers. By integrating over the particle volume, the particle shape and interference between its parts are accounted for. This approach can be combined with an exponentially decaying illumination field, which both affects the scattering intensity directly, but also how the magnitude of the RGD correction varies over the particle. We can express the scattering intensity as:

$$I_{\mathrm{s}} = I_{\mathrm{s}}^{0} \eta_{s}, \tag{3.37}$$

with I_{s}^{0} from equation 3.28 and η_s being a being dimensionless correction factor accounting for these effects. η_s for a particle can be calculated by integrating over its volume:

$$\eta_s = \left| \int \frac{\mathrm{d}V}{V} e^{-z/\delta} e^{i\varphi} \right|^2, \tag{3.38}$$

where V is the particle volume, z is the vertical coordinate, i.e. height over the sensor surface, δ the evanescent field decay length and $e^{i\varphi}$ a factor relating the phase of each volume element to its position with respect to a chosen reference point. This is generally a tricky integral to solve. It has, however, been shown that the two phenomena represented in this correction factor can to a good approximation be treated independently[123], i.e.:

$$\eta_s = \eta_{\mathrm{ev.s}} \eta_{\mathrm{RGD}} = \left| \int \frac{\mathrm{d}V}{V} e^{-z/\delta} \int \frac{\mathrm{d}V}{V} e^{i\varphi} \right|^2, \tag{3.39}$$

---

[7] The limits are set by the assumption underlying RGD theory that the phase of each scattering element is determined solely by its position in relation to the illumination, and not by phase retardation or other effects (e.g. excitation of plasmons, as in plasmonic particles) due to the material properties of the particle surrounding it. The element thus acts as if the rest of the particle were not there. This puts restrictions on both RI and size. The assumptions for applying RGD theory can be expressed mathematically as $|m-1| \ll 1$ and $ka|m-1| \ll 1$, where m is the particle-medium RI ratio, k the light wavenumber and a the largest dimension of an object. The former inequality means the incident field is not considerably disturbed by the particle, and the latter inequality that the phase difference in the particle relative to the medium can be neglected. See chapter 8 in [122].

where $\eta_{ev.s}$ and η_{RGD} account for the exponentially decaying evanescent field and phase shifts according to Rayleigh-Gans-Debye theory, respectively. Solving these integrals for a solid sphere geometry gives:

$$\eta_{\mathrm{ev.s}} = 9\Big(\frac{2\delta}{r_0}\Big)^6 e^{-r_0/\delta}\Big[\frac{r_0}{2\delta}\cosh\big(\frac{r_0}{2\delta}\big) - \sinh\big(\frac{r_0}{2\delta}\big)\Big]^2, \tag{3.40}$$

where r_0 is the particle radius (see paper III for details), and:

$$\eta_{\mathrm{RGD}} = \Big|\frac{3}{u^3}[\sin(u) - u\cos(u)]\Big|^2, u = \big(\frac{2\pi n_{\mathrm{m}}}{\lambda_0}\big) r_0 \sin\big(\frac{\vartheta}{2}\big), \tag{3.41}$$

where λ_0 is the vacuum wavelength of the light and ϑ the angle between the incident and scattered light[122]. When considering equation 3.41, it is worth noting that for an increasing particle radius this factor will eventually reach a maximum after which its contribution to the total signal will be negative. The effect is wavelength dependent but will for visible light be of significance as particle diameters approaches a few 100s of nm. Consequently, interpreting a specific scattering intensity in terms of particle size will for certain size regimes be ambiguous (see figure S6 in the Supporting Information of paper III for an illustration of this effect).

These correction factors have also been solved for hollow spheres, which is useful when considering lipid vesicles. The results can be found in paper III and in the supporting information of ref. [123].

3.6 Fluorescence

The use of the fluorescence as a tool for the investigation of biological structures and processes is well established[113]. The waveguide microscopy method utilized in paper I-IV benefits from the possibility of combining its scattering microscopy capabilities with that of the more traditional fluorescence microscopy-based investigations.

The method is typically based on the use of *fluorescent labels*, entities which can bind to analytes of interest and which upon absorption of light in a certain spectral range, emit photons of a (usually) increased wavelength[113]. This allows, as in the case of the waveguide microscopy setup described in section 4.1, for the decoupling of the incident and emitted light and thus the selective visualization of labeled objects. The concept is usually explained through the use of a Jablonski diagram, see figure 3.3 where electronic and vibrational state transitions in a fluorescent molecule are shown and photon absorption and emission are highlighted[8].

---

[8] Note that we are now leaving classical optics and are considering a phenomenon understood through quantum physics.

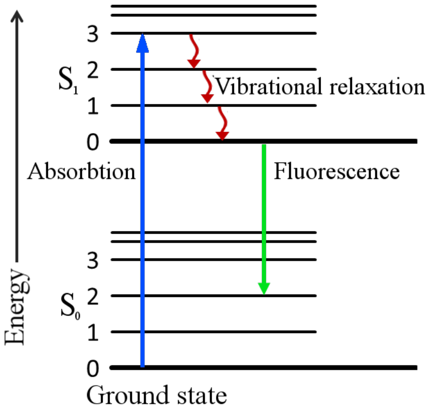

Figure 3.3: The concept of fluorescence illustrated through a Jablonski diagram. An example of the fluorescence process is shown, where excitation of an electron from its ground state S_0 to its first excited singlet state, S_1, through the absorption of a photon and subsequent non-radiative vibrational relaxation (phononic loss of energy) leads to the emission of a photon of increased wavelength (i.e. of less energy). The difference in wavelength between incident and emitted light can be utilized through optical filtering for highly sensitive observation of fluorescing objects.

It is also worth mentioning that the highly reactive nature of fluorophores in their excited state results in the phenomenon of *photobleaching*, where a fluorophore has a certain probability of suffering a photochemical alteration that permanently makes it non-fluorescent. This is often manifested as a fluorescence signal decrease over time, an effect which puts temporal limits on experiments utilizing fluorophores[113].

The fluorescence intensity of a labeled object scales with the number of fluorophores (disregarding quenching effects, i.e. fluorescence decrease due to a number of phenomena, many which relate to interactions with other nearby entities[113]). This is an important point when comparing a signal based on fluorescence emission with a light scattering signal of the same sample. The scattering signal instead scales with the square of the polarizability (see equations 3.30, 3.36).

The fact that an emitted fluorescence signal is incoherent[9] means that phase related effects as discussed for the scattering signal does not occur (i.e. there is no correction factor like η_{RGD} for the fluorescence signal). This fact additionally results in a slightly different expression for the correction factor accounting for the evanescent field decay, $\eta_{\mathrm{ev,f}}$:

$$\eta_{\mathrm{ev.f}} = 3\left(\frac{\delta}{r_0}\right)^3 e^{-r_0/\delta}\left[\frac{r_0}{\delta}\cosh\left(\frac{r_0}{\delta}\right) - \sinh\left(\frac{r_0}{\delta}\right)\right]. \tag{3.42}$$

---

[9] Phase related effects such as an interference related signal decrease require coherent light, i.e. that the frequency and waveform are identical and the phase difference constant. The time scale (nanoseconds) over which fluorescence absorption and emission occurs is large enough for environmental interactions to remove any phase correlation between individual fluorophores and thus any net effects due to interference.

4

Experimental Methods

> *"There is a crack in everything,*
> *that's how the light gets in."*
> — Leonard Cohen

Practical investigation, understanding and utilization of physical phenomena require, in most cases, experimental measurements in order to gain necessary information and more often than not, hard-obtained quantitative information is desired. This thesis work focuses on the use of a number of methods and their combination, to investigate the properties and behavior of biological nanoscopic objects. A distinction to keep in mind is that of measurements providing single-particle resolved information, such as waveguide scattering microscopy and nanoparticle tracking analysis (NTA), and that of ensemble average methods, such as SPR and QCM-D, whose signals exclusively originates from multiple particles. This section will provide information on the principles of the main experimental methods utilized in this work.

4.1 Waveguide microscopy

The main method in use for the characterization of individual nanoparticles utilized here builds on the use of evanescent field illumination through waveguide microscopy, as theoretically outlined in section 3.4. The use of evanescence for this purpose in its currently most popular implementation, total internal reflection fluorescence (TIRF) microscopy, was pioneered by Axelrod in the 1980s[124]. The rapidly decaying evanescent field provides a means to limit the illumination to the volume $\sim 200\,\mathrm{nm}$ above a surface, thus providing a resolution beyond the depth-of-focus-limitation of other methods such as standard epi-illumination microscopy. TIRF has been used extensively to examine interaction between cells and surfaces, making use of the methods palpable reduction in background from cell and debris autofluorescence[125]. TIRF has also been combined with fluorescence photobleaching recovery and correlation spectroscopy to measure the binding rates and surface diffusion constants upon fluorescently labeled serum protein binding[126, 127].

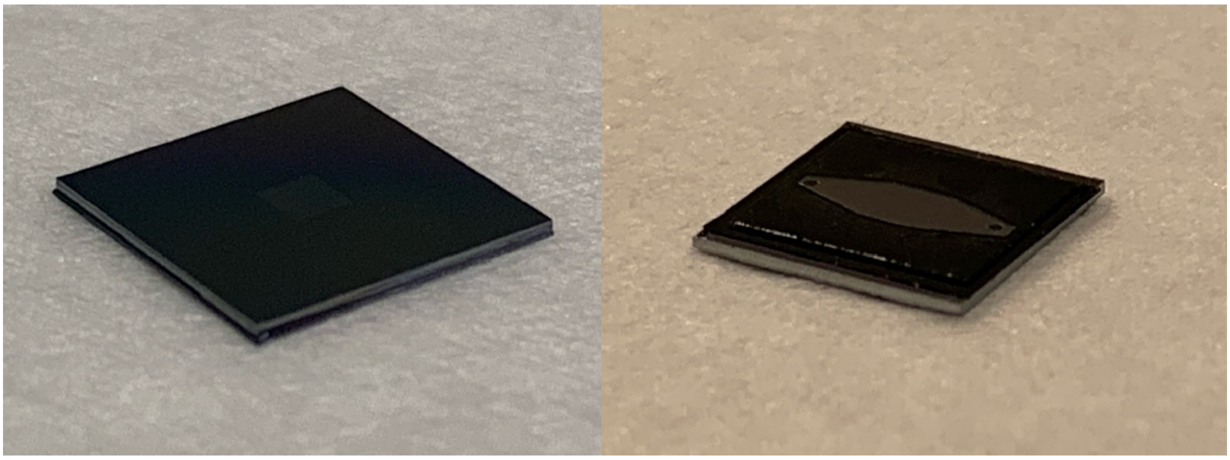

Figure 4.1: Picture of the waveguide chips used in this work. The chips have an area of $1 \times 1\,\text{cm}^2$. The left image shows the open chip configuration, with square well design. The well is covered by a droplet of sample to which a water immersion objective is connected. The right image shows a chip designed for use with the Nanolyze$^{\text{TM}}$ fluid exchange system. Two hole have been etched through the chip for the inlet and outlet connections, and a glass slide has been attached on top of the well using double-sided tape to create an enclosed compartment through which sample can be pumped.

Waveguide microscopy shares many similarities with this method in terms of the use of the rapidly decaying evanescent field for sample illumination. Developed in the 1990s and initially demonstrated for thin film characterization[128, 129], the method was later implemented for biological applications[130] and has today been used in a variety of setups. These include fluorescence microscopy approaches[131], transparent chip platforms[132], dSTORM and ESI super-resolution fluorescence microscopy[133], multimode scattering microscopy using high core-cladding RI contrast[134] and incoherent white light source illumination[135]. The term *waveguide microscopy* also covers methods of quite different geometries than in these works, including optical fiber based approaches[136, 137].

The basic structure of the waveguide chip used in this thesis consists of a silicon substrate on which a lower cladding, core and upper cladding layer have been sequentially deposited. A single chip (see figure 4.1) consists of a $1 \times 1\,\text{cm}^2$ square of this assembly with a well etched through the top cladding layer, reaching the waveguide core and thus an excited evanescent field at its interface. The field is generated through laser illumination by an optical fiber but-coupled to the waveguide core layer from a chip facet. This illumination setup features an orthogonal relation between the illumination and observation direction, i.e. illumination from the side and observation from above or below.

In order to minimize stray light scattering, which as discussed in section 3.2 is a consequence of refractive index contrasts, the cladding consists of CYTOP, a fluorinated polymer material which has the convenient property of a refractive index of 1.34[138] (i.e. n_1 in figure 3.2 and equation 3.25), thus closely matching that of water. The cladding envelops a core of silica, in the form of spin-on-glass, with a refractive index of 1.42 (i.e. n_2). In fact, to utilize silica as a core in a waveguide chip, which is convenient from the perspective of using well established surface modifications as well as SLB formation, the cladding must have a refractive index lower than that of the core. CYTOP fulfills also this criteria.

A waveguide scattering measurement setup, as implemented in papers I and II, is shown in figure 4.2. A water immersion objective is connected to a droplet of buffer placed in the waveguide well, enabling the observation of objects emitting light due to the generated evanescent field on the well bottom. This entails light emitted due to fluorescence excitation and emission, in a manner analogue to that of TIRF microscopy, but also scattered light due to a refractive index contrast between an object and the surrounding medium. The penetration depth of the waveguide system, which defines its sensing range extending from the core, is determined by the refractive indices and thicknesses of the core and cladding layers, the illumination wavelength and polarization, and can be tuned from below 100 nm to well above a micron[139], while regular TIRF usually exhibits 100-200 nm values. The implementation used in this thesis shows a penetration depth of approximately 100 nm.

Although the waveguide design used in papers I and II worked adequately for situations involving experiments over short time spans and of a limited number of different sample solutions, it did not allow for measurements where thorough or rapid exchange of liquids was required. As measurements were carried out directly in a droplet exposed to the environment, issues arose due to the droplet evaporating over time which changed both the sample concentration and the optical properties of the setup. To mitigate this problem, microfluidic flow structures were built into the waveguide chip allowing for a more stable setup and a much easier way of liquid exchange (see papers III and IV, as well as section 4.1.3).

4.1.1 Waveguide microscopy among other methods

The persistent high interest in questions regarding nanoparticles and relating technology has resulted in a vast space of approaches for nanoparticle characterization. Many of these cover different areas and applications and can often be considered complementary. When it comes to optical characterization methods, many challenges stem from the fact that nanoparticles are small and thus generally produce a weak signal. For instance, as seen in section 3.5.1, the light scattering signal from a dielectric nanoparticle is roughly proportional to the particle volume squared[1]. This means that development of technology for optical observation and investigation of nanoscopic objects is focused on the question of generating contrast, the possibility of distinguishing a weak particle signal from its background. One of the key approaches to this is that of fluorescence microscopy, where the contrast originates from the spectral separation of the illumination and emitted signal, i.e. that the emitted signal and the illumination are of different wavelengths (see section

---

[1] Reducing the diameter of a sphere 10 times thus reduces its scattering signal by a factor of 10^6.

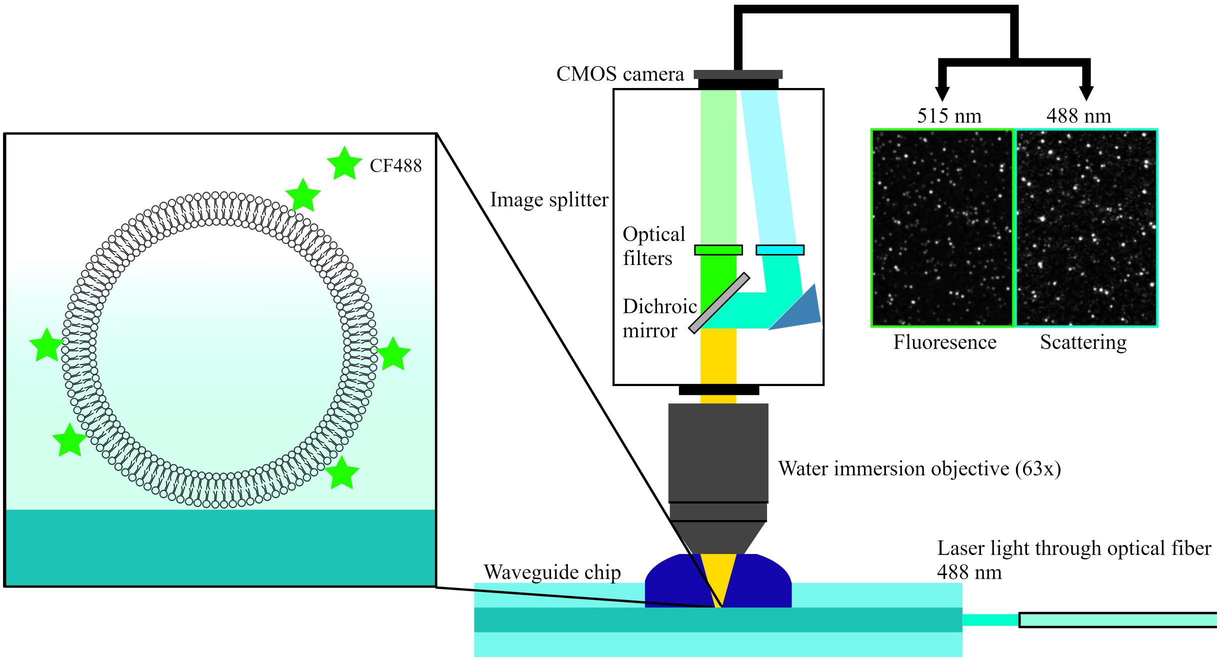

Figure 4.2: Illustration of the basic principle of a waveguide evanescent light measurement. TE polarized laser light of a certain chosen wavelength, here 488 nm, is but-coupled from an optical fiber to the waveguide core in which a propagating field, and outside of which an exponentially decaying evanescent field, is generated. A droplet of solution which constitutes the experimental environment and contains analytes of interest has been placed in the waveguide well which provides access to the evanescent field on the core surface. A vesicle partially consisting of fluorescently labeled lipids (CF488 labels) is found inside the evanescent field, which causes it to scatter light of 488 nm and fluoresce at approximately 515 nm. This light passes through an objective immersed in the solution droplet and subsequently through an image splitter which separates the two signals which are subsequently projected onto a CMOS camera.

3.6). The background can thus be efficiently suppressed by using appropriate optical filters. While very useful, fluorescence microscopy carries a number of limitations, as it requires samples which are either inherently fluorescent or labeled with fluorescent tags. Inherent to the method is thus that one only observes what one has labeled and that other components of a sample do not produce a signal. Additionally, the introduction of fluorescent molecules to a sample might require complicated chemical procedures and both these procedures and the physicochemical properties of the molecules themselves risks affecting the sample. For instance, as discussed in paper IV, these tags can often carry charge and be of similar size as the objects of interest (in this case, the lipids in LNPs). Quantitative interpretation of a fluorescence signal is also complicated as it often requires accounting for phenomena such as photobleaching and quenching[124].

Waveguide microscopy as a means for (biological) nanoparticle characterization exists in this context as a method specifically designed for single-particle-resolved, label-free and quantitative investigations. It is worth noting that such information can also be obtained through total internal reflection scattering microscopy, a method which shares the use of evanescent light illumination with waveguide microscopy. Although mainly used exclusively as a fluorescence microscopy method, there exist a number of approaches for suppressing the background from the illumination and thereby observing also the light scattered of a sample. Examples of this include dark-field TIR using a perforated mirror to separate the scattered light from the illumination[140, 141], or bright field TIR through the use of a number of noise reduction methods in the optical setup[142]. Compared to waveguide microscopy, TIR scattering microscopy has a significantly smaller range over which the evanescent field depth can be tailored and is limited by having a relatively small area of homogeneous illumination. It also usually requires the use of a more complicated and expensive optical setup, both in terms of TIR-enabling objectives and optics required for background suppression[143].

The capacity of these methods to investigate individual nanoparticles sets them apart from methods solely producing ensemble average data (e.g. QCM-D or SPR). The possibility to generate information from the scattering signal of nanoparticles distinguishes the method from those requiring particle labeling. As shown in the appended papers, it is however possible to still utilize fluorescent labels to gain additional information on the investigated particles. To the extent theoretical models can sufficiently well represent the nature of light scattering, the method is also quantitative and can thus be used to not only detect the presence of a sample, but to produce data on its properties (e.g., as in the appended papers: size, refractive index or temporal changes in bound mass).

A principle to keep in mind when comparing methods is that the light scattering signal is, to a first approximation, a function of both particle size and refractive index and that separation and measurement of the two requires a signal complementary to the scattering intensity. In this thesis (more specifically, in paper IV), this complement is obtained by inspecting how the signal varies as a function of medium refractive index. A number of other methods instead use the movement of particles for this purpose, an approach with other advantages and disadvantages to consider. In order to gain some further insights into the waveguide microscopy method, this section will briefly describe alternative methods in its vicinity and how they relate.

Nanoparticle tracking analysis

A method where both fluorescence and scattering signals are commonly used for nanoparticle characterization is NTA, where the size of nanoparticles in suspension is probed by tracking their position over time. The principle builds on the fact that the hydrodynamic radius of a particle relates to its diffusion coefficient through the, so called, Stokes-Einstein relation[34]. The method is similar to the dynamic light scattering (DLS) method, but with single-particle-resolution. The fact that the method requires mobile particles brings with it some limitations. It is not possible to investigate the temporal evolution of properties for individual particles over time as is possible with surface immobilized particles. It is also complicated to use the signal intensity for quantitative analysis due to signal fluctuations related to particle movement. This challenge has been addressed in various ways, for instance through limiting statistics[144] or by convex lens-induced confinement (CLiC) microscopy[145]. The latter builds on the idea of confining individual particles to a small volume in which they are homogeneously illuminated but still mobile enough for tracking analysis. It is an open question whether this method can be extended from fluorescence microscopy to using light scattering. This principle relates to the concepts utilized in flow cytometer-based scattering measurements of NPs, which although restricted to short measurement time spans have been show to provide high labels of sensitivity for biological NPs[107, 146]. Another approach to limiting signal fluctuations and extending the time span over which a particle is observed is to confine the particle movement to two dimensions, i.e. to a surface. Using a protocol fully compatible with the waveguide microscopy method of this thesis, this has been demonstrated using TIRF, where the improved accuracy of this approach allowed for an investigation of the relationship between size, number of tethers and the hydrodynamics of particle-surface interactions of vesicles DNA-tethered to an SLB[147].

Interferometric scattering microscopy

An alternative to using the light scattered of a particle directly is to instead make use of how it interferes with that of a reference light field. As implemented in a number of methods this produces a signal proportional to the particle volume and to the reference field[148], instead of the volume-square-dependence of regular scattering microscopy. This significantly improves sensitivity and has allowed for the label-free observation of individual proteins down to a few tens of kilo-Daltons in mass[149]. The currently most common implementation of this principle is interferometric scattering microscopy (iSCAT), where the interferometric signal stems from the interplay of light from a sample and a back reflected reference signal. As with regular scattering microscopy the main challenges of applying this method for investigating various samples relates to reducing the background signal which in this case often consists of backscattering of rough surfaces or fluctuations in the reference light due to various sources of noise. The currently sparse amount of implemented iSCAT setups involving e.g. flow and sample exchange, suggest that this is also not a trivial challenge. iSCAT has, however, recently been combined with NTA[2][150], offering a complementary particle size determination method.

Quantitative interpretation of iSCAT data is often complicated by the fact that the inherent dependence on signal interference makes it highly influenced by the sample location in relation to the reference, usually its z-coordinate above the surface. For instance, quantification of protein binding to a nanoparticle would in many cases entail modeling how the light scattering due to protein binding interferes both with scattering from the underlying

---

[2] Referred to as iNTA.

surface and from the nanoparticle. While waveguide microscopy also has a z-dependence, due to the decaying evanescent field, it is a weaker dependence than for iSCAT and thus more easily modeled or accounted for by use of reference scatterers on the surface.

As a bright-field counterpart to iSCAT, the method of coherent brightfield imaging (COBRI) has been developed[151, 152]. While not reaching the sensitivity levels of iSCAT, it carries advantages e.g. for tracking particles within cells, as it is not disturbed by reflections from interfaces inside a sample[143].

Holographic microscopy

Yet another approach to optical nanoparticle characterization is the use of phase information contained in a signal. Light traveling the same geometrical length but through media of different refractive index will have traveled different optical distances and might thus be out of phase. Combining light having passed through a sample with a reference beam will thus generate an interference pattern from which information on sample refractive index and geometry can be extracted. This approach is referred to as holographic microscopy and has been implemented for characterization of particles near the nanoscale [153, 154]. The signal obtained is approximately the product of the sample volume and refractive index and can thus be used quantitatively. As a bright-field method, it carries limitations due to a large background signal when used to investigate nanoparticles and current quantitative state-of-the-art methods have a limit of detection around 300–400 nm in diameter for polystyrene and silica particles, respectively. Interestingly, this makes the method quite complementary to waveguide scattering microscopy, the signal interpretation of which works well for particles smaller than the wavelength of light but become more complicated when approaching it. Holographic microscopy thus takes over when waveguide scattering microscopy quantification become ambiguous due to interferometric signal decrease, while iSCAT provides superior sensitivity below the detection limit of waveguide microscopy, but suffers from complications with respect to quantitative analysis above 50 nm.

4.1.2 Waveguide chip fabrication

The waveguide chips used in the measurements of papers I-IV were manufactured in the Chalmers nanofabrication cleanroom laboratory in a process involving numerous different tools and methods. Rather than describing the details of each method and protocol, this section will focus on the main ideas behind the fabrication steps and highlight a number of important points to consider during fabrication. More details can be found in paper I-IV, as well as in other publications from our research group[51, 155, 156].

The process described here has been developed with a number of goals in mind. To produce an optical waveguide structure with an evanescent field penetration depth of $\sim 200\,\mathrm{nm}$. To have a cladding material with a refractive index matching that of water. To have a well accessing the waveguide core through the top cladding layer in which aqueous solutions containing biological samples can be placed. To have the surface of the sensing well compatible with standard surface functionalization schemes including self-assembly of supported lipid bilayers.

These goals are mainly achieved through careful choice of materials. This, in turn, creates a number of requirements on which fabrication methods that can be used. The waveguide core is the layer to which the light is coupled and whose surface the biological samples under investigation interact with. Since many protocols used in microscopy investigations of biological samples are developed for glass surfaces, this layer is preferably made of glass or a glass-like material. As discussed in paper I, the material chosen, due to its low surface roughness and thus low background scattering, is spin-on-glass.

In order to act as a waveguide, this core, with a fairly low refractive index of ~ 1.42, needs to be enveloped in a material of lower refractive index, the so-called cladding layers. The cladding material chosen is CYTOP, a fluorinated polymer material with a refractive index of ~ 1.34, which also fulfills the purpose of having a refractive index close to that of the liquid immersed in the sensing well, which in turn provides a symmetric wave propagation in the core and low background scattering at the edge of the well. One of the main challenges of the chip manufacturing is the low compatibility of the organic CYTOP polymer with the inorganic core glass material, since large differences in thermal expansion coefficients easily result in cracks or delamination. A related issue is the low glass transition temperature of CYTOP, approximately $\sim 110\,^{\circ}\mathrm{C}$. Exceeding this temperature after the core deposition on the lower cladding results in crack formation and thus put quite unusual restrictions in terms of temperature on the other processing steps.

The waveguide fabrication process starts with the substrate, the structural foundation to which the other layers of material are added. The substrates used are polished 4" Si (1 0 0) wafers. Of high quality and of relatively low cost, these exhibit the beneficial properties of low surface roughness, high purity and high inter-specimen consistency. Additionally, and of essence when used for laser generated waveguide applications, they exhibit a low auto-fluorescence for the wavelengths used.

Lower cladding

The hydrophobic nature of CYTOP generally results in a low adhesion to substrates. In order to promote adhesion, the substrates were thus, after initial cleaning using the SC-1 standard procedure[3], functionalized using a silanization protocol. More specifically, a mixture of 3-Aminopropyl-triethoxysilane (APTES, $H_2N(CH_2)_3Si(OC_2H_5)_3$), filtered deionized water and ethanol, in the volume ratios 1:25:475 was spin-coated to the substrate which were subsequently baked at $100\,^{\circ}\mathrm{C}$ for three minutes. To this surface, CYTOP CTX-809A P2

---

[3] SC-1, Standard Clean 1, is a commonly used cleaning procedure where a wafer is placed in a solution of 5 parts deionized water, 1 part ammonia water (29 wt%) and 1 part aqueous H_2O_2 (30 wt%)[157]. For new and properly stored wafers, this procedure was, however, found to be unnecessary for the chip fabrication.

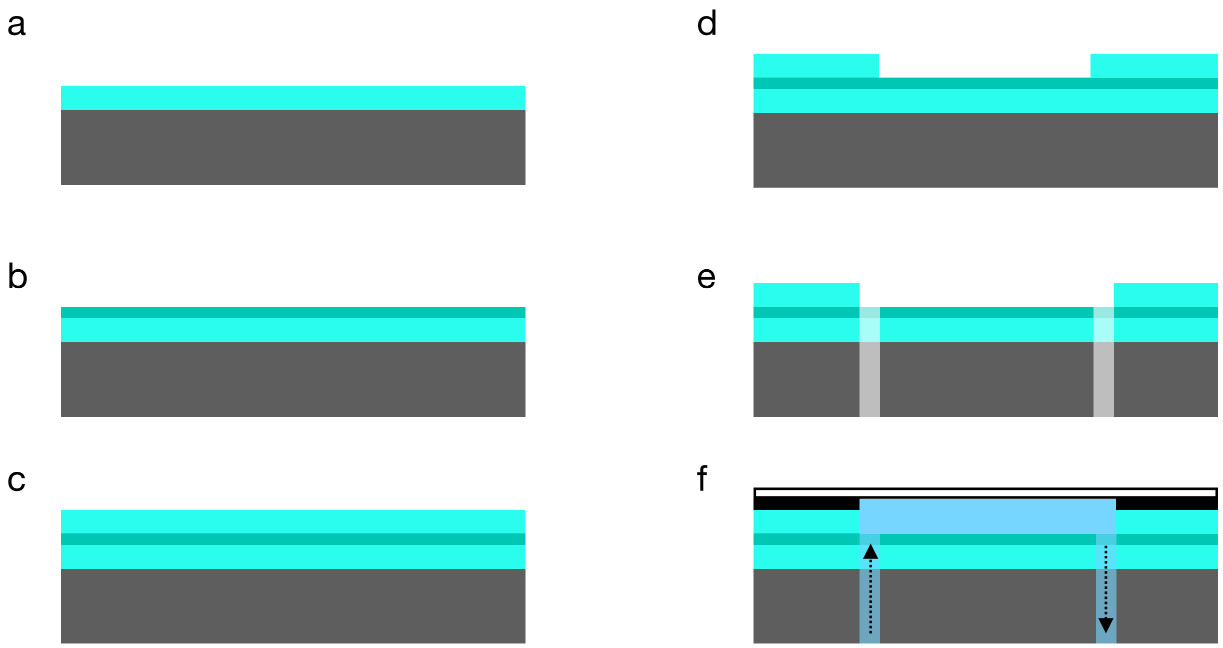

Figure 4.3: Fabrication steps of a waveguide chip on a Si substrate with microfluidics incorporated. a) CYTOP spin-coating and baking. b) Spin-on-glass coating and baking. c) CYTOP spin-coating and baking. d) Reactive-ion etching of the upper cladding to form the sensing well in the CYTOP. e) Etching of inlet and outlet holes through the substrate, core and lower cladding. f) Application of tape and glass to close the flow cell.

was then spin coated, resulting in a 4 µm layer after baking [figure 4.3 a)]. In order to slowly remove gas and bubbles in the CYTOP, thereby ensuring a high surface flatness, the baking was done at an initially low temperature which was slowly ramped to 250 °C.

Core

To, again, overcome the poor adhesive properties of CYTOP, its surface was treated by the deposition and subsequent removal of a thin aluminum layer prior to adding the core material. This procedure has been found to promote adhesion, presumedly through orienting the hydrophilic COOH groups of CYTOP towards the surface[156, 158, 159]. After this surface treatment, spin-on-glass (SOG) was added to the surface using spin coating [figure 4.3 b)]. SOG refers to a class of sol-gel technology for silica deposition through spin coating which, as described in paper I was the glass material investigated found to result in the lowest surface roughness. From this point on, the structure could not be subjected to temperatures above the glass transition temperature of CYTOP of ∼ 110 °C. The baking of the SOG was thus done considerably below the recommended 400 °C, but instead for a longer time than instructed.

Upper cladding

Adding the upper CYTOP cladding layer [fig 4.3 c)] is similar to the procedure for the lower, i.e. APTES functionalization, CYTOP spin coating and baking. The baking is however now ramped to a maximum temperature of 100 °C. The requirements on surface flatness and purity is not quite as strict for this layer since its upper surface is not in contact with the waveguide core.

Sensing well

In order to access the evanescent field at the waveguide core surface, a sensing well is created by removing a part of the upper cladding layer of each chip through photolithography [figure 4.3 d)]. This process consisted of CYTOP surface adhesion promotion by aluminum deposition and removal as described above, after which a photoresist is applied, baked, patterned and developed. The wells were then etched through reactive ion etching using a protocol which combines chemical etching by O_2 plasma and mechanical sputtering by Ar plasma. All steps done at a sub 110 °C temperature. Finally, the wafer was placed in deionized water for neutralization of the highly reactive etched surface.

Dicing

When separating the wafer into individual waveguide sensor chips, two aspects are essential to consider in order to achieve a good chip quality: avoiding contaminating the sensor well surfaces and producing high-quality chip facets. Contaminations on the well surface results in an increased scattering background for the measurements, and smooth chip facets are crucial for a good light coupling into the chip. The debris generated during the dice sawing process used was prevented from reaching the wells by covering the entire wafer surface with a layer of photoresist. Facet quality (e.g. no cracks and no chipping) is governed by a range of parameters, such as saw blade type and quality, blade rotation speed and feed rate. Finding the correct parameters for a specific setup is likely a matter of trial and error.

4.1.3 Waveguide microscopy under flow

Chips fabricated as described above are used paper I and II. A square sensing well, in which a droplet of liquid is placed, is observed using a water immersion objective directly in contact with the droplet. While fully working for a range of interesting applications, this setup carries a number of limitations. The sample droplet will, depending on the ambient temperature, evaporate over time, which affects both its optical properties and the sample concentration within. It is also challenging to change from one sample to another (done using e.g. a pipette) without disturbing the sensitive light coupling by accidentally touching the chip. In order to enable a controlled exchange of liquid over the chip and to allow for measurements under flow, two different microfluidic approaches are used in paper III and IV, respectively. In paper III the fabrication protocol is adapted for used

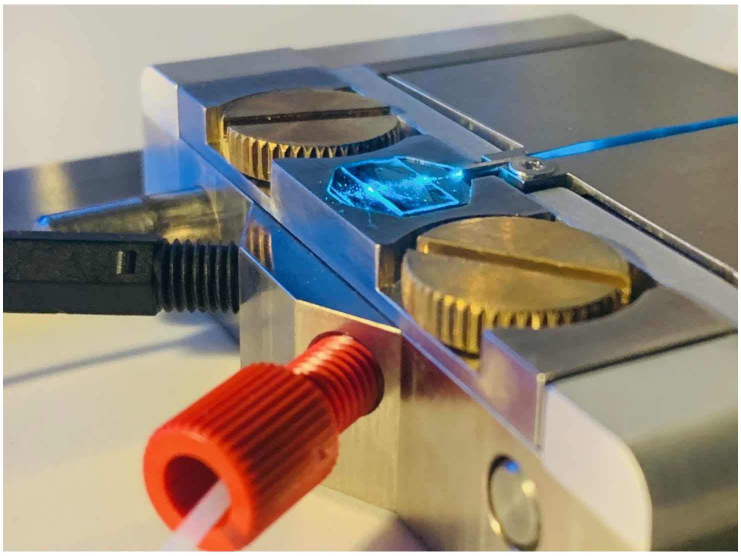

Figure 4.4: Picture of a waveguide chip with an integrated flow cell as implemented in paper IV, placed in the Nanolyze$^{\text{TM}}$ Vision fluid handling and laser coupling system.

with transparent silicon dioxide wafers, making possible to use oil immersion objectives from the chip backside. This allowed for an SU8-based microfluidic flow cell structure to be added above the sensing wells during the chip fabrication procedure. The details of this procedure can be found in paper III.

In an attempt to simplify the rather complicated chip fabrication process of paper III, the measurements in paper IV were done with chips made as described in the sections above, but with one additional step, the etching of inlet and outlet holes, using standard protocols, before the wafer dicing [figure 4.3 e)]. A flow cell structure could then be constructed by applying a custom cut double sided tape over the sensing well to which a thin glass slide was attached [figure 4.3 f)]. This procedure produced chips compatible with the Nanolyze$^{\text{TM}}$ Vision fluid handling and laser coupling system and allowed for pumping sample liquids over the sensing well as desired. The sensor surface could then be observed through the glass slide on top of the flow cell. Figure 4.4 shows a waveguide chip constructed this way, placed in the fluid handling and laser coupling system.

4.2 Surface plasmon resonance sensing

In addition to waveguide microscopy a number of complementary methods have been utilized in this thesis work. One of them is SPR, which provides information on changes in interfacial refractive index near a liquid-metal interface. The defining property of a metal is, I believe most students of physics would explain, the feature of cations in a background of commonly contributed delocalized electrons, or expressed in analogical language, the *electron sea*. These free electrons, or plasma, act as a main mediator of many

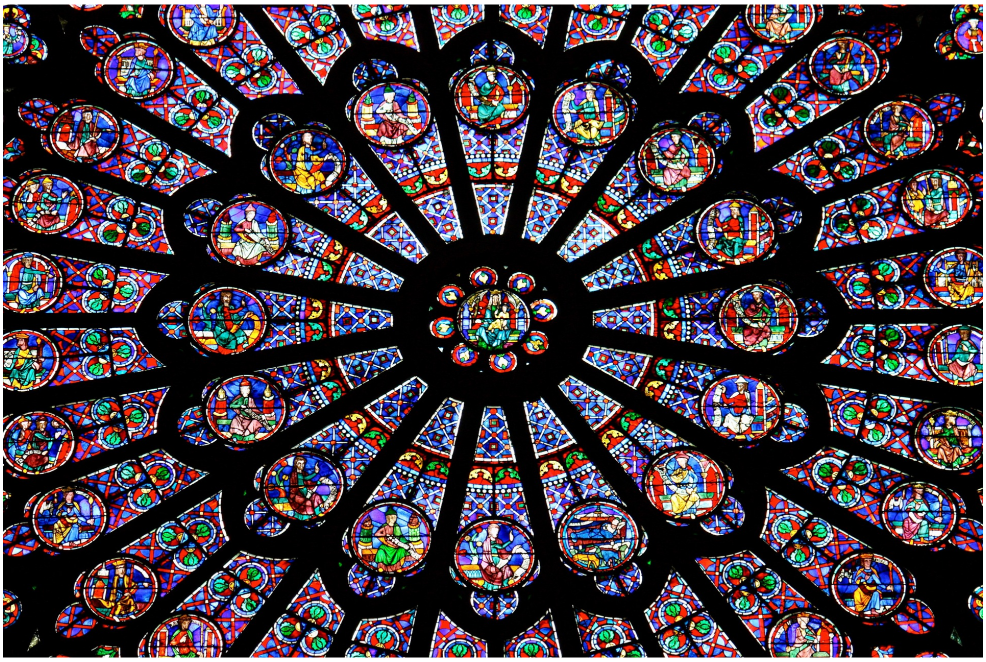

Figure 4.5: Medieval application of localized surface plasmon resonance. Light in certain wavelength intervals is absorbed and scattered by metal nanoparticles in the glass, producing colorful results. Notre-Dame de Paris.

defining properties of this material class, for example its electrical conductivity. Extending the analogy further it is possible to excite waves in the electron sea, so called surface *plasma oscillations* or *surface plasmons*, electron density oscillations which, although the charges are highly confined to the metal surface, generate fields extending into the local environment[160]. The generation of surface plasmons in a metal depends on a set of conditions which, if properly fulfilled, causes an energetic maximum; this occurs at the, so called, resonance conditions. Keeping in mind the existence of other types of plasmonic excitations, such as bulk and wire and localized plasmons[161], the following discussion is restricted to the case of surface plasmon resonance (SPR).

Utilized since at least around 300 AD[162] for fabricating stained glass[4] (see figure 4.5), properly understood in the late 1960s[163, 164] and applied for biosensing purposes since the 1980s[31], the plasmon resonance phenomenon is an intriguing and colorful concept. The principle behind the main bioanalytical technology utilizing this phenomenon, *surface* plasmon resonance builds on the possibility to excite propagating electron density oscillations at a metal-dielectric interface. The field generated from surface plasmons exhibits exponential decay into the local environment and SPR biosensors thus produces a situation similar to the above discussed evanescent field waveguide microscopy method, where analytes are placed in an exponentially decaying field above a surface.

---

[4] Note that this specific application relates to the *localized* surface plasmon resonance phenomenon.

As electrons in a metal surface are driven out of positional equilibrium due to plasmonic excitation, they are subjected to a retrogradely directed force stemming from the oppositely charged cations and mutually repulsive interactions of the equally charged electrons. This is the driving mechanism of the resulting electronic oscillatory behavior, i.e. the plasmons. As theoretically discussed in section 3.3, the refractive index of a medium relates to its extent of electromagnetic field attenuation. An increase in refractive index in the region above a metal surface, for example by the replacement of water with an optically more dense material such as a biomolecular entity, will thus reduce the magnitude of the restoring force felt by the electrons which thus reduces the plasma oscillation frequency. This is the basic principle behind SPR based biosensing. Refractive index variations due to the presence and behavior of biological analytes close to a surface affects the plasmon resonance frequency which, if gauged, thus provides information interpretable in terms of analyte presence, mass, structure and dynamics.

From a technological perspective it is convenient to excite plasmons through the use of light, in particular laser illumination. Generation of SPR at a metal-dielectric interface (in biosensing applications commonly gold-water) through these means is, however, nontrivial due to the need of simultaneous matching of both energy and momentum between the light and surface plasmon[160]. Of the two existing main methods for momentum matching, grating based and prism based, the latter, called the Kretschmann configuration is more common as it allows for more technologically elegant solutions and will be in focus henceforth. In this context, the required momentum matching can be expressed as matching the metal surface parallel components of the laser illumination wavevector incident through the glass prism, $k_{\mathrm{i},x}$, with the surface plasmon wavevector, $k_{\mathrm{sp},x}$.

Under the, for our purposes, reasonable assumptions of typical material properties, metal similar to an electron plasma and non-lossy dielectric (i.e $-\Re(\varepsilon_{\mathrm{d}}) > \varepsilon_{\mathrm{m}}$, $-\Re(\varepsilon_{\mathrm{d}}) \gg \Im(\varepsilon_{\mathrm{d}})$, $\Im(\varepsilon_{\mathrm{m}}) \approx 0$), allows expressing the real part of the propagating plasmon wavevector as:

$$\Re(k_{\mathrm{sp},x}) = \frac{\omega}{c}\sqrt{\frac{\Re(\varepsilon_{\mathrm{d}})\varepsilon_{\mathrm{m}}}{\Re(\varepsilon_{\mathrm{d}}) + \varepsilon_{\mathrm{m}}}} \tag{4.1}$$

where ω is the angular frequency, c the speed of light, ε_{d} the permittivity of the dielectric, ε_{m} the permittivity of the metal[165].

$k_{i,x}$ of illumination incident through the prism with an angle θ can be expressed as[160]:

$$k_{i,x} = \frac{\omega}{c}\sqrt{\varepsilon_g}\sin(\theta) \tag{4.2}$$

In the experimental setup in use in this work, the angle of illumination θ is continuously varied across a chosen interval as the subsequent reflection is observed. As $k_{i,x}$ and $k_{\mathrm{sp},x}$ coincides and surface plasmon resonance excitement occurs, this is manifested as a reflection intensity minimum. The angle θ at which this occurs can be tracked over time, for example

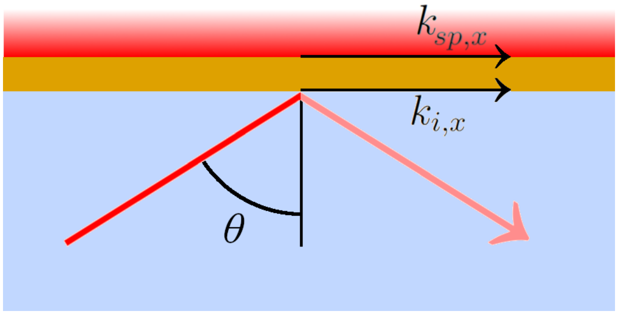

Figure 4.6: The working principles of the surface plasmon resonance sensing method utilized in this work. When the metal surface parallel component of the laser illumination wavevector incident through the glass prism, $k_{i,x}$, coincides with the surface plasmon wavevector, $k_{sp,x}$, SPR excitation occurs. This happens at a certain laser illumination angle θ which is determined by continuously varying the illumination angle and observing the reflection intensity minimum. θ, also referred to as the SPR response R, additionally depends on the refractive index above the sensor surface and can thus be used as a gauge for this parameter. How this response is manifested during the addition of samples of different dimensions and refractive index can be seen in figure 5.11.

as material adheres to the surface, and constitutes a major signal of an SPR measurement (see figure 4.6). This minimum angle is henceforth referred to as the SPR response, R.

The above reasoning on how the SPR response relates to environmental refractive index variations is evident from equation 4.1 which shows that the plasmon wavevector is a function of the dielectric permittivity, ε_d, thus its refractive index ($n_\mathrm{d} = \sqrt{\varepsilon_\mathrm{d}}$).

The instrument in use in this work, the SPR Navi 220A instrument (BioNavis) provides the simultaneous use of two SPR excitation wavelength, in this case 670 nm and 785 nm, allowing for more extensive data analysis. The sensors in use are gold surfaces on glass substrates coated with a thin (10-20 nm) SiO_2 layer in order to allow desired surface chemistry.

The quantitative aims of this work require the interpretation of the SPR response in terms of relevant analyte parameters, i.e. mass and dimensions of entities adhered to the sensor surface. The key bridge between refractive index and mass concentration Γ, as discussed in section 3.3, is the de Feijter's formula:

$$\Gamma = \frac{d_\mathrm{f}(n_\mathrm{f} - n_\mathrm{m})}{\partial n/\partial c} \tag{4.3}$$

with n_f and n_m being the refractive indices of an adhered film and bulk solution, respectively, and d_f the film thickness[115]. Interpretation of the SPR response, R, in terms of refractive index thus provides a route to mass determination. The most straightforward way for this is to assume a linear relationship between R and Δn, an assumption which holds for a small Δn[166], i.e:

$$R_\lambda = S_\lambda(n_{\mathrm{f,eff}} - n_{\mathrm{b}})_\lambda \tag{4.4}$$

where the subscript λ indicates the parameter wavelength dependence, $n_{\mathrm{f,eff}}$ is the effective refractive index of an adhered film, taking the exponentially decaying nature of the plasmon field into account, and S is the SPR instrument sensitivity, a factor describing the signal response per refractive index unit which in practice is determined through calibration measurements with solutions of known refractive index (in this work H_2O- or D_2O-based buffer or glycerol).

Expression of the effective refractive index of an adhered film of refractive index n_{f} and thickness d_{f}[166] enables the following relation:

$$R_\lambda = S_\lambda(n_{\mathrm{f}} - n_{\mathrm{m}})_\lambda \phi(d_{\mathrm{f}},\delta_\lambda) \tag{4.5}$$

With ϕ being a dimensionless parameter accounting for the plasmon field decay:

$$\phi(d_{\mathrm{f}},\delta) = 1 - e^{-d_{\mathrm{f}}/\delta} \tag{4.6}$$

Combining this expression with equation 4.3 provides an expression for the bound mass concentration:

$$\Delta\Gamma = \frac{R_\lambda d_f}{S_\lambda(\partial n_\lambda/\partial c)\phi(d_f,\delta_\lambda)} \tag{4.7}$$

As is evident above, determination Γ requires a value for d_{f}, value which can be obtained from parallel measurements through other instrumentation or circumvented through approximation[167].

A convenient alternative to this approach is the utilization of a second SPR illumination wavelength with the purpose reducing the number of required approximations by determining d_{f} directly from the measured response ratio[32]. This dual-wavelength SPR method exploits the fact that surface plasmons induced by different illumination wavelengths differ in field decay length and thus senses refractive index variations at different depths. As a volume of bulk solution in the vicinity of the sensor surface is replaced by sample, the resulting effective refractive index change of the total sensing volume will differ between wavelengths. This allows for the analysis of sample dimensions/geometry in addition to the conventional mass quantification. Through consideration of the response ratio between the wavelengths, the use of dual wavelengths further eliminates potential inaccuracies due to assumptions on absolute component refractive index values. Since S_λ, the component

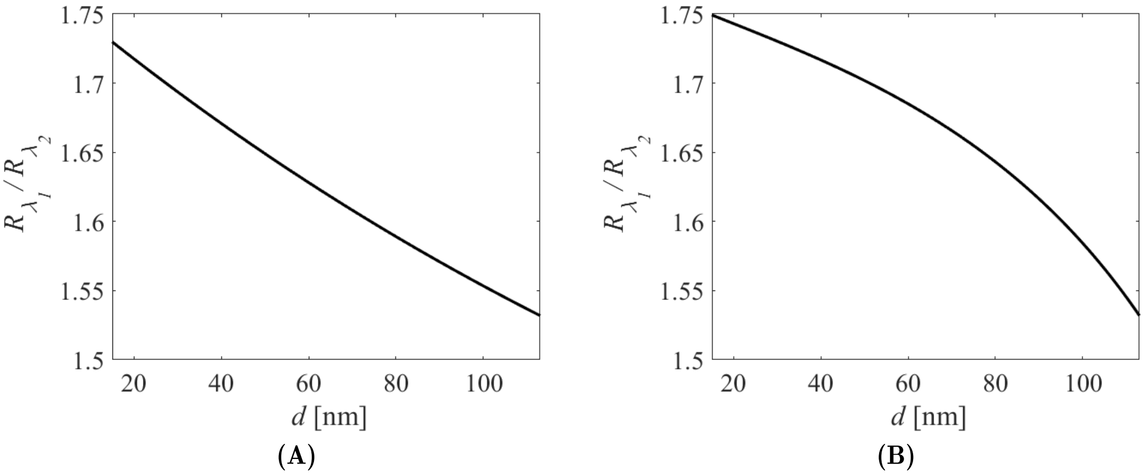

Figure 4.7: The response ratio for $\lambda_1 = 670$ nm and $\lambda_2 = 785$ nm as a function of film thickness d. (a) shows the function for a nondeformed vesicle which has a laterally symmetric mass distribution and thus a ϕ according to equation 4.6. (b) shows the function for a vesicle deformed according to figure 4.8 and thus with a ϕ according to equation 4.9, calculated with a radius $r = 52.5$ nm prior to deformation.

refractive index increments and δ_λ and their wavelength dependencies are known, the simultaneous dual response acquisition, in this case at 670 nm and 785 nm, and consideration of their ratio enables calculating the adsorbed film thickness d_f using the following expression:

$$\frac{R_{670}}{R_{785}} = \frac{S_{670}(\partial n/\partial c)_{670}\phi(d_f,\delta_{670})}{S_{785}(\partial n/\partial c)_{785}\phi(d_f,\delta_{785})} \tag{4.8}$$

where $(\partial n/\partial c)_{670}/(\partial n/\partial c)_{785} \approx 1.02$[168].

This expression is illustrated for a homogeneous film in figure 4.7a), where the response ratio is plotted as a function of the film thickness d_f. A measured R_{670}/R_{785}-value can accordingly be interpreted as a film thickness.

The expressions above, which assumes thin films adhered to the SPR sensor surface, has mathematically been shown to be equal when replacing a homogeneous film with vesicles with a radius $r = d_f/2$, under the assumption of negligible vesicle deformation upon interaction with the underlying surface, i.e. mirror symmetric vesicles along an axis perpendicular to the surface[32]. In situations where this assumption is not valid, such as in paper V, an asymmetric distribution of the vesicle material needs to be considered. A model for this, where vesicles are deformed into truncated spheres but with maintained surface area (see reference[32]), can be implemented by expressing ϕ as:

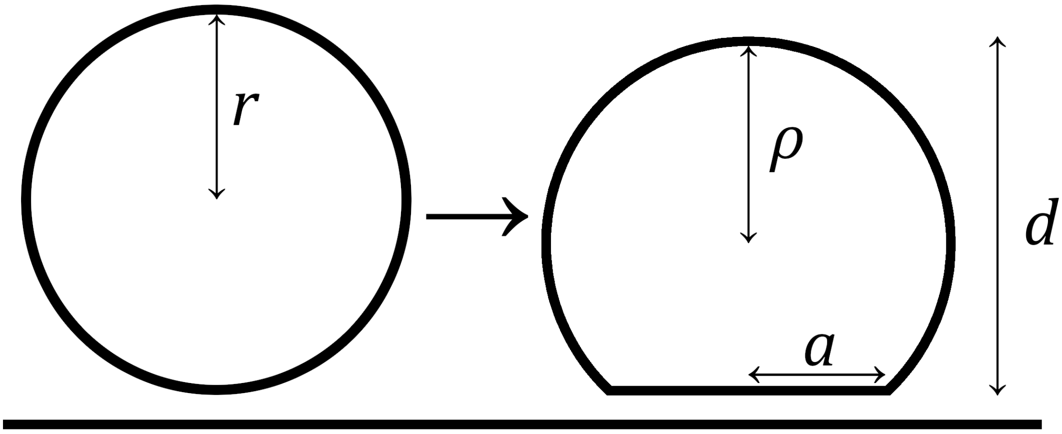

Figure 4.8: Liposome deformation is modeled as a sphere of radius r transitioning to a truncated sphere of radius ρ and footprint radius a while the particle area is preserved. Prior to deformation the liposome lateral dimension, i.e. the thickness as measured using SPR, is simply $2r$, while it after deformation equals d, relating to ρ and a as expressed in equation 4.10.

$$\phi(r,\delta) = [a^2 + 2\delta\rho(1 - \exp\{-(\rho + \sqrt{\rho^2 - a^2})/\delta\})]/2r\delta \tag{4.9}$$

with a and ρ being geometric parameters of the truncated sphere as defined in figure 4.8. These parameters are related to the radius r of the vesicle prior to deformation and the thickness d after deformation according to

$$\rho = \frac{4r^2 + d^2}{4d} \tag{4.10}$$

See paper V for a more thorough discussion on this model. This expression thus allows the expansion of the vesicle thickness determination methodology outlined above to include deformed vesicles.

4.3 Quartz crystal microbalance with dissipation monitoring

Upon the 1959 discovery[169] of a linear relationship between changes in the oscillation frequency response of quartz crystals with mass deposited on its surface, technology exploiting this fact, quartz crystal microbalances, were quickly developed and found use, not least, in layer thickness determination in micro- and nanofabrication[170]. The area of application for this measurement method was significantly expanded from measurement in gas and vacuum to also include aqueous environments with the development of facilitating oscillator circuitry in 1982[171]. This opened the door to the realm of bioanalytical applications where QCM-based technology has occupied its place in the field of label-free ensemble averaged investigations of surface adhered biomolecular compounds.

The method builds on the piezoelectric property of quartz, the fact that physical deformation of the material causes accumulation of electric charge through induced dipole moments, and conversely, that an applied electric field induces deformation. The working principles of QCM-D[170] is built upon the latter through the use of, so called, AT-cut crystals, cut with an 35.25° angle with respect to the optical axis, which upon exposure to an alternating electric field exhibits thickness-shear mode oscillations, i.e. propagating acoustic waves perpendicular to the crystal surface. A quartz crystal will have a set of frequencies, f_n where conditions for resonance are fulfilled. This occurs when the crystal thickness, t_c coincides with an odd number, n, of half wavelengths. The resonance frequency is expressed:

$$f_n = \frac{n v_\mathrm{q}}{2 t_\mathrm{c}} = \frac{n v_\mathrm{q}}{\lambda}, n \text{ odd} \tag{4.11}$$

where v_q is the speed of sound in quartz and λ is the induced wave wavelength.

As described in the foundational Sauerbrey paper[169], a change in adsorbed mass to the quartz crystal surface, Δm induces a resonance frequency shift according to:

$$\Delta m = -\frac{C \Delta f}{n} \tag{4.12}$$

Where $C = 17.7\,\mathrm{ng/Hz\,cm^2}$ for the 5 MHz crystals in use in this work. This expression builds on assumptions of thin, rigid and uniform adsorbed films.

By measuring the dissipation of energy following crystal oscillation excitation, it is possible to draw conclusions on the viscoelastic properties of an adherent.

The assumptions of Sauerbrey are often not fully valid when considering measurements involving biomaterials, which usually results in a mass underestimation. By considering information on resonance frequency shifts in combination with energy dissipation from multiple overtones viscoelastic modeling allows for more accurate results[172].

Another effect of great importance in the context is that of coupling of environmental water to a sample, leading to a mass overestimation in comparison to the sample dry mass[173].

In this thesis QCM-D is utilized as a complement to the waveguide microscopy and plasmon resonance measurements in paper II for confirming the findings on protein binding to lipid vesicles. The Additional Results section of this thesis also contains QCM-D data on ApoE binding to LNPs.

5

Summary of Results

> *"The beauty of science is that all the important things are unpredictable. The optimistic view in me is that nature is designed to make the universe as interesting as possible."*
>
> — Freeman Dyson

THIS SECTION SUMMARIZES the five articles which this thesis is based on. More details are found in the appended articles themselves. The papers are ordered with the aim to illustrate the parallel effort of method development and method utilization that has accompanied this project. **Paper I** has an emphasis on the manufacturing process and characterization of the optical waveguide chip, the core of the waveguide microscopy method. This technology is applied in **paper II** to quantitatively investigate the binding of protein to lipid vesicles through analysis of their light-scattering intensity. These results are additionally compared with measurements using SPR, with the differences and complementarity of the methods emphasized. In **paper III**, the possibilities of the waveguide microscopy method are expanded by developing a fluid handling system. This enables measurements involving controlled exchange of liquids over the sensor surface, e.g. observing processes under flow. **Paper IV** then show how liquid exchange can be utilized to quantify a number of physical properties of lipid nanoparticles, specifically their size, refractive index and how these correlate with fluorescently labeled particle components. Finally, **paper V** describes how the SPR method can be used to investigate nanoparticle deformation and its interplay with multivalent surface interactions, applied to lipid vesicles. Beside its importance as a stand-alone method, it informs the interpretation of the shape sensitive scattering microscopy results in the former four papers.

5.1 Paper I

This paper forms the foundation to a large part of the results presented in this thesis. Here we describe the process of manufacturing a symmetric hybrid organic–inorganic slab waveguide chip, the sensor used in the waveguide microscopy method. One of the main ideas behind this method is to, through careful selection of chip structure and material properties, produce an evanescent light-based illumination system which results in a signal-to-background ratio (SBR) high enough for observing the light scattering signal of individual dielectric nanoparticles.

The aspired SBR is accomplished mainly through two ideas: (1) having the laser illumination and resulting scattering signal decoupled by being perpendicular to each other, in other words that we illuminate from the side but observe from above; (2) that the stray light scattering background is minimized by letting the waveguide cladding layers, in which the sensing well is located, have a refractive index closely matching that of the solutions put in the well, i.e. close to water.

The cladding material chosen is CYTOP, a fluorinated polymer material with a refractive index of ~ 1.34 that through appropriate surface treatments, spin-coating and baking can be applied to a planar surface. Sandwiched between two layers of CYTOP is the waveguide core, a structure which needs to have a higher refractive index, be of high structural and compositional purity and be chemically compatible with standard surface functionalization procedures used in biophysical measurements. In other words, the core should consist of glass or a glass-like material. One of the main challenges with manufacturing these structures is to combine the organic CYTOP polymer with the inorganic core materials, since large differences in thermal expansion coefficients easily results in cracks or delamination. A related issue is the low glass transition temperature of CYTOP, approximately $\sim 110\,^{\circ}\mathrm{C}$. Exceeding this temperature results in crack formation and thus put quite unusual restrictions in terms of temperature on the other processing steps.

Four different core materials were investigated: spin-on-$\mathrm{SiO_2}$, sputtered $\mathrm{SiO_2}$, evaporated $\mathrm{SiO_2}$ and $\mathrm{Si_3N_4}$. With the possibility to tune the core thickness and to choose either $\mathrm{SiO_2}$ or $\mathrm{Si_3N_4}$ as material, it is calculated[1] that the resulting evanescent field penetration depth can be chosen in the $\lesssim 100 - 1000\,\mathrm{nm}$ range.

Waveguide chips made with cladding layers of spin-on-$\mathrm{SiO_2}$ (SOG), the material shown through AFM measurements to have the least surface roughness, were chosen for an in-depth characterization and for a comparison with epi-illumination microscopy to explore the features of waveguide microscopy.

The chip behavior in terms of guided optical mode and light attenuation were shown to be in agreement with expected values. In the former case by comparison with simulations, in the latter by comparison with the literature[174–176]. See figure 5.1 for a visualization of these results.

Fluorescent latex beads bound to the waveguide sensing surface were imaged using regular epi-fluorescence microscopy as well as using scattering (WGS) and fluorescence (WGF) signals acquired through evanescent light illumination (see figure 5.2). Measurements were conducted with varying amounts of particles in solution, i.e. between the observed particles

---

[1] Based on known material dispersion relations and assuming a illumination wavelength of 532 nm.

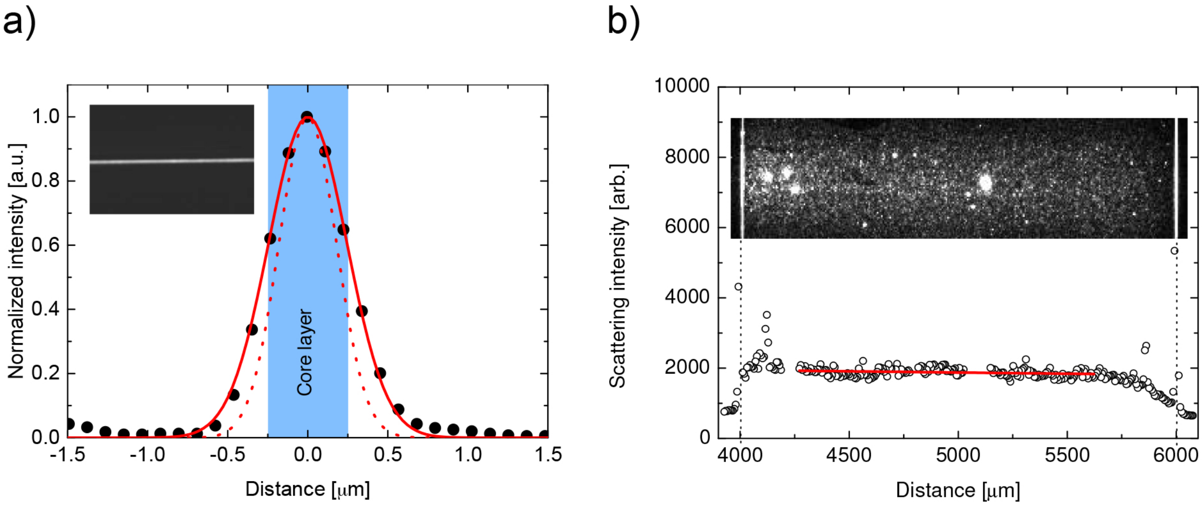

Figure 5.1: Optical characteristics of a hybrid SOG waveguide-chip with 500 nm thick SOG core layer. (a) A micrograph showing a highly confined single mode output obtained at the far side of the waveguide-chip. The filled circles represent the normalized measured intensity profile over the output while the red curves represent the theoretical values before (red dotted line) and after (red solid line) accounting for the finite resolution of the imaging optics (see the article supporting information). The shaded blue area represents the core layer of the waveguide. (b) A micrograph showing the surface scattering from surface-adsorbed 50 nm gold particles in an aqueous environment. The edges of the sensing region are visible as white, high intensity lines 2 mm apart on each side. The graph shows the scattered intensity profile across the chip's sensing area with the red solid line representing an exponential fit to the data.

on the sensor surface and the microscope objective collecting the light. This was done to emulate measurements in complex biological solutions, where it is often necessary to measure in complex particle-dense solution environments. For each mode of observation and each environment, the signals acquired for individual particles were analyzed in terms of SBR and signal-to-noise ratio (SNR). A summary of the results can be seen in figure 5.3. It can be seen that especially for measurements in complex solutions, evanescent light microscopy carries advantages compared to epi-fluorescence microscopy. In large part by illuminating mainly the volume within $\sim$ 110 nm depth from the sensor surface.

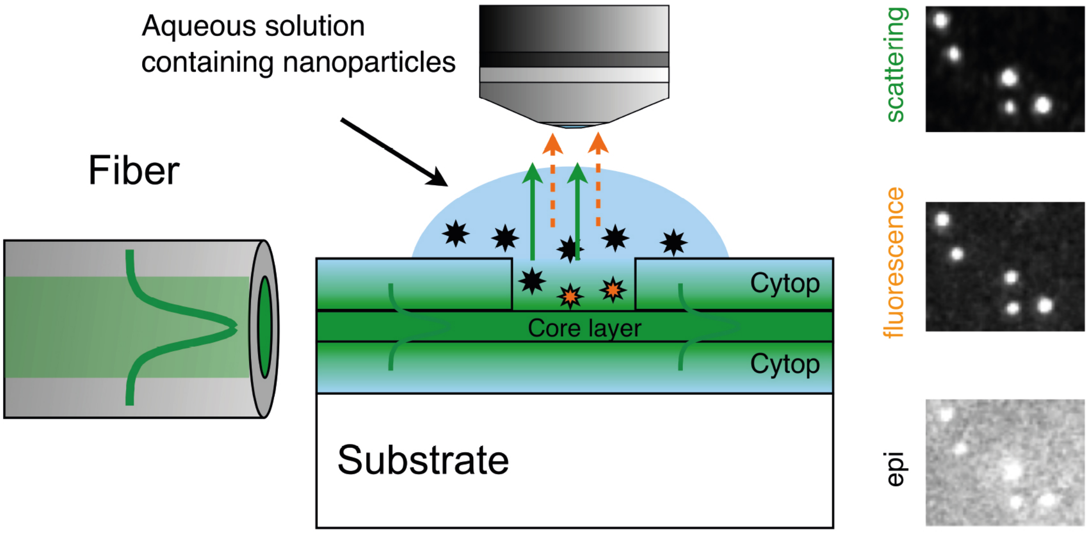

Figure 5.2: Illustration of the waveguide-chip and the measurement scheme. A single mode optical fiber is aligned to the facet of the waveguide and light (green) is coupled into the core layer. An opening is constructed in the upper cladding layer into which a solution containing the specimen of interest is placed. The evanescent light at the interface between the core

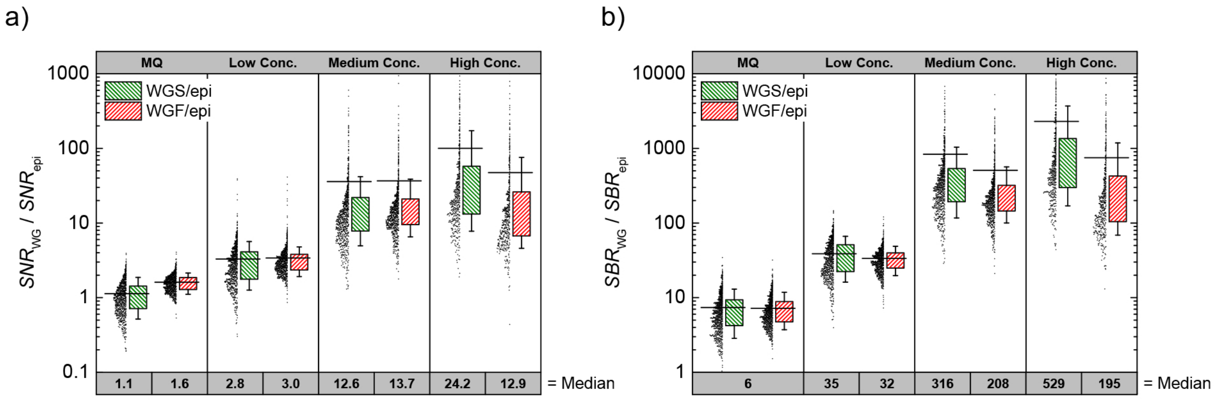

Figure 5.3: Direct comparison between epi and waveguide illumination schemes. (a) SNR ratio and (b) SBR ratio between waveguide illumination and epi-illumination obtained by comparing over 1650 individual surface-adsorbed beads in suspensions containing four different bead concentrations. The whiskers represent the 10%–90% range of the data set, the box 25%–75% range and the horizontal line represents the mean value. The x-axis shows the median of the data.

5.2 Paper II

With the objective of demonstrating the waveguide scattering microscopy method as a quick and reliable, label-free and single-particle-sensitive method for quantification of protein adhesion to biological NPs with potential use in pertinent biological environments, the interaction of biotin binding proteins with biotinylated lipid vesicles was investigated. The interactions between the chosen proteins and biotin are of common use and well-studied and the full system used consists of, in the context of protein film formation, relatively few components[108, 177]. This resulted in a system of relatively low complexity, thus suited for method development. Besides investigations through waveguide scattering microscopy, which simultaneously provided a fluorescence signal, SPR measurements were utilized on the same system for complementary purposes.

An illustration of the biological system studied can be seen in figure 5.4. The purpose was to produce the interaction of interest in this project, a surface presenting vesicles to which fluorescently labeled proteins bound. In order to achieve this final experimental step, a sequence of prior steps was taken:

The experimental procedure consisted of the sequential addition of components to the sensor surfaces, each binding to the previous one, either electrostatically, through cholesterol intercalation into a lipid bilayer, or through the biotin-streptavidin interaction. The final step, in which fluorescently labeled proteins bound to biotinylated vesicles, was the main interest of the measurements. The steps were:

1. After method specific cleaning procedures (detailed in the method section of the paper), the sensor surface was functionalized with PLL-g-PEG. This is a synthetic copolymer which consists of a backbone of poly(L-lysine), a positively charged polymer which serves the purpose of electrostatically binding to a negatively charged substrate, to which side-chains of poly(ethylene glycol) has been grafted. The latter forms a dense polymer brush structure which sterically hinders most nonspecific interactions and passivates the surface. A fraction of the sidechains are biotinylated, and thus the binding target for the subsequent streptavidin. Varying the PLL-g-PEG:PLL-g-PEG-biotin ratio made possible to control the surface concentration of bound material.

2. The subsequent step consisted of adding a highly concentrated solution of streptavidin which bound to all available biotin on the surface and thus enabled the binding of a second biotinylated substance.

3. In order to enable the binding of vesicles, double stranded DNA tethers with one end biotinylated and the other cholesterolated were added to the surface. This produced a surface of cholesterol which could then intercalate into the lipid bilayers of subsequently added vesicles. Using these 30 base pair tethers is an established means of binding[64].

4. Subjecting this surface to a lipid vesicle solution lead to their surface immobilization. In this study, unilamellar vesicles consisting of 95 mol% 1-palmitoyl-2-oleoyl-glycero-

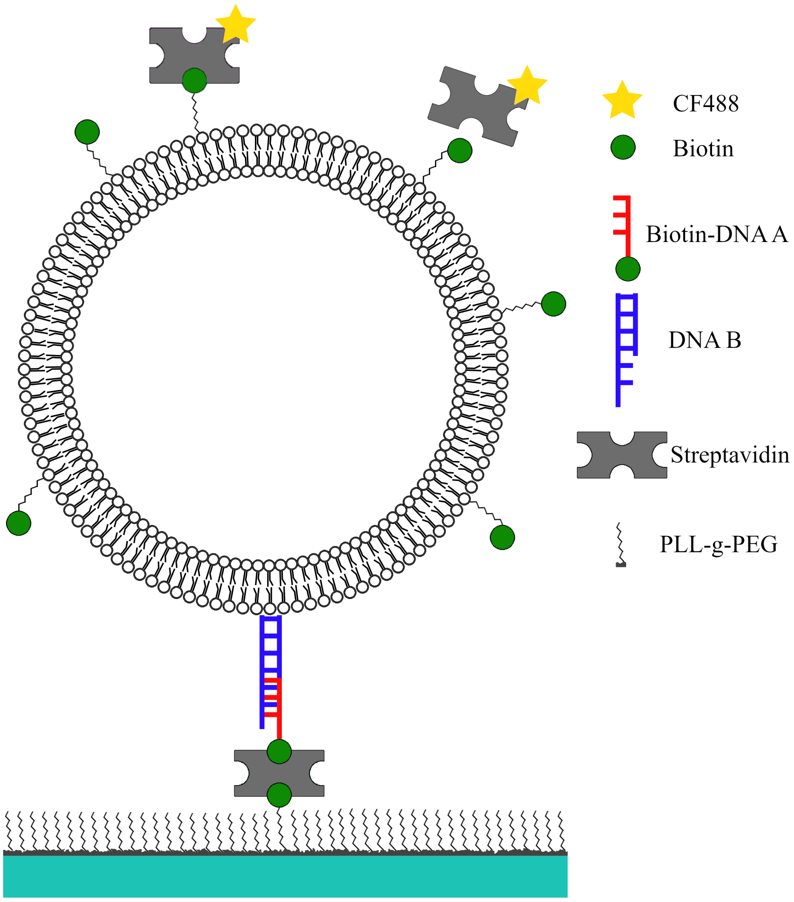

Figure 5.4: Illustration of the system studied. Fluorescently labelled proteins, for example streptavidin, bind to biotinylated vesicles which has been surface immobilized through binding with cholesterolated DNA-tethers, streptavidin and PLL-g-PEG-biotin.

3-phosphocholine (POPC) and 5 mol% 1,2-distearoyl-sn-glycero-3-phosphoethanolamine-N-[biotinyl(polyethylene glycol)-2000] (DSPE-PEG(2000)-biotin of a diameter of approximately 100 nm were used.

5. To the surface bound lipid vesicles, either streptavidin or anti-biotin IgGs labeled with the CF488 fluorophore were added which lead to the formation of a vesicle-adhered protein film. The protein footprint ($\sim 30\,\mathrm{nm}^2$) is large in comparison with the area per biotin in the vesicles.

Observations of the temporal change in scattering and fluorescence intensity during the process of protein binding to the vesicles consistently revealed a signal increase, examples of which can be seen in figure 5.5, both for individual vesicles and as averaged over the approximately 1000 vesicles in the field of view.

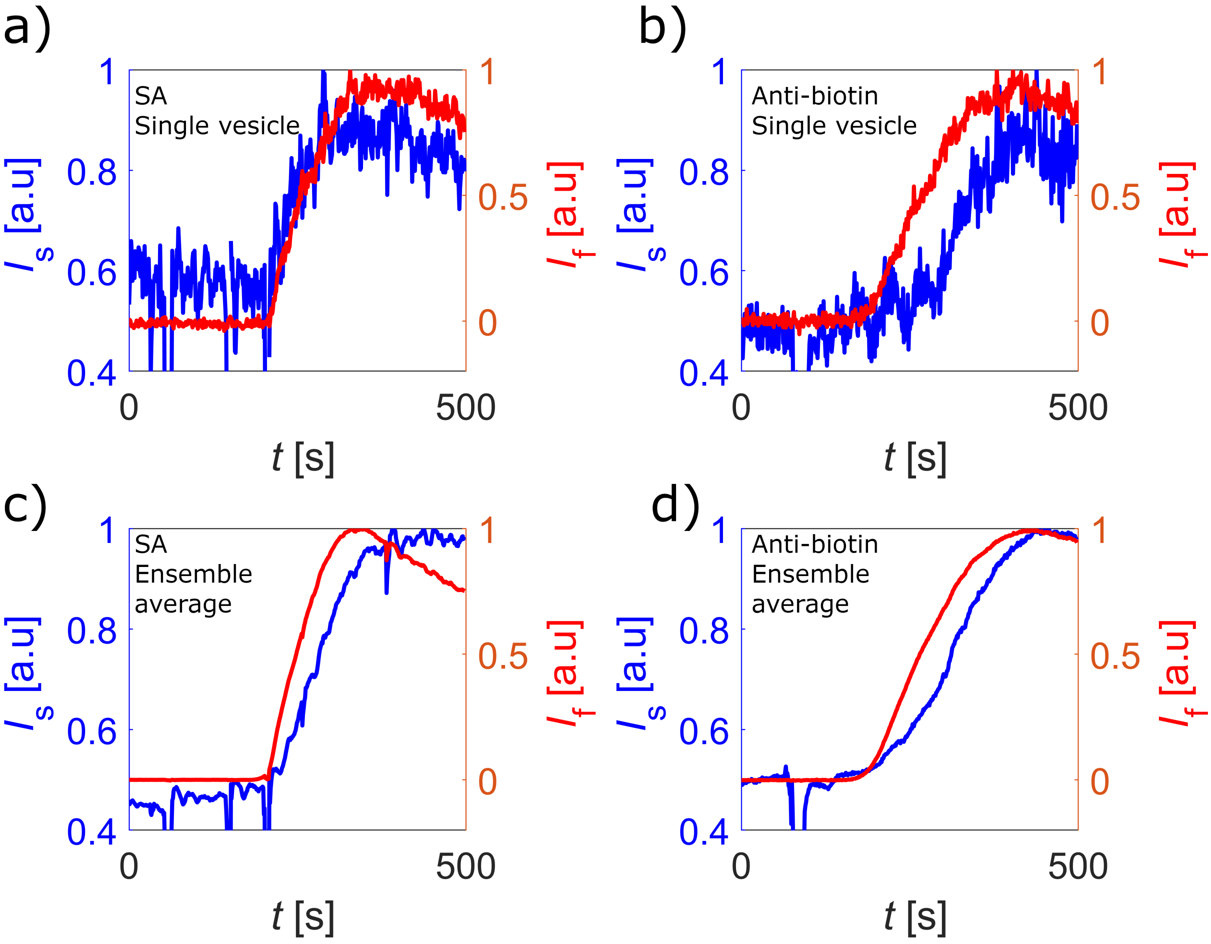

Figure 5.5: Normalized waveguide-microscopy intensities: scattering (blue) and fluorescence (red), as a function of time for vesicles modified with 5 and 3 mol % biotin-lipids upon exposure to (a) and (c) CF488-streptavidin (18 nM) and (b) and (d) CF488-antibiotin (6 nM), respectively. (a) and (b) show the signals for representative single vesicles, and (c) and (d) exhibit the ensemble-averaged signal using around 1700 vesicles in each experiment. Since (a) and (b) represent single vesicle data while (c) and (d) represent average values, the absolute signals differ slightly. The sudden spikes in intensity seen in (c) and (d) are related to liquid injection and/or mixing.

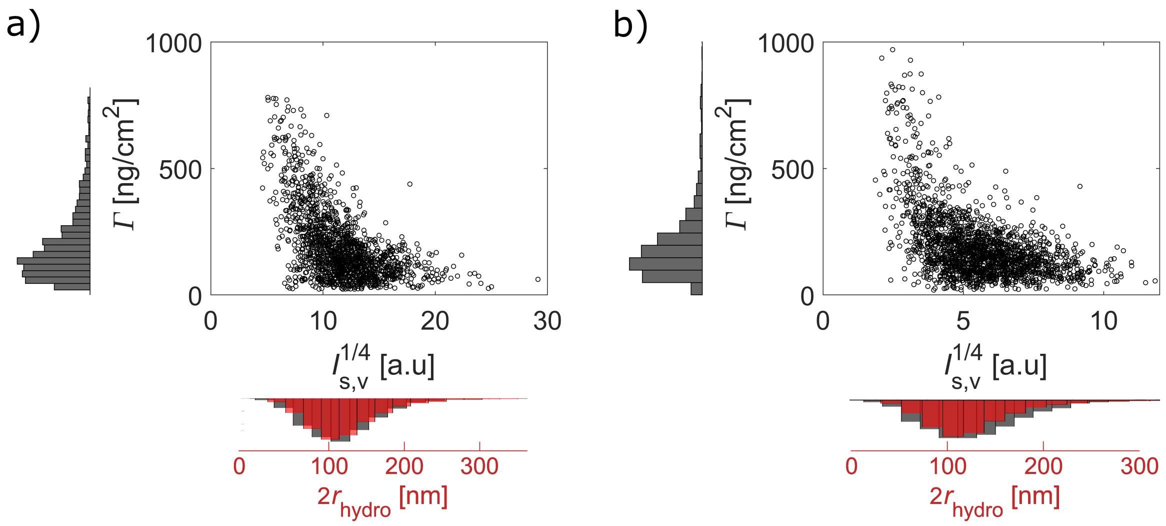

Figure 5.6: Calculated adsorbed protein surface concentration, Γ, expressed in terms of mass per cm^2 of lipid membrane, as a function of the fourth root of the initial vesicle scattering intensity, which is proportional to the vesicle diameter, for (a) streptavidin and (b) antibiotin binding to biotinylated vesicles, with the corresponding distributions projected onto the axes, including the size distribution determined in bulk using NTA plotted together with the distribution in $I_{\mathrm{s,v}}^{1/4}$.

The scattering signal for each individual vesicle can be interpreted as a mass increase due to protein binding as discussed in section 3.5. This revealed an adhered protein layer with an average mass concentration of around 225 ng/cm^2 for streptavidin and 249 ng/cm^2 for anti-biotin and distributions according to figure 5.6, where the mass concentration increase for individual vesicles, Γ is plotted against the fourth root of vesicle scattering intensity prior to protein binding, $I_{\mathrm{s,v}}^{1/4}$, a parameter which roughly scales with the vesicle radius. The results (red histograms) of NTA measurements showing the vesicle hydrodynamic diameter distribution are placed on top of the waveguide microscopy scattering intensity histograms (black) as a comparison. The measured mass concentration values can be compared to that obtained through SPR measurements, 220 and 380 ng/cm^2 for streptavidin and anti-biotin, respectively.

When comparing the results of scattering microscopy and SPR, it is worth noting that in the former case the vesicles are observed at an individual level, which makes possible the analysis of distributions and subpopulations. It also allows for the separation of areas of interest, i.e. the vesicles, from the surrounding surface which in SPR measurements may contribute signal due to unspecific interactions. This background exclusion is an important advantage in comparison with surface sensitive methods solely relying on ensemble average information.

5.3 Paper III

With the aim of extending the utility of the waveguide microscopy technique, this paper presents two major modifications of the chip manufacturing process: (1) using transparent glass substrates instead of the previously used silicon wafers and (2) incorporating a built-in fluid handling system. The performance of these chips were investigated through measurements exploring the correlation between light scattering and fluorescence of surface-immobilized polystyrene beads and measurements on cholera-toxin B protein complex subunit (CTB) binding to G_{M1} modified vesicles. The discussion and interpretation of these results involves extending and evaluating the analytical models used in previous papers[155, 178].

The use of transparent substrates provides the possibility to perform measurements using inverted microscopes, setups where the evanescent field-illuminated samples near the sensor surface are observed from below. Light stemming from a sample thus no longer needs to travel through the solution above before reaching the camera. This carries the advantage of reducing the background and noise levels when measuring in complex biological solutions. Additionally, the enabling of inverted microscope setups allows for the use of high numerical aperture objectives, a possibility which is also explored in the paper.

By incorporating a fluid handling system into the chip design, it was possible to exchange sample or sample environment in a controlled manner. Besides enabling measurements under flow, it significantly simplified measurements by making sample introduction and rinsing more convenient and less time consuming.

In order to gain further insights into how nanoparticles scatter light and fluoresce when illuminated in evanescent fields, three different populations of fluorescent polystyrene beads (with nominal diameters of 52 nm, 100 nm and 188 nm) were adsorbed to the sensor surface. This was done by functionalizing the surface with a mixture of PLL and PLL-g-PEG, of which the former promotes adherence of the negatively charged beads through electrostatic interactions while the latter suppresses adsorption through steric hindrance. Varying the PLL:PLL-g-PEG ratio thus enabled controlling the amount of surface adsorption. These particles contained dye throughout their volume.

Figure 5.7 a) shows a logarithmic representation of how the fluorescence and scattering of these beads relate to each other. Linear fits to the three data clusters reveal the trend that as particle diameter increases, the line slope decreases. The reasons for this is thoroughly discussed both in the paper and in the theoretical section of this thesis (section 3.5). In brief, in a logarithmic plot like this we expect a slope of 2 for an infinitesimal dipole scatterer since its fluorescence intensity scales with the volume and its scattering intensity with the volume squared. As the size of an object approaches the illumination wavelength, two factors will start to play an increasingly significant role: the evanescent field extinction $\eta_{\text{ev.s}}$ and[2] phase related effects η_{RGD}. Figure 5.7 b) shows how the measured data coincides

---

[2] In the case of scattering intensity.

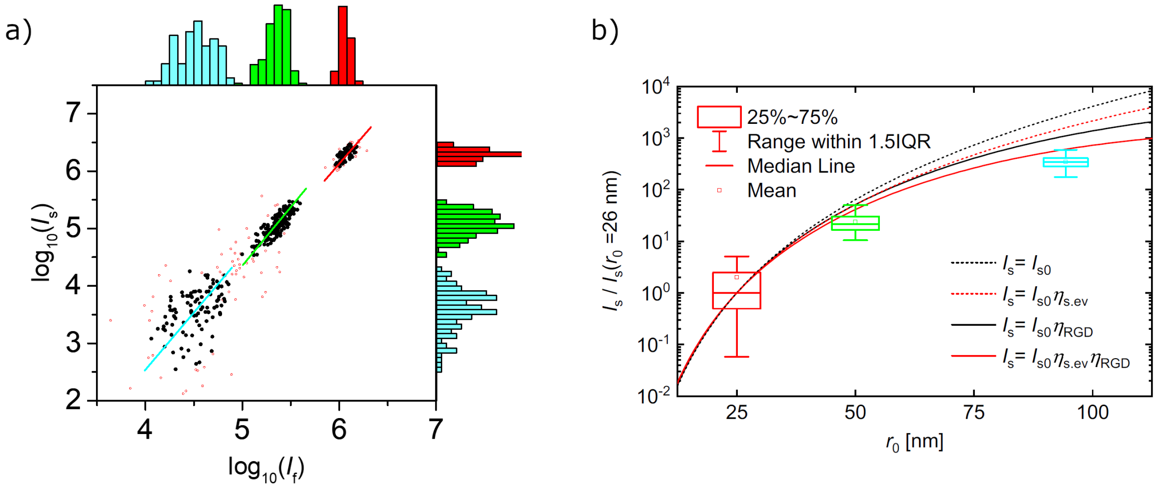

Figure 5.7: a) Logarithmic representation of scattering versus fluorescence intensity obtained with waveguide illumination for three different populations of surface adsorbed fluorescent polystyrene beads (diameter of: 52 nm, 100 nm and 188 nm). The red hollow circles represent excluded data-points that are more than three standard deviations away from the center of a fitted bivariate lognormal distribution of each cluster. The blue, green and red lines are the principal component of the selected data points (black solid circles) of the three observed clusters, with slopes of 1.98, 1.87 and 1.70. The corresponding intensity distributions are projected on each of the axis. b) Scattering intensities from surface adsorbed fluorescent polystyrene beads as a function of their nominal measured nominal radius (26 nm, 50 nm and 94 nm). The intensities have been normalized to the median intensities for the beads obtained for $r_0 = 26$ nm. The data points show the results of measurements while the solid lines represent different adaptions of the proposed analytical models. In a), the models include I_{s0} (black dashed line), $I_{s0}\eta_{\mathrm{ev.s}}$ (red dashed line), $I_{s0}\eta_{\mathrm{RGD}}$ (black solid line), and $I_{s0}\eta_{\mathrm{ev.s}}\eta_{\mathrm{RGD}}$ (red solid line).

with expectations as these factors are taken into account.

The models developed were extended to the case of hollow spherical particles and applied to interpret data on CTB binding to $\mathrm{G_{M1}}$ modified vesicles. CTB is the subunit of the cholera toxin protein complex responsible for binding to the cell membrane (usually, to the ganglioside $\mathrm{G_{M1}}$ molecules there), thus enabling subsequent processes resulting in cholera infection[179]. The vesicles were adsorbed to the sensor surface using PLL-g-PEG-biotin-Neutravidin chemistry as described for paper II after which a solution of fluorescently labeled CTB was introduced. Figure 5.8 a) shows a representative example of the resulting scattering and fluorescence signal increase for a single vesicle. In figure 5.8 b) a histogram of the ratio of the vesicle scattering intensity after and before CTB binding is shown, revealing a modal value of approximately 2.6, a number which under reasonable assumptions can be translated to a CTB protein thickness of around 3 nm. This number agrees well with the literature[180], and thus validates the models here developed for data interpretation.

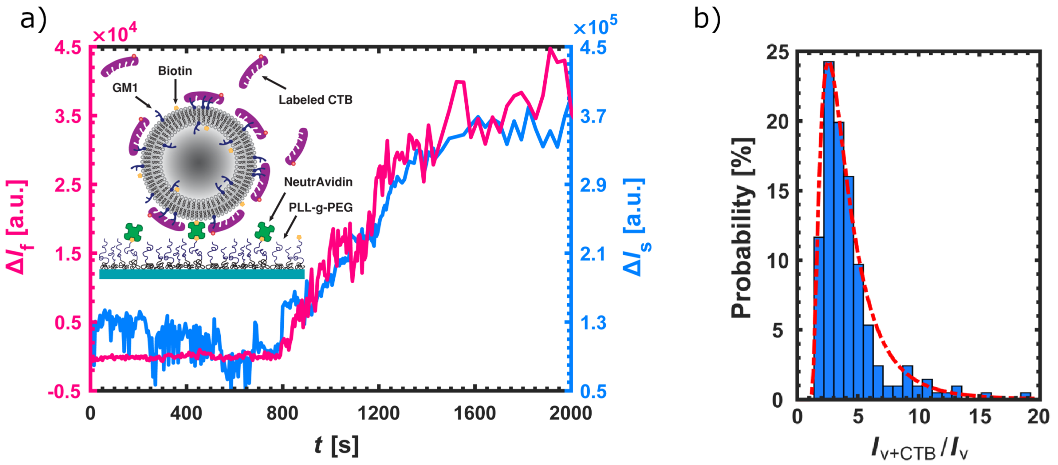

Figure 5.8: a) A representative example of CTB binding to a single POPC vesicle containing 4 mol% G_{M1} acquired simultaneously in fluorescence (red) and scattering (blue) modes. The inset shows a schematic representation of the system. b) Histogram of $\frac{I_{\mathrm{v+CTB}}}{I_{\mathrm{v}}}$ and a fitted lognormal distribution giving a modal value of 2.59.

This paper demonstrates the possibility of using transparent substrate-based waveguide chips with an inverted microscope, the possibility of performing measurements with a built-in fluid handling system and improved mathematical models for data analysis.

5.4 Paper IV

The fourth paper presents an approach to use the single-particle resolution capabilities of the waveguide scattering microscopy method for investigating heterogeneities in nanoparticle samples. By using an integrated liquid exchange system[3], nanoparticle samples together with reference particles could be observed as the surrounding medium refractive index was varied sequentially (see figure 5.9). This, together with a theoretical model for data interpretation, allowed for the extraction of nanoparticle size and refractive index at the level of individual nanoparticles.

The samples chosen for this investigation were lipid nanoparticles, a class of delivery vehicles currently under intense research efforts for their application for nucleic acid-based therapeutics. It has previously been observed that when LNPs, designed for RNA delivery, are taken up by a target cell, only a few percent produce a functional response[88]. It is in this context worthwhile to recall that LNPs are typically prepared using microfluidic assisted rapid mixing precipitation protocols[82, 83], and although the mean diameter can be controlled by varying PEG-lipid content[78], the half-width-half-maximum of the size

---

[3] A different technical solution was used here compared to the one used in paper III. Here, a flow cell was constructed on top of waveguide chips made on non-transparent silicon wafers, see section 4.1.3.

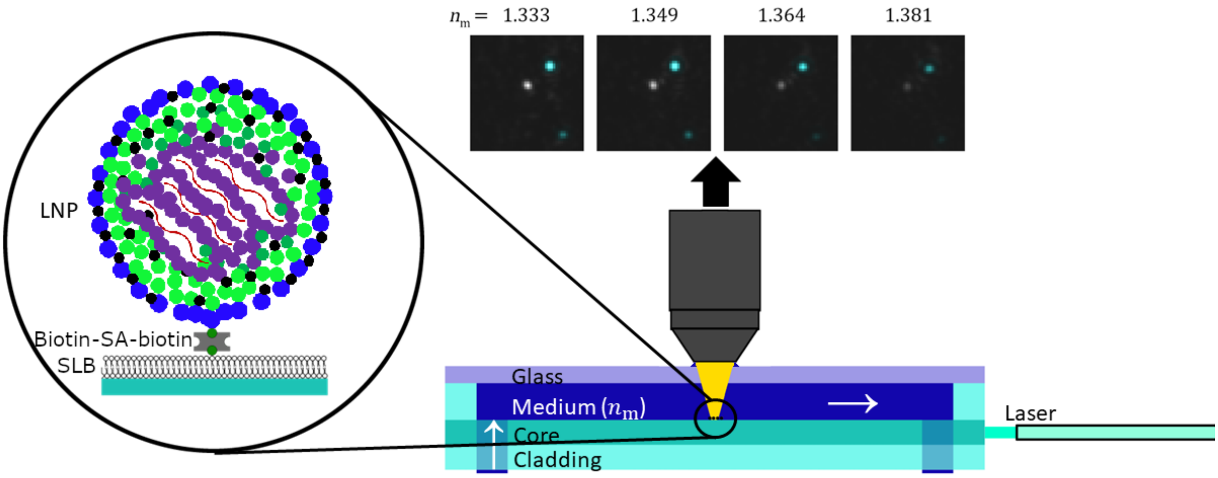

Figure 5.9: Schematic representation of the particle size and RI determination procedure. LNPs (blue) and silica nanoparticles (white) are bound to the waveguide chip sensor surface inside the flow cell. The particles are illuminated by coupling laser light into the waveguide core, generating an evanescent field which produces a light scattering signal from the particles. This signal is observed as the medium refractive index, n_{m}, is varied.

distribution is generally broad, with magnitudes approaching the mean diameter of the LNPs. This suggests that properties other than size could vary within single LNP batches, which can potentially be related to the observed low functional response. Observing sample heterogeneities could thus provide better understanding of these systems and be a route to optimize LNPs for delivery.

The investigated LNPs were bound to an SLB on the waveguide chip sensor surface using biotin-streptavidin chemistry and then subjected to surrounding solutions of different RI by varying concentrations of iodixanol in the buffer solutions. By also having immobilized silica nanoparticles on the sensor surface, serving as references of know size and RI, it was possible to extract the LNP size and RI from the particle scattering signals. Figure 5.10 shows a scatter plot, where the position of each data point indicates the extracted LNP size versus RI an individual particles. The data reveals a mean LNP RI of ~ 1.45 and a trend of lower RI values for larger particles.

Besides having the light scattering signal from the particles, two LNP components: Cy5-labeleld mRNA cargo and rhodamine-labeled DOPE-lipids, provided fluorescence signals. The color coding in figure 5.10 a) and b) shows how the LNP fluorescence intensity for the two respective components is distributed over the size-RI-space by dividing the data into five subpopulations of increasing signal (with the faintest 20% being blue etc.). Based on this data we conclude that the labeled components are likely concentrated in an inner particle core surrounded by a thin shell of unlabeled components, presumable lipids. We additionally note the possibility of structural pockets in the LNPs, permeable to the

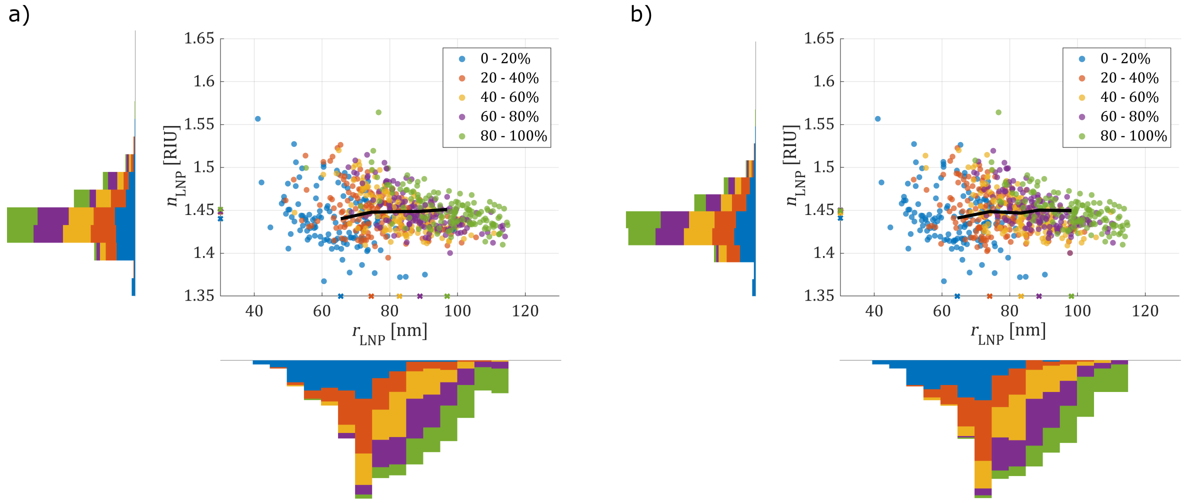

Figure 5.10: Refractive index (n_{LNP}) vs. radius (r_{LNP}) for individual LNPs color-coded according to a) Cy5-mRNA- and b) Rhod-DOPE-content for the LNPs shown in Figs 3 and 4, with corresponding histograms projected onto the respective axes. The LNPs are divided into subpopulations and colored based on their fluorescence intensity, with the faintest 20% being blue etc. The black line indicates how the center of mass of the fluorescence varies with n_{LNP} and r_{LNP}.

surrounding medium which would elicit an RI independent increase in LNP size.

This paper demonstrates the possibility of determining and correlating nanoparticle size and RI with other properties such as fluorescent content, and shows a way towards understanding the potential differences in behavior of heterogeneous nanoparticle populations.

5.5 Paper V

This investigation utilizes two capabilities offered by dual-wavelength SPR, mass quantification and adherent thickness analysis, in order to elucidate the interplay between particle rigidity, ligand density and receptor distribution in a system modelling nanoparticle interactions with the cytosolic membrane. The study focused on liposomes binding to a supported lipid bilayer through the streptavidin-biotin interaction. The processes studied are of interest in the context of e.g. pathogen recognition and initiation of cellular uptake pathways, where polyvalent interactions at the cell membrane is a central concept[181]. Particle rigidity is expected to play a key roll in the cellular uptake process as the energy required for membrane envelopment of a highly deformable entity increases[182].

Two types of liposomes, consisting of either DOPC or DSPC as the main constituent lipid and a fraction of DSPE-PEG(2000)-biotin, were studied while binding to biotinylated SLBs, saturated with streptavidin prior to the liposome addition (see figure 5.11 for an

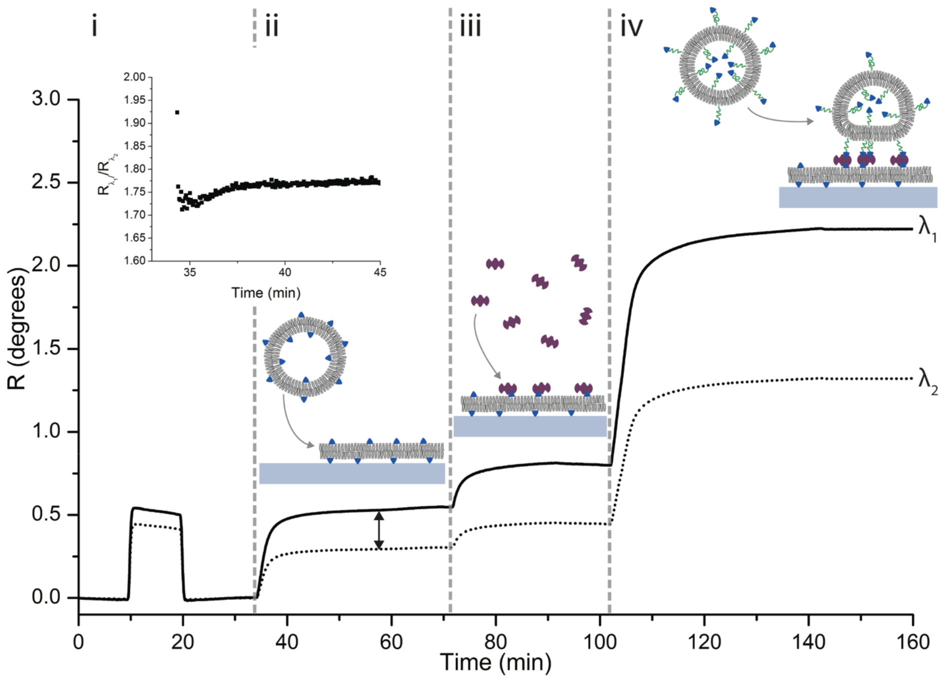

Figure 5.11: Illustration of a typical dual-wavelength SPR measurement with (i) injection of 5 wt% glycerol for calibration purposes, (ii) injection of liposomes and formation of an SLB containing 5 mol% cap biotin ($\Delta\Gamma \sim 345\,\text{ng/cm}^2$), (iii) binding of SA ($\Delta\Gamma \sim 120\,\text{ng/cm}^2$) and (iv) binding of DOPC-PEG-biotin ($\Delta\Gamma \sim 1100\,\text{ng/cm}^2$, $d \sim 77\,\text{nm}$). The inset shows the $R_{\lambda_1}/R_{\lambda_2}$ ratio upon SLB formation plotted vs time used to calibrate the decay lengths.

illustration of the experimental steps). The two liposomes, which at the experimental conditions used exhibited different lipid phase behavior, fluid- and gel phase for the DOPC and DSPC, respectively could be compared in terms of deformation upon interaction with the SLB.

As the liposomes were added to an SLB containing 0.5% biotinylated lipids, liposome coverage were in both cases below the expected jamming limit for random sequential adsorption of spheres to a planar surface (~ 54%), suggesting that the limiting factor for binding is not geometrical saturation of liposomes, but rather the amount of available ligands (streptavidin) on the SLB. This consequently means that all streptavidin were engaged in the binding of liposomes and thus located in the liposome-SLB contact area. Based on measurements of the adsorbed mass of streptavidin and liposomes, it was calculated that on average 100 and 56 streptavidin proteins were bound per liposome for the fluid and gel phase liposomes, respectively. Using the interpretation approach outlined in section 4.2 the dimensions and thus the deformation and the contact area of the liposomes could be calculated (the fluid phase liposomes contracted from 105 nm to 90 nm while the gel phase liposome deformation was negligible) suggesting that the gel phase liposomes had significantly higher concentration of biotinylated lipids in the contact area than possible for immobile lipids. This, in turn, indicates that the DSPE-PEG(2000)-biotin lipids are indeed able to diffuse in both the liposome bilayer in the gel phase liposomes as well as the fluid phase.

Adding the liposomes instead to an SLB containing 5% biotinylated lipids produced liposome coverages close to or above the jamming limit (for fluid and gel-phase liposomes, respectively), suggesting not only the expected possibility of bound liposomes to diffuse on the SLB surface but also that in the gel-phase case, steric hindrance due to reciprocal liposome interaction limits the amount of binding. In these cases liposome deformation from 105 nm to 75 nm and 93 nm for fluid and gel liposomes, respectively were observed. This corresponds to at least ~ 184 and ~ 79 streptavidin engaged in the respective cases, and possibly even higher. Hence, it appears likely that on the SLB, which served to mimic a cellular membrane, the liposome deformation of fluid-phase liposomes is limited by the number of available ligand-receptor bonds while membrane stiffness seems to play a significant role in limiting the deformation of gel-phase liposomes.

In conclusion, the possibility of investigating and potentially disentangling the effects of nanoparticle deformation and interaction valency was demonstrated, while showing that differences in deformability seems to play an important role, worthy of further studies.

6

Additional Results and Future Outlook

The five papers presented in this thesis demonstrate how a number of characterization methods, with a focus on waveguide scattering microscopy and SPR, can be used to gain in-depth information about various nanoparticle properties. Waveguide microscopy is presented as a means for multiparametric single-particle-resolved nanoparticle characterization, where properties such as size, refractive index, fluorescently labeled content and mass variations can be measured and compared. A method is also presented for using dual-wavelength SPR sensing to elucidate the interplay of liposome rigidity, ligand density and receptor distribution upon interaction with a cell-membrane mimic. During the years of working with this project, a range of investigations outside of the scope of the published papers have also been conducted. This section will present results from the most interesting of these measurements, together with some thoughts on possible future developments of the methods and their use.

6.1 Nanoparticle heterogeneity and protein interaction

As described in section 2.3, one of the key processes in the in vivo route of an administered nanoparticle, and thus its efficiency as a drug delivery vehicle, is that of protein corona formation. When considering the papers of this thesis it is clear that a combination of microfluidic controlled measurements as done in papers II, III and IV would offer some interesting possibilities in this context. If the size, refractive index and content characterization procedure of paper IV was combined with an investigation of protein binding as done in paper II and III, single-particle-resolved data on how these parameters correlate could be generated, thus opening a potential way of approaching the paramount questions (e.g. as discussed in the context of LNPs in paper IV) of how batch particle heterogeneity and delivery efficiency relate.

Some preliminary measurements of this kind were in fact conducted on the LNPs investigated in paper IV. After binding LNPs to an SLB on the waveguide sensor as described in the paper, a solution of 25 µg/ml (735 nM) ApoE[1] was injected to the sensor surface.

---

[1] A protein shown to play a crucial role as a corona component for boosting cellular uptake of LNPs[99]

In figure 6.1 a), the recorded variation of LNP scattering intensity over time is shown. The data is sub-grouped based on relative scattering intensity increase, and display a wide spread. In figure 6.1 b) the same subgroups are shown in a log-log plot of scattering vs. mRNA fluorescence intensity. It can be seen that particles that behave similarly upon ApoE exposure, i.e. of the same color in the figure, seem to be spread throughout the sample, and that amount of mRNA does not seem to correlate with disposition for ApoE interaction. As described in papers II and III the scattering intensity can under certain reasonable assumptions be related to bound protein surface mass concentration. Translated into bound mass of ApoE, the particles showing the highest signal increase (green) bind $\sim 250\,\mathrm{ng/cm^2}$ vesicle area. With a molecular weight of 34 kDa, this corresponds roughly to an adhered ApoE monolayer. While a majority of particles show a signal increase, suggesting binding of ApoE, some remain relatively unaltered and a significant fraction of particles lose mass. The same system of SLB bound LNPs exposed to ApoE was investigated using QCM-D [figure 6.1 c)], which showed a net mass increase. The QCM-D frequency data seems to also show three distinct binding phases (labeled i, ii and iii in the figure), speculatively related to the expected time dependent shedding of PEG-lipids from the LNPs[183]. A similar multi-phase behavior can possibly be seen in the scattering data as well, with a second phase beginning around $t = 60$ min. Although more measurements are needed before drawing firm conclusions on these observations, they suggest an interesting application of the single-particle-resolution of the scattering microscopy, where distinct nanoparticle behavior can be related to particle parameters such as size, refractive index or labeled components. For example, could the wide distribution in ApoE binding observed using scattering microscopy be due to differences in PEG shedding from the LNPs, or is it due to structural changes induced upon ApoE binding as previously observed[99] and here confirmed using QCM-D?

Measurements of this kind, enabling a particle parameter of interest (such as disposition for protein interaction) to be correlated with size, RI or content, can help identify approaches for increasing drug delivery efficiency. Systematic investigations using this method, where clusters in parameter scatter plots like figure 6.1 b) are sought, hold the potential of adding important information to the ongoing effort of nanoparticle delivery system development. While improved fabrication methods which produce more homogeneous nanoparticle preparations can be envisioned by improved self-assembly protocols, information of this type would benefit further from sorting protocols making possible to investigate the biological function of different subpopulations. This is challenging from many perspectives, not least the requirement to obtain sufficient yields to perform biological experiments with high enough statistics. Sorting thus represents a key bottleneck that deserves special attention in order to make full use of the multiparametric information obtained with this and complementary methods developed in the field of nanoparticle analytics.

(see section 2.3).

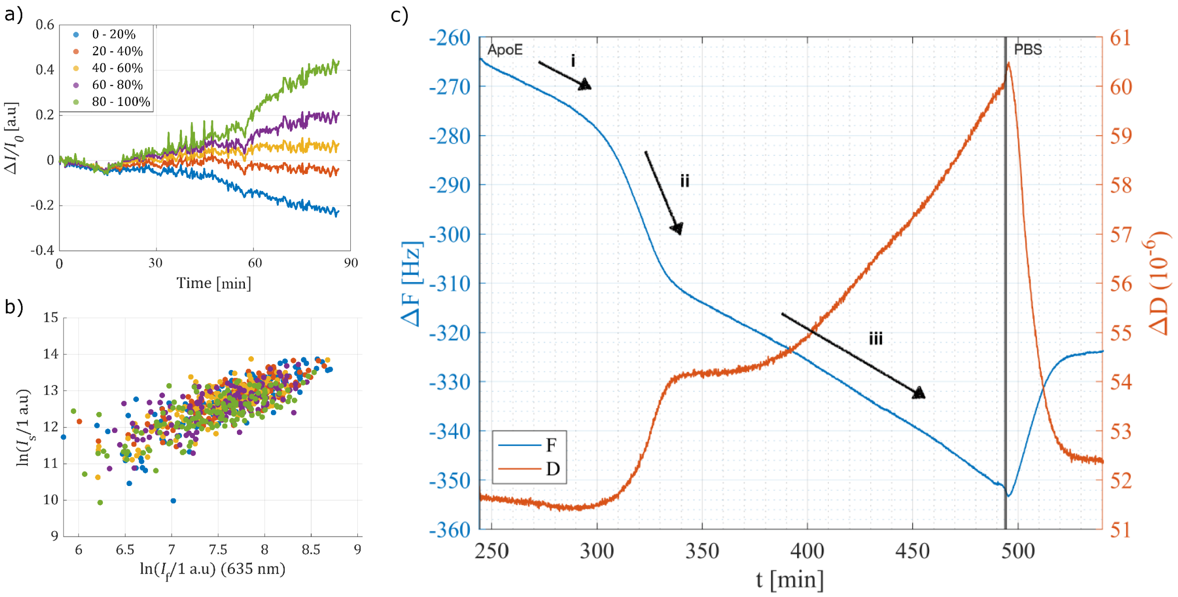

Figure 6.1: a) Normalized average light scattering intensity increase measured with waveguide microscopy vs. time for five subpopulations of surface immobilized LNPs, divided and colored based on relative signal change, as a solution of ApoE is added. The ApoE solution reaches the surface at around $t = 15$ min. b) Log-log plot for the particle scattering intensity prior to ApoE injection vs. fluorescence intensity of the Cy5-mRNA cargo, with the particles colored according to the subpopulation division shown in a). c) QCM-D data on frequency (blue) and dissipation (red) vs. time as LNPs are subjected to ApoE solution and subsequently rinsed in PBS in a system similar to the waveguide measurement shown in a) and b). The binding curve exhibits three phases, labeled i, ii and iii.

6.2 LNP-membrane fusion

LNPs are taken up by a cell via endosomes, and are designed to become electrostatically attracted to the anionic inner lipid bilayer of the endosome as the pH decreases during endosomal processing. If this interaction is sufficiently strong, the LNPs fuse with the endosomal membrane, resulting in release of cargo to the cytosol of the cell. A collaborator investigating the interactions between LNPs and an SLB-based endosomal membrane mimic using TIRF, observed particles appearing to fuse with the SLB upon varying the environmental pH (unpublished). We investigated this system using waveguide microscopy, thus accessing a label-free scattering signal in addition to fluorescence from Cy5-labeled mRNA cargo and rhodamine-labeled lipids present in the LNPs. The results can be seen in figure 6.2 which shows that upon a fusion event, the fluorescence from the Cy5-mRNA remains relatively unaltered, while the scattering signal decreases and the rhodamine-lipid fluorescence signal disappears. This is interpreted as the lipids diffusing out into the SLB while the mRNA remains on the surface, still fluorescing and scattering light. Access to the scattering signal helped excluding the possibility that the particles on the surface did

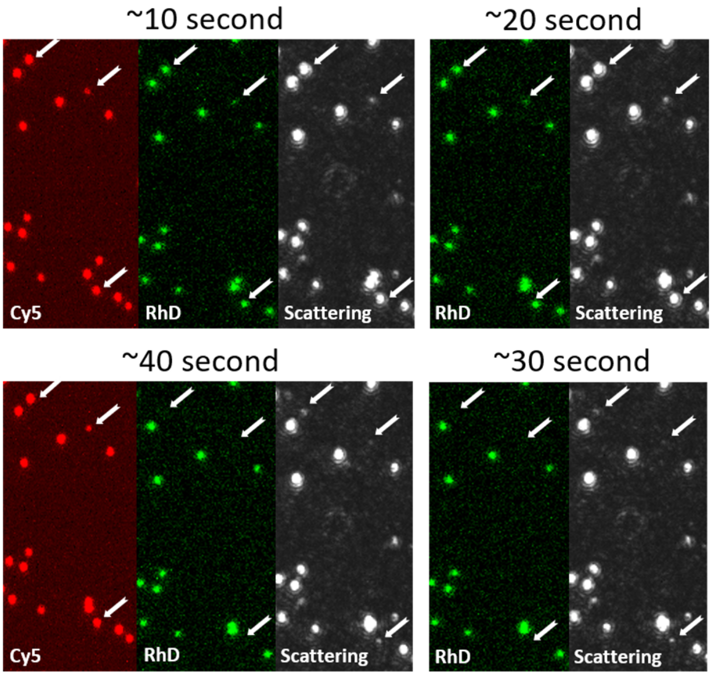

Figure 6.2: Dual-mode fluorescent-scattering microscopy of LNP-membrane fusion events. An SLB formed on glass that prevented the cargo release upon fusion and thus the decrease in the Cy5 signal, while the RhD (lipids) and scattering signal show the collapse of the system upon fusion at 40 seconds. The cargo residue on the surface caused a low scattering signal at the local point of the fusion that is visually appreciable at 40 seconds. Time is approximate.

not fuse but solely exchanged fluorescently labeled lipids with the SLB over time. This investigation is an example of how evanescent-light scattering microscopy can add additional information and contribute understanding inaccessible through fluorescence alone.

TIRF measurements on this system has also been done using a porous silica surface (unpublished), which allows for observing cargo penetrating the membrane by entering the pores. An interesting future direction of the waveguide scattering microscopy platform would be the integration of a similar porous silica surface, on top of the waveguide SOG core. The interaction of the coupled light with a porous silica layer and how this affects the evanescent field would however need to be experimentally and theoretically addressed in order to make quantitative interpretations like those possible on homogeneous planar substrates.

6.3 Nanoparticle mobility

As discussed in section 4.1.1, many nanoparticle characterization methods, such as NTA or DLS, exploit the correlation between particle diffusivity and radius to produce data on particle size by measuring their mobility in three dimensions. As one of the main parameters for nanoparticle classification, accurate size determination for variuos types of samples has remained a topic of interest for a long time and for which new methods are steadily developed[150, 154]. Our research group have contributed to this effort through the development of 2D flow nanometry, a method where particle size is determined from tracking the mobility of particles bound to an SLB under exposure to a constant flow[184]. This approach has been shown to provide a higher accuracy than NTA and DLS, especially when investigating polydisperse samples[147]. As presented in papers II and IV, the technology is now in place for conducting waveguide scattering microscopy under a controlled flow, which thus enables extending the 2D flow nanometry method from TIRF to label-free measurements. This would provide a complementary size-determination approach to the method used in paper IV, where changes in medium RI was used for size determination.

Besides the straight-forward implementation of flow nanometry protocols for the label-free waveguide platform, the possibility to measure particle mobility opens the door to additional novel applications of waveguide microscopy. One example of this comes from observations done while immobilizing LNPs on SLBs during this thesis work. In many measurements investigating LNPs using waveguide microscopy, biotinylated LNPs were bound to a biotinylated SLB with streptavidin as a linker. As particles were bound to the surface they often exhibited an initial mobility, moving across the surface for a distance before becoming stationary. This process is not observed to occur for vesicles, which instead are immediately immobile upon binding. For LNPs, this process was observed to depend on the amount of biotin in the SLB, with a lower amount of biotin in the SLB correlating with a longer mobile phase (see figure 6.3). A particle bound to an SLB is immobile if enough bonds between the two are established. The delay between initial binding and immobilization is thus likely the time it takes to form enough such bonds, an interpretation further supported by a stepwise mobility decrease seen for many particles (data not shown). The reason that this is not observed for lipid vesicles is attributed to the fact that the biotin-lipids in this case have significantly higher mobility than for LNPs. Hidden in this data, there is likely extractable information on the mobility of the biotinylated lipids on the LNP surfaces. Thus, with additional data and analysis it should be possible to demonstrate 1) the ability to measure the mobility of individual nanoparticle components and 2) the possibility to quantify the number of particle-SLB bonds.

6.4 Pushing the limits of detection

In paper II, we used the SNR values for the single-particle-resolved data to estimate the limit of detection for protein binding to vesicles for the waveguide scattering microscopy method. For IgG-antibodies, this number was around 40 proteins. A number of approaches could likely be taken to try to improve this value and further push the limit of detection.

When considering this data, where both the fluorescence and scattering intensities are

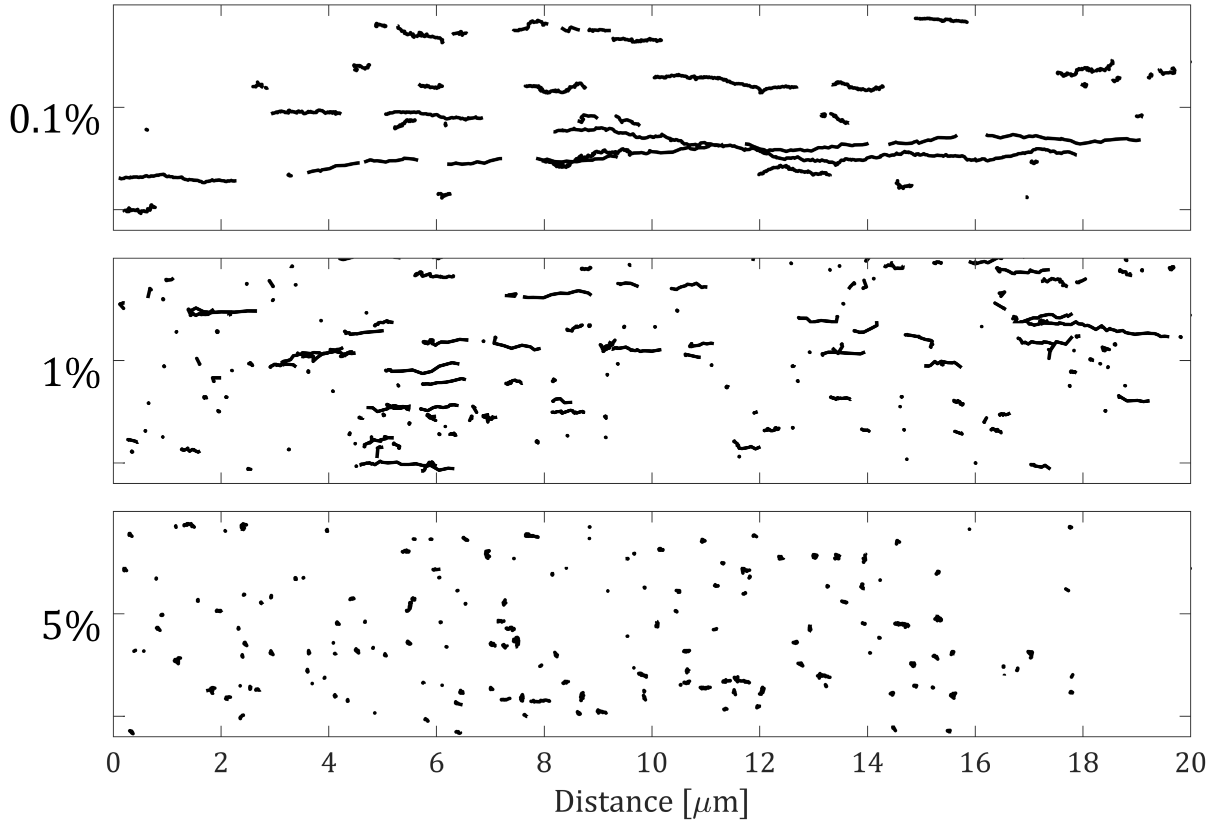

Figure 6.3: Traces of biotinylated LNPs binding to SLBs of increasing biotinylation (to which streptavidin was bound prior to LNP addition) as they bind under flow and eventually become immobile. An increasing biotinylation (0.1-5%) correlates with shorter LNP tracks.

recorded as fluorescent proteins bind to nanoparticles, it is striking how well it would suit training neural networks for label-free detection of weak scattering signals. With the fluorescence as a "ground truth", a network could be trained to detect the very weak scattering signal during the initial phase of binding, stemming form just the first bound proteins. It is possible that a data analysis approach like this could significantly improve the limit of detection.

Besides advanced data analysis approaches, it is worth further investigations how the use of reference particles could benefit scattering microscopy measurements. Adding light-scattering reference structures to the sensor surface, either during the waveguide fabrication or during measurements (e.g. in the form of silica nanoparticles as done in paper IV) could enable reducing both short and long term noise that are due to variations in light-source intensity, light incoupling, vibrations etc. With reference scatterers inert to protein binding, it should be possible to significantly improve the SNR.

6.5 Setup development

There are a number of directions for interesting future development of the waveguide microscopy method used in this work. A feature currently lacking is an integrated solution for temperature control. A simple and user-friendly method of performing measurements at 37 °C would appreciably extend the scope of biophysical investigations possible.

Another interesting possible development is the integration of more advanced microfluidic designs on the waveguide sensing surface. This would open the door to possibilities such as spatial confinement of samples without any sample-surface bonds or the use of very rapid liquid exchange rates.

Recently there has been a number of publications demonstrating the intriguing possibility to combine various super-resolution microscopy methods with waveguide microscopy. This includes super-resolution radial fluctuation microscopy[132], entropy-based superresolution imaging[133] and stochastic optical reconstruction microscopy[133]. An exciting opportunity exists in integrating similar approaches with the refractive-index matched platform in use in this thesis. This way, it would be possible to significantly increase the amount of information extractable from the fluorescence of a sample, thus further complementing the scattering data.

Acknowledgements

I would like to express my sincerest gratitude to everyone which in one way or another has contributed to this thesis.

Fredrik Höök, my main supervisor. Thanks for sharing your knowledge, experience and enthusiasm for science. I really appreciate your style of supervising. Thanks for all insightful comments, guidance and help.

Björn Agnarsson, my co-supervisor. Thanks for all our discussions on experiments and data interpretation. Your ideas, suggestions and engineering skills have been invaluable for this project. Thanks for the many great suggestions which has helped moving this project forwards.

Antonius Armanious, my co-supervisor. Thanks for all your help in the early phases of this PhD project. I admire and am inspired by the rigour and care you put into your research.

Collaborators and co-authors. Thanks for good cooperation. I hope we can continue collaborating in the future. A special thanks to ***Mokhtar Mapar*** for all your help with the waveguide and for good collaboration with papers I and III, and to ***Karin Norling*** for good collaboration on paper V. I would also like to thank ***Erik Olsén*** for the many sudden bursts of theoretical insights you have provided while discussing my data, and for helping me proof-reading this thesis. Thanks also to ***Petteri Parkkila*** for help with the proof-reading. A big thanks also to ***Sara Mohammadi*** for your contribution to this project during your master's thesis work.

Past and present members of the ***Biological Physics group***. Thanks for good cooperation, and for a stimulating, friendly and welcoming working environment. I will miss our interesting, weird and outrageous fika-discussions. A special thanks to my (past and present) ***Office mates*** for making work fun more often than not.

All collaborators in the ***FoRmulaEx team*** and in ***Nanolyze***. Thanks for a collaborative and open environment.

My family and friends, for being just that.

Soli Deo Gloria.

Mattias Sjöberg, Göteborg, August 2022

Bibliography

[1] R. Hooke, *Micrographia.* LONDON, Printed by Jo. Martyn, and Ja. Allestry, Printers to the Royal Society, and are to be sold at their Shop at the Bell in S. Paul's Church-yard. M DC LX V., 1665.

[2] H. Lodish, A. Berk, S. L. Zipursky, P. Matsudaira, D. Baltimore, and J. Darnell, "Microscopy and cell architecture," in *Molecular Cell Biology. 8th edition*, WH Freeman, 2016.

[3] J. James and H. J. Tanke, *Biomedical light microscopy.* Springer Science & Business Media, 2012.

[4] A. Sadana and N. Sadana, *Handbook of biosensors and biosensor kinetics.* Elsevier, 2010.

[5] B. E. Rapp, F. J. Gruhl, and K. Länge, "Biosensors with label-free detection designed for diagnostic applications," *Analytical and bioanalytical chemistry*, vol. 398, no. 6, pp. 2403–2412, 2010.

[6] L. Villarreal-Gómez, A. L. Iglesias, and R. Koprowski, *Biosensors: Current and Novel Strategies for Biosensing.* BoD–Books on Demand, 2021.

[7] X. Fan, I. M. White, S. I. Shopova, H. Zhu, J. D. Suter, and Y. Sun, "Sensitive optical biosensors for unlabeled targets: A review," *analytica chimica acta*, vol. 620, no. 1-2, pp. 8–26, 2008.

[8] S. Stanley, "Biological nanoparticles and their influence on organisms," *Current opinion in biotechnology*, vol. 28, pp. 69–74, 2014.

[9] E. Blanco, H. Shen, and M. Ferrari, "Principles of nanoparticle design for overcoming biological barriers to drug delivery," *Nature biotechnology*, vol. 33, no. 9, p. 941, 2015.

[10] H. A. Rothan and S. N. Byrareddy, "The epidemiology and pathogenesis of coronavirus disease (covid-19) outbreak," *Journal of autoimmunity*, vol. 109, p. 102433, 2020.

[11] M. Hoffmann, H. Kleine-Weber, S. Schroeder, N. Krüger, T. Herrler, S. Erichsen, T. S. Schiergens, G. Herrler, N.-H. Wu, A. Nitsche, *et al.*, "Sars-cov-2 cell entry

depends on ace2 and tmprss2 and is blocked by a clinically proven protease inhibitor," *cell*, vol. 181, no. 2, pp. 271–280, 2020.

[12] G. Chauhan, M. J. Madou, S. Kalra, V. Chopra, D. Ghosh, and S. O. Martinez-Chapa, "Nanotechnology for covid-19: therapeutics and vaccine research," *ACS nano*, vol. 14, no. 7, pp. 7760–7782, 2020.

[13] G. Forni and A. Mantovani, "Covid-19 vaccines: where we stand and challenges ahead," *Cell Death & Differentiation*, vol. 28, no. 2, pp. 626–639, 2021.

[14] X. Hou, T. Zaks, R. Langer, and Y. Dong, "Lipid nanoparticles for mrna delivery," *Nature Reviews Materials*, vol. 6, no. 12, pp. 1078–1094, 2021.

[15] M. Schlich, R. Palomba, G. Costabile, S. Mizrahy, M. Pannuzzo, D. Peer, and P. Decuzzi, "Cytosolic delivery of nucleic acids: The case of ionizable lipid nanoparticles," *Bioengineering & Translational Medicine*, vol. 6, no. 2, p. e10213, 2021.

[16] J. P. Bost, H. Barriga, M. N. Holme, A. Gallud, M. Maugeri, D. Gupta, T. Lehto, H. Valadi, E. K. Esbjorner, M. M. Stevens, *et al.*, "Delivery of oligonucleotide therapeutics: Chemical modifications, lipid nanoparticles, and extracellular vesicles," *ACS nano*, vol. 15, no. 9, pp. 13993–14021, 2021.

[17] M. Tkach and C. Théry, "Communication by extracellular vesicles: where we are and where we need to go," *Cell*, vol. 164, no. 6, pp. 1226–1232, 2016.

[18] R. E. Veerman, G. G. Akpinar, M. Eldh, and S. Gabrielsson, "Immune cell-derived extracellular vesicles–functions and therapeutic applications," *Trends in molecular medicine*, 2019.

[19] K. W. Witwer, E. I. Buzás, L. T. Bemis, A. Bora, C. Lässer, J. Lötvall, E. N. Nolte-'t Hoen, M. G. Piper, S. Sivaraman, J. Skog, *et al.*, "Standardization of sample collection, isolation and analysis methods in extracellular vesicle research," *Journal of extracellular vesicles*, vol. 2, no. 1, p. 20360, 2013.

[20] J. K. Patra, G. Das, L. F. Fraceto, E. V. R. Campos, M. d. P. Rodriguez-Torres, L. S. Acosta-Torres, L. A. Diaz-Torres, R. Grillo, M. K. Swamy, S. Sharma, *et al.*, "Nano based drug delivery systems: recent developments and future prospects," *Journal of nanobiotechnology*, vol. 16, no. 1, pp. 1–33, 2018.

[21] M. J. Mitchell, M. M. Billingsley, R. M. Haley, M. E. Wechsler, N. A. Peppas, and R. Langer, "Engineering precision nanoparticles for drug delivery," *Nature Reviews Drug Discovery*, vol. 20, no. 2, pp. 101–124, 2021.

[22] L. Sercombe, T. Veerati, F. Moheimani, S. Y. Wu, A. K. Sood, and S. Hua, "Advances and challenges of liposome assisted drug delivery," *Frontiers in pharmacology*, vol. 6, p. 286, 2015.

[23] O. S. Fenton, K. N. Olafson, P. S. Pillai, M. J. Mitchell, and R. Langer, "Advances in biomaterials for drug delivery," *Advanced Materials*, vol. 30, no. 29, p. 1705328, 2018.

[24] M. Afsharzadeh, M. Hashemi, A. Mokhtarzadeh, K. Abnous, and M. Ramezani, "Recent advances in co-delivery systems based on polymeric nanoparticle for cancer treatment," *Artificial cells, nanomedicine, and biotechnology*, vol. 46, no. 6, pp. 1095–1110, 2018.

[25] L. S. Arias, J. P. Pessan, A. P. M. Vieira, T. M. T. d. Lima, A. C. B. Delbem, and D. R. Monteiro, "Iron oxide nanoparticles for biomedical applications: A perspective on synthesis, drugs, antimicrobial activity, and toxicity," *Antibiotics*, vol. 7, no. 2, p. 46, 2018.

[26] P. Ghosh, G. Han, M. De, C. K. Kim, and V. M. Rotello, "Gold nanoparticles in delivery applications," *Advanced drug delivery reviews*, vol. 60, no. 11, pp. 1307–1315, 2008.

[27] D. Docter, D. Westmeier, M. Markiewicz, S. Stolte, S. Knauer, and R. Stauber, "The nanoparticle biomolecule corona: lessons learned–challenge accepted?," *Chemical Society Reviews*, vol. 44, no. 17, pp. 6094–6121, 2015.

[28] M. Mammen, S.-K. Choi, and G. M. Whitesides, "Polyvalent interactions in biological systems: implications for design and use of multivalent ligands and inhibitors," *Angewandte Chemie International Edition*, vol. 37, no. 20, pp. 2754–2794, 1998.

[29] H. Metzger, "Transmembrane signaling: the joy of aggregation.," *The Journal of Immunology*, vol. 149, no. 5, pp. 1477–1487, 1992.

[30] P. Vader, E. A. Mol, G. Pasterkamp, and R. M. Schiffelers, "Extracellular vesicles for drug delivery," *Advanced drug delivery reviews*, vol. 106, pp. 148–156, 2016.

[31] B. Liedberg, C. Nylander, and I. Lunström, "Surface plasmon resonance for gas detection and biosensing," *Sensors and actuators*, vol. 4, pp. 299–304, 1983.

[32] D. L. Rupert, G. V. Shelke, G. Emilsson, V. Claudio, S. Block, C. Lässer, A. Dahlin, J. O. Lötvall, M. Bally, V. P. Zhdanov, and F. Höök, "Dual-Wavelength Surface Plasmon Resonance for Determining the Size and Concentration of Sub-Populations of Extracellular Vesicles," *Analytical Chemistry*, vol. 88, no. 20, pp. 9980–9988, 2016.

[33] N.-J. Cho, C. W. Frank, B. Kasemo, and F. Höök, "Quartz crystal microbalance with dissipation monitoring of supported lipid bilayers on various substrates," *Nature protocols*, vol. 5, no. 6, pp. 1096–1106, 2010.

[34] V. Filipe, A. Hawe, and W. Jiskoot, "Critical evaluation of nanoparticle tracking analysis (nta) by nanosight for the measurement of nanoparticles and protein aggregates," *Pharmaceutical research*, vol. 27, no. 5, pp. 796–810, 2010.

[35] L. I. Conrad, M. Neve, V. Nutton, R. Porter, and A. Wear, *The Western medical tradition: 800 BC to AD 1800*, vol. 1. Cambridge University Press, 1995.

[36] G. Ehud and M. Anna, *Plenty of room for biology at the bottom: an introduction to bionanotechnology.* World Scientific, 2013.

[37] A. Schroeder, C. G. Levins, C. Cortez, R. Langer, and D. G. Anderson, "Lipid-based nanotherapeutics for sirna delivery," *Journal of internal medicine*, vol. 267, no. 1, pp. 9–21, 2010.

[38] M.-X. Wu and Y.-W. Yang, "Metal–organic framework (mof)-based drug/cargo delivery and cancer therapy," *Advanced Materials*, vol. 29, no. 23, p. 1606134, 2017.

[39] J. G. Croissant, Y. Fatieiev, A. Almalik, and N. M. Khashab, "Mesoporous silica and organosilica nanoparticles: physical chemistry, biosafety, delivery strategies, and biomedical applications," *Advanced healthcare materials*, vol. 7, no. 4, p. 1700831, 2018.

[40] R. Rupaimoole and F. J. Slack, "Microrna therapeutics: towards a new era for the management of cancer and other diseases," *Nature reviews Drug discovery*, vol. 16, no. 3, p. 203, 2017.

[41] J. Shi, P. W. Kantoff, R. Wooster, and O. C. Farokhzad, "Cancer nanomedicine: progress, challenges and opportunities," *Nature Reviews Cancer*, vol. 17, no. 1, p. 20, 2017.

[42] L. Wang, C. Hu, and L. Shao, "The antimicrobial activity of nanoparticles: present situation and prospects for the future," *International journal of nanomedicine*, vol. 12, p. 1227, 2017.

[43] R. Kalluri and V. S. LeBleu, "The biology, function, and biomedical applications of exosomes," *Science*, vol. 367, no. 6478, 2020.

[44] A. E. Czapar and N. F. Steinmetz, "Plant viruses and bacteriophages for drug delivery in medicine and biotechnology," *Current opinion in chemical biology*, vol. 38, pp. 108–116, 2017.

[45] R. O. Ryan, "Nanobiotechnology applications of reconstituted high density lipoprotein," *Journal of Nanobiotechnology*, vol. 8, no. 1, pp. 1–10, 2010.

[46] D. A. Bricarello, J. T. Smilowitz, A. M. Zivkovic, J. B. German, and A. N. Parikh, "Reconstituted lipoprotein: a versatile class of biologically-inspired nanostructures," *ACS nano*, vol. 5, no. 1, pp. 42–57, 2011.

[47] Y. Liu, P. Bhattarai, Z. Dai, and X. Chen, "Photothermal therapy and photoacoustic imaging via nanotheranostics in fighting cancer," *Chemical Society Reviews*, vol. 48, no. 7, pp. 2053–2108, 2019.

[48] S. M. Dadfar, K. Roemhild, N. I. Drude, S. von Stillfried, R. Knüchel, F. Kiessling, and T. Lammers, "Iron oxide nanoparticles: Diagnostic, therapeutic and theranostic applications," *Advanced drug delivery reviews*, vol. 138, pp. 302–325, 2019.

[49] S. H. Lee and B.-H. Jun, "Silver nanoparticles: synthesis and application for nanomedicine," *International journal of molecular sciences*, vol. 20, no. 4, p. 865, 2019.

[50] G. Maduraiveeran, M. Sasidharan, and V. Ganesan, "Electrochemical sensor and biosensor platforms based on advanced nanomaterials for biological and biomedical applications," *Biosensors and Bioelectronics*, vol. 103, pp. 113–129, 2018.

[51] B. Agnarsson, A. Lundgren, A. Gunnarsson, M. Rabe, A. Kunze, M. Mapar, L. Simonsson, M. Bally, V. P. Zhdanov, and F. Höök, "Evanescent light-scattering microscopy for label-free interfacial imaging: from single sub-100 nm vesicles to live cells," *ACS nano*, vol. 9, no. 12, pp. 11849–11862, 2015.

[52] R. Phillips, J. Kondev, J. Theriot, and H. Garcia, *Physical biology of the cell.* Garland Science, 2012.

[53] B. S. Pattni, V. V. Chupin, and V. P. Torchilin, "New developments in liposomal drug delivery," *Chemical reviews*, vol. 115, no. 19, pp. 10938–10966, 2015.

[54] R. Kanasty, J. R. Dorkin, A. Vegas, and D. Anderson, "Delivery materials for sirna therapeutics," *Nature materials*, vol. 12, no. 11, pp. 967–977, 2013.

[55] T. P. Prakash, M. J. Graham, J. Yu, R. Carty, A. Low, A. Chappell, K. Schmidt, C. Zhao, M. Aghajan, H. F. Murray, *et al.*, "Targeted delivery of antisense oligonucleotides to hepatocytes using triantennary n-acetyl galactosamine improves potency 10-fold in mice," *Nucleic acids research*, vol. 42, no. 13, pp. 8796–8807, 2014.

[56] G. Walsh, "Pharmaceuticals, biologics and biopharmaceuticals," *Biopharmaceuticals: Biochemistry and Biotechnology, 2nd ed. John Wiley & Sons, Inc., Hoboken, NJ*, 2003.

[57] J. A. Kulkarni, D. Witzigmann, S. B. Thomson, S. Chen, B. R. Leavitt, P. R. Cullis, and R. van der Meel, "The current landscape of nucleic acid therapeutics," *Nature Nanotechnology*, vol. 16, no. 6, pp. 630–643, 2021.

[58] H. Lodish, A. Berk, C. A. Kaiser, M. Krieger, M. P. Scott, A. Bretscher, H. Ploegh, P. Matsudaira, *et al.*, *Molecular cell biology.* Macmillan, 2008.

[59] J. Nissen, S. Gritsch, G. Wiegand, and J. Rädler, "Wetting of phospholipid membranes on hydrophilic surfaces-concepts towards self-healing membranes," *The European Physical Journal B-Condensed Matter and Complex Systems*, vol. 10, no. 2, pp. 335–344, 1999.

[60] G. Van Niel, G. d'Angelo, and G. Raposo, "Shedding light on the cell biology of extracellular vesicles," *Nature reviews Molecular cell biology*, vol. 19, no. 4, pp. 213–228, 2018.

[61] R. P. Richter, R. Bérat, and A. R. Brisson, "Formation of solid-supported lipid bilayers: an integrated view," *Langmuir*, vol. 22, no. 8, pp. 3497–3505, 2006.

[62] W. Rawicz, K. C. Olbrich, T. McIntosh, D. Needham, and E. Evans, "Effect of chain length and unsaturation on elasticity of lipid bilayers," *Biophysical journal*, vol. 79, no. 1, pp. 328–339, 2000.

[63] E. Rascol, J.-M. Devoisselle, and J. Chopineau, "The relevance of membrane models to understand nanoparticles–cell membrane interactions," *Nanoscale*, vol. 8, no. 9, pp. 4780–4798, 2016.

[64] I. Pfeiffer and F. Höök, "Bivalent cholesterol-based coupling of oligonucletides to lipid membrane assemblies," *Journal of the American Chemical Society*, vol. 126, no. 33, pp. 10224–10225, 2004.

[65] M. Hope, M. Bally, G. Webb, and P. Cullis, "Production of large unilamellar vesicles by a rapid extrusion procedure. characterization of size distribution, trapped volume and ability to maintain a membrane potential," *Biochimica et Biophysica Acta (BBA)-Biomembranes*, vol. 812, no. 1, pp. 55–65, 1985.

[66] S. G. M. Ong, M. Chitneni, K. S. Lee, L. C. Ming, and K. H. Yuen, "Evaluation of extrusion technique for nanosizing liposomes," *Pharmaceutics*, vol. 8, no. 4, p. 36, 2016.

[67] V. Nele, M. N. Holme, U. Kauscher, M. R. Thomas, J. J. Doutch, and M. M. Stevens, "Effect of formulation method, lipid composition, and pegylation on vesicle lamellarity: a small-angle neutron scattering study," *Langmuir*, vol. 35, no. 18, pp. 6064–6074, 2019.

[68] D. Zucker, D. Marcus, Y. Barenholz, and A. Goldblum, "Liposome drugs' loading efficiency: a working model based on loading conditions and drug's physicochemical properties," *Journal of controlled release*, vol. 139, no. 1, pp. 73–80, 2009.

[69] S. Mura, J. Nicolas, and P. Couvreur, "Stimuli-responsive nanocarriers for drug delivery," *Nature materials*, vol. 12, no. 11, pp. 991–1003, 2013.

[70] D. G. Fatouros and S. G. Antimisiaris, "Effect of amphiphilic drugs on the stability and zeta-potential of their liposome formulations: a study with prednisolone, diazepam, and griseofulvin," *Journal of colloid and interface science*, vol. 251, no. 2, pp. 271–277, 2002.

[71] R. Mezzenga, J. M. Seddon, C. J. Drummond, B. J. Boyd, G. E. Schröder-Turk, and L. Sagalowicz, "Nature-inspired design and application of lipidic lyotropic liquid crystals," *Advanced Materials*, vol. 31, no. 35, p. 1900818, 2019.

[72] J. A. Kulkarni, M. M. Darjuan, J. E. Mercer, S. Chen, R. Van Der Meel, J. L. Thewalt, Y. Y. C. Tam, and P. R. Cullis, "On the formation and morphology of lipid nanoparticles containing ionizable cationic lipids and sirna," *ACS nano*, vol. 12, no. 5, pp. 4787–4795, 2018.

[73] M. Jayaraman, S. M. Ansell, B. L. Mui, Y. K. Tam, J. Chen, X. Du, D. Butler, L. Eltepu, S. Matsuda, J. K. Narayanannair, *et al.*, "Maximizing the potency of sirna lipid nanoparticles for hepatic gene silencing in vivo," *Angewandte Chemie*, vol. 124, no. 34, pp. 8657–8661, 2012.

[74] K. A. Hajj and K. A. Whitehead, "Tools for translation: non-viral materials for therapeutic mrna delivery," *Nature Reviews Materials*, vol. 2, no. 10, pp. 1–17, 2017.

[75] P. S. Kowalski, A. Rudra, L. Miao, and D. G. Anderson, "Delivering the messenger: advances in technologies for therapeutic mrna delivery," *Molecular Therapy*, vol. 27, no. 4, pp. 710–728, 2019.

[76] I. Koltover, T. Salditt, J. O. Rädler, and C. R. Safinya, "An inverted hexagonal phase of cationic liposome-dna complexes related to dna release and delivery," *Science*, vol. 281, no. 5373, pp. 78–81, 1998.

[77] J. Kim, Y. Eygeris, M. Gupta, and G. Sahay, "Self-assembled mrna vaccines," *Advanced drug delivery reviews*, vol. 170, pp. 83–112, 2021.

[78] N. M. Belliveau, J. Huft, P. J. Lin, S. Chen, A. K. Leung, T. J. Leaver, A. W. Wild, J. B. Lee, R. J. Taylor, Y. K. Tam, *et al.*, "Microfluidic synthesis of highly potent limit-size lipid nanoparticles for in vivo delivery of sirna," *Molecular Therapy-Nucleic Acids*, vol. 1, p. e37, 2012.

[79] R. C. Ryals, S. Patel, C. Acosta, M. McKinney, M. E. Pennesi, and G. Sahay, "The effects of pegylation on lnp based mrna delivery to the eye," *PLoS One*, vol. 15, no. 10, p. e0241006, 2020.

[80] K. Knop, R. Hoogenboom, D. Fischer, and U. S. Schubert, "Poly (ethylene glycol) in drug delivery: pros and cons as well as potential alternatives," *Angewandte chemie international edition*, vol. 49, no. 36, pp. 6288–6308, 2010.

[81] H. M. Barriga, M. N. Holme, and M. M. Stevens, "Cubosomes: the next generation of smart lipid nanoparticles?," *Angewandte Chemie International Edition*, vol. 58, no. 10, pp. 2958–2978, 2019.

[82] I. V. Zhigaltsev, N. Belliveau, I. Hafez, A. K. Leung, J. Huft, C. Hansen, and P. R. Cullis, “Bottom-up design and synthesis of limit size lipid nanoparticle systems with aqueous and triglyceride cores using millisecond microfluidic mixing,” *Langmuir*, vol. 28, no. 7, pp. 3633–3640, 2012.

[83] A. K. Leung, Y. Y. C. Tam, S. Chen, I. M. Hafez, and P. R. Cullis, “Microfluidic mixing: a general method for encapsulating macromolecules in lipid nanoparticle systems,” *The Journal of Physical Chemistry B*, vol. 119, no. 28, pp. 8698–8706, 2015.

[84] T. Terada, J. A. Kulkarni, A. Huynh, S. Chen, R. van der Meel, Y. Y. C. Tam, and P. R. Cullis, “Characterization of lipid nanoparticles containing ionizable cationic lipids using design-of-experiments approach,” *Langmuir*, vol. 37, no. 3, pp. 1120–1128, 2021.

[85] K. A. Whitehead, R. Langer, and D. G. Anderson, “Knocking down barriers: advances in sirna delivery,” *Nature reviews Drug discovery*, vol. 8, no. 2, pp. 129–138, 2009.

[86] S. Patel, N. Ashwanikumar, E. Robinson, A. DuRoss, C. Sun, K. E. Murphy-Benenato, C. Mihai, O. Almarsson, and G. Sahay, “Boosting intracellular delivery of lipid nanoparticle-encapsulated mrna,” *Nano letters*, vol. 17, no. 9, pp. 5711–5718, 2017.

[87] M. Y. Arteta, T. Kjellman, S. Bartesaghi, S. Wallin, X. Wu, A. J. Kvist, A. Dabkowska, N. Székely, A. Radulescu, J. Bergenholtz, *et al.*, “Successful reprogramming of cellular protein production through mrna delivered by functionalized lipid nanoparticles,” *Proceedings of the National Academy of Sciences*, vol. 115, no. 15, pp. E3351–E3360, 2018.

[88] J. Gilleron, W. Querbes, A. Zeigerer, A. Borodovsky, G. Marsico, U. Schubert, K. Manygoats, S. Seifert, C. Andree, M. Stöter, *et al.*, “Image-based analysis of lipid nanoparticle–mediated sirna delivery, intracellular trafficking and endosomal escape,” *Nature biotechnology*, vol. 31, no. 7, pp. 638–646, 2013.

[89] J. C. Kaczmarek, P. S. Kowalski, and D. G. Anderson, “Advances in the delivery of rna therapeutics: from concept to clinical reality,” *Genome medicine*, vol. 9, no. 1, pp. 1–16, 2017.

[90] M. J. Munson, G. O’Driscoll, A. M. Silva, E. Lázaro-Ibáñez, A. Gallud, J. T. Wilson, A. Collén, E. K. Esbjörner, and A. Sabirsh, “A high-throughput galectin-9 imaging assay for quantifying nanoparticle uptake, endosomal escape and functional rna delivery,” *Communications biology*, vol. 4, no. 1, pp. 1–14, 2021.

[91] Y. Bao, Y. Jin, P. Chivukula, J. Zhang, Y. Liu, J. Liu, J.-P. Clamme, R. I. Mahato, D. Ng, W. Ying, *et al.*, “Effect of pegylation on biodistribution and gene silencing of

sirna/lipid nanoparticle complexes," *Pharmaceutical research*, vol. 30, no. 2, pp. 342–351, 2013.

[92] N. Dan and D. Danino, "Structure and kinetics of lipid–nucleic acid complexes," *Advances in colloid and interface science*, vol. 205, pp. 230–239, 2014.

[93] C. Corbo, R. Molinaro, A. Parodi, N. E. Toledano Furman, F. Salvatore, and E. Tasciotti, "The impact of nanoparticle protein corona on cytotoxicity, immunotoxicity and target drug delivery," *Nanomedicine*, vol. 11, no. 1, pp. 81–100, 2016.

[94] M. P. Monopoli, D. Walczyk, A. Campbell, G. Elia, I. Lynch, F. Baldelli Bombelli, and K. A. Dawson, "Physical- chemical aspects of protein corona: relevance to in vitro and in vivo biological impacts of nanoparticles," *Journal of the American Chemical Society*, vol. 133, no. 8, pp. 2525–2534, 2011.

[95] C. D. Walkey and W. C. Chan, "Understanding and controlling the interaction of nanomaterials with proteins in a physiological environment," *Chemical Society Reviews*, vol. 41, no. 7, pp. 2780–2799, 2012.

[96] S. Wan, P. M. Kelly, E. Mahon, H. Stockmann, P. M. Rudd, F. Caruso, K. A. Dawson, Y. Yan, and M. P. Monopoli, "The "sweet" side of the protein corona: effects of glycosylation on nanoparticle–cell interactions," *ACS nano*, vol. 9, no. 2, pp. 2157–2166, 2015.

[97] E. Hellstrand, I. Lynch, A. Andersson, T. Drakenberg, B. Dahlbäck, K. A. Dawson, S. Linse, and T. Cedervall, "Complete high-density lipoproteins in nanoparticle corona," *The FEBS journal*, vol. 276, no. 12, pp. 3372–3381, 2009.

[98] S. Milani, F. Baldelli Bombelli, A. S. Pitek, K. A. Dawson, and J. Rädler, "Reversible versus irreversible binding of transferrin to polystyrene nanoparticles: soft and hard corona," *ACS nano*, vol. 6, no. 3, pp. 2532–2541, 2012.

[99] F. Sebastiani, M. Yanez Arteta, M. Lerche, L. Porcar, C. Lang, R. A. Bragg, C. S. Elmore, V. R. Krishnamurthy, R. A. Russell, T. Darwish, *et al.*, "Apolipoprotein e binding drives structural and compositional rearrangement of mrna-containing lipid nanoparticles," *ACS nano*, vol. 15, no. 4, pp. 6709–6722, 2021.

[100] X. Zhu, W. Tao, D. Liu, J. Wu, Z. Guo, X. Ji, Z. Bharwani, L. Zhao, X. Zhao, O. C. Farokhzad, *et al.*, "Surface de-pegylation controls nanoparticle-mediated sirna delivery in vitro and in vivo," *Theranostics*, vol. 7, no. 7, p. 1990, 2017.

[101] E. Casals, T. Pfaller, A. Duschl, G. J. Oostingh, and V. Puntes, "Time evolution of the nanoparticle protein corona," *ACS nano*, vol. 4, no. 7, pp. 3623–3632, 2010.

[102] D. Docter, U. Distler, W. Storck, J. Kuharev, D. Wünsch, A. Hahlbrock, S. K. Knauer, S. Tenzer, and R. H. Stauber, "Quantitative profiling of the protein coronas that form around nanoparticles," *Nature protocols*, vol. 9, no. 9, pp. 2030–2044, 2014.

[103] O. K. Kari, J. Ndika, P. Parkkila, A. Louna, T. Lajunen, A. Puustinen, T. Viitala, H. Alenius, and A. Urtti, “In situ analysis of liposome hard and soft protein corona structure and composition in a single label-free workflow,” *Nanoscale*, vol. 12, no. 3, pp. 1728–1741, 2020.

[104] D. Di Silvio, M. Maccarini, R. Parker, A. Mackie, G. Fragneto, and F. B. Bombelli, “The effect of the protein corona on the interaction between nanoparticles and lipid bilayers,” *Journal of colloid and interface science*, vol. 504, pp. 741–750, 2017.

[105] T. Cedervall, I. Lynch, S. Lindman, T. Berggård, E. Thulin, H. Nilsson, K. A. Dawson, and S. Linse, “Understanding the nanoparticle–protein corona using methods to quantify exchange rates and affinities of proteins for nanoparticles,” *Proceedings of the National Academy of Sciences*, vol. 104, no. 7, pp. 2050–2055, 2007.

[106] O. K. Kari, T. Rojalin, S. Salmaso, M. Barattin, H. Jarva, S. Meri, M. Yliperttula, T. Viitala, and A. Urtti, “Multi-parametric surface plasmon resonance platform for studying liposome-serum interactions and protein corona formation,” *Drug delivery and translational research*, vol. 7, no. 2, pp. 228–240, 2017.

[107] G. C. Brittain, Y. Q. Chen, E. Martinez, V. A. Tang, T. M. Renner, M.-A. Langlois, and S. Gulnik, “A novel semiconductor-based flow cytometer with enhanced light-scatter sensitivity for the analysis of biological nanoparticles,” *Scientific reports*, vol. 9, no. 1, pp. 1–13, 2019.

[108] N. M. Green, “Avidin,” in *Advances in protein chemistry*, vol. 29, pp. 85–133, Elsevier, 1975.

[109] R. Feynman, R. Leighton, and M. Sands, *The Feynman Lectures on Physics, Vol II: Commemorative Issue.* Addison-Wesley, 1989.

[110] E. Hecht, *Optics.* Pearson Education, Incorporated, 2017.

[111] L. Novotny and B. Hecht, *Principles of Nano-Optics.* Cambridge University Press, 2006.

[112] C. Bohren and D. Huffman, *Absorption and Scattering of Light by Small Particles.* Wiley Science Series, Wiley, 2008.

[113] J. R. Lakowicz, *Principles of fluorescence spectroscopy.* Springer science & business media, 2013.

[114] H. Zhao, P. H. Brown, and P. Schuck, “On the distribution of protein refractive index increments,” *Biophysical journal*, vol. 100, no. 9, pp. 2309–2317, 2011.

[115] J. De Feijter, d. J. Benjamins, and F. Veer, “Ellipsometry as a tool to study the adsorption behavior of synthetic and biopolymers at the air–water interface,” *Biopolymers: Original Research on Biomolecules*, vol. 17, no. 7, pp. 1759–1772, 1978.

[116] D. Axelrod, "Cell-substrate contacts illuminated by total internal reflection fluorescence.," *Journal of Cell Biology*, vol. 89, no. 1, pp. 141–145, 1981.

[117] D. K. Cheng *et al.*, *Field and wave electromagnetics.* Pearson Education India, 1989.

[118] R. B. Miles, W. R. Lempert, and J. N. Forkey, "Laser rayleigh scattering," *Measurement Science and Technology*, vol. 12, no. 5, p. R33, 2001.

[119] P. Lilienfeld, "A blue sky history," *Optics and photonics news*, vol. 15, no. 6, pp. 32–39, 2004.

[120] L. Rayleigh, "On the electromagnetic theory of light," *The London, Edinburgh, and Dublin Philosophical Magazine and Journal of Science*, vol. 12, no. 73, pp. 81–101, 1881.

[121] G. A. Niklasson, C. Granqvist, and O. Hunderi, "Effective medium models for the optical properties of inhomogeneous materials," *Applied Optics*, vol. 20, no. 1, pp. 26–30, 1981.

[122] M. Kerker, *The scattering of light and other electromagnetic radiation: physical chemistry: a series of monographs*, vol. 16. Academic press, 1963.

[123] J. K. Hannestad, S. Rocha, B. Agnarsson, V. P. Zhdanov, P. Wittung-Stafshede, and F. Höök, "Single-vesicle imaging reveals lipid-selective and stepwise membrane disruption by monomeric α-synuclein," *Proceedings of the National Academy of Sciences*, 2020.

[124] D. Axelrod, E. H. Hellen, and R. M. Fulbright, "Total internal reflection fluorescence," in *Topics in fluorescence spectroscopy*, pp. 289–343, Springer, 2002.

[125] E. H. Hellen, R. M. Fulbright, and D. Axelrod, "Total internal reflection fluorescence: theory and applications at biosurfaces," in *Spectroscopic Membrane Probes*, pp. 47–79, CRC Press, 2018.

[126] A. N. Weiss, M. A. Bittner, R. W. Holz, and D. Axelrod, "Protein mobility within secretory granules," *Biophysical journal*, vol. 107, no. 1, pp. 16–25, 2014.

[127] D. Axelrod, "Total internal reflection fluorescence microscopy," *Methods in cell biology*, vol. 30, pp. 245–270, 1989.

[128] W. Hickel and W. Knoll, "Optical waveguide microscopy," *Applied physics letters*, vol. 57, no. 13, pp. 1286–1288, 1990.

[129] F. Thoma, U. Langbein, and S. Mittler-Neher, "Waveguide scattering microscopy," *Optics communications*, vol. 134, no. 1-6, pp. 16–20, 1997.

[130] H. Grandin, B. Städler, M. Textor, and J. Vörös, “Waveguide excitation fluorescence microscopy: A new tool for sensing and imaging the biointerface,” *Biosensors and Bioelectronics*, vol. 21, no. 8, pp. 1476–1482, 2006.

[131] A. Hassanzadeh, M. Nitsche, S. Mittler, S. Armstrong, J. Dixon, and U. Langbein, “Waveguide evanescent field fluorescence microscopy: Thin film fluorescence intensities and its application in cell biology,” *Applied Physics Letters*, vol. 92, no. 23, p. 233503, 2008.

[132] A. Priyadarshi, F. T. Dullo, D. L. Wolfson, A. Ahmad, N. Jayakumar, V. Dubey, J.-C. Tinguely, B. S. Ahluwalia, and G. S. Murugan, “A transparent waveguide chip for versatile total internal reflection fluorescence-based microscopy and nanoscopy,” *Communications Materials*, vol. 2, no. 1, pp. 1–11, 2021.

[133] R. Diekmann, Ø. I. Helle, C. I. Øie, P. McCourt, T. R. Huser, M. Schüttpelz, and B. S. Ahluwalia, “Chip-based wide field-of-view nanoscopy,” *Nature Photonics*, vol. 11, no. 5, pp. 322–328, 2017.

[134] N. Jayakumar, F. T. Dullo, V. Dubey, A. Ahmad, F. Ströhl, J. Cauzzo, E. M. Guerreiro, O. Snir, N. Skalko-Basnet, K. Agarwal, *et al.*, “Multi-moded high-index contrast optical waveguide for super-contrast high-resolution label-free microscopy,” *Nanophotonics*, 2022.

[135] D. J. Hill, C. W. Pinion, J. D. Christesen, and J. F. Cahoon, “Waveguide scattering microscopy for dark-field imaging and spectroscopy of photonic nanostructures,” *Acs Photonics*, vol. 1, no. 8, pp. 725–731, 2014.

[136] S. Faez, Y. Lahini, S. Weidlich, R. F. Garmann, K. Wondraczek, M. Zeisberger, M. A. Schmidt, M. Orrit, and V. N. Manoharan, “Fast, label-free tracking of single viruses and weakly scattering nanoparticles in a nanofluidic optical fiber,” *ACS nano*, vol. 9, no. 12, pp. 12349–12357, 2015.

[137] S. Jiang, R. Förster, M. Plidschun, J. Kobelke, R. F. Ando, and M. A. Schmidt, “Three-dimensional spatiotemporal tracking of nano-objects diffusing in water-filled optofluidic microstructured fiber,” *Nanophotonics*, vol. 9, no. 15, pp. 4545–4554, 2020.

[138] K. Leosson and B. Agnarsson, “Integrated biophotonics with cytop,” *Micromachines*, vol. 3, no. 1, pp. 114–125, 2012.

[139] B. Agnarsson, S. Ingthorsson, T. Gudjonsson, and K. Leosson, “Evanescent-wave fluorescence microscopy using symmetric planar waveguides,” *Optics express*, vol. 17, no. 7, pp. 5075–5082, 2009.

[140] H. Ueno, S. Nishikawa, R. Iino, K. V. Tabata, S. Sakakihara, T. Yanagida, and H. Noji, “Simple dark-field microscopy with nanometer spatial precision and microsecond temporal resolution,” *Biophysical journal*, vol. 98, no. 9, pp. 2014–2023, 2010.

[141] J. Ando, A. Nakamura, A. Visootsat, M. Yamamoto, C. Song, K. Murata, and R. Iino, "Single-nanoparticle tracking with angstrom localization precision and microsecond time resolution," *Biophysical journal*, vol. 115, no. 12, pp. 2413–2427, 2018.

[142] G. Byrne, M. Pitter, J. Zhang, F. Falcone, S. Stolnik, and M. G. Somekh, "Total internal reflection microscopy for live imaging of cellular uptake of sub-micron non-fluorescent particles," *Journal of microscopy*, vol. 231, no. 1, pp. 168–179, 2008.

[143] L. Priest, J. S. Peters, and P. Kukura, "Scattering-based light microscopy: From metal nanoparticles to single proteins," *Chemical Reviews*, vol. 121, no. 19, pp. 11937–11970, 2021.

[144] E. Van Der Pol, F. A. Coumans, A. Sturk, R. Nieuwland, and T. G. van Leeuwen, "Refractive index determination of nanoparticles in suspension using nanoparticle tracking analysis," *Nano letters*, vol. 14, no. 11, pp. 6195–6201, 2014.

[145] A. Kamanzi, Y. Gu, R. Tahvildari, Z. Friedenberger, X. Zhu, R. Berti, M. Kurylowicz, D. Witzigmann, J. A. Kulkarni, J. Leung, *et al.*, "Simultaneous, single-particle measurements of size and loading give insights into the structure of drug-delivery nanoparticles," *ACS nano*, vol. 15, no. 12, pp. 19244–19255, 2021.

[146] S. Zhu, L. Ma, S. Wang, C. Chen, W. Zhang, L. Yang, W. Hang, J. P. Nolan, L. Wu, and X. Yan, "Light-scattering detection below the level of single fluorescent molecules for high-resolution characterization of functional nanoparticles," *ACS nano*, vol. 8, no. 10, pp. 10998–11006, 2014.

[147] E. Olsén, S. Jõemetsa, A. González, P. Joyce, V. P. Zhdanov, D. Midtvedt, and F. Höök, "Diffusion of lipid nanovesicles bound to a lipid membrane is associated with the partial-slip boundary condition," *Nano letters*, vol. 21, no. 19, pp. 8503–8509, 2021.

[148] M. Piliarik and V. Sandoghdar, "Direct optical sensing of single unlabelled proteins and super-resolution imaging of their binding sites," *Nature communications*, vol. 5, no. 1, pp. 1–8, 2014.

[149] B. Špačková, H. Klein Moberg, J. Fritzsche, J. Tenghamn, G. Sjösten, H. Šípová-Jungová, D. Albinsson, Q. Lubart, D. van Leeuwen, F. Westerlund, *et al.*, "Label-free nanofluidic scattering microscopy of size and mass of single diffusing molecules and nanoparticles," *Nature Methods*, pp. 1–8, 2022.

[150] A. D. Kashkanova, M. Blessing, A. Gemeinhardt, D. Soulat, and V. Sandoghdar, "Precision size and refractive index analysis of weakly scattering nanoparticles in polydispersions," *Nature methods*, vol. 19, no. 5, pp. 586–593, 2022.

[151] Y.-F. Huang, G.-Y. Zhuo, C.-Y. Chou, C.-H. Lin, W. Chang, and C.-L. Hsieh, "Coherent brightfield microscopy provides the spatiotemporal resolution to study early stage viral infection in live cells," *ACS nano*, vol. 11, no. 3, pp. 2575–2585, 2017.

[152] Y.-F. Huang, G.-Y. Zhuo, C.-Y. Chou, C.-H. Lin, and C.-L. Hsieh, "Label-free, ultrahigh-speed, 3d observation of bidirectional and correlated intracellular cargo transport by coherent brightfield microscopy," *Nanoscale*, vol. 9, no. 19, pp. 6567–6574, 2017.

[153] S.-H. Lee, Y. Roichman, G.-R. Yi, S.-H. Kim, S.-M. Yang, A. Van Blaaderen, P. Van Oostrum, and D. G. Grier, "Characterizing and tracking single colloidal particles with video holographic microscopy," *Optics express*, vol. 15, no. 26, pp. 18275–18282, 2007.

[154] B. Midtvedt, E. Olsén, F. Eklund, F. Höök, C. B. Adiels, G. Volpe, and D. Midtvedt, "Fast and accurate nanoparticle characterization using deep-learning-enhanced off-axis holography," *ACS nano*, vol. 15, no. 2, pp. 2240–2250, 2021.

[155] B. Agnarsson, M. Mapar, M. Sjöberg, M. Alizadehheidari, and F. Höök, "Low-temperature fabrication and characterization of a symmetric hybrid organic–inorganic slab waveguide for evanescent light microscopy," *Nano Futures*, vol. 2, no. 2, p. 025007, 2018.

[156] B. Agnarsson, J. Halldorsson, N. Arnfinnsdottir, S. Ingthorsson, T. Gudjonsson, and K. Leosson, "Fabrication of planar polymer waveguides for evanescent-wave sensing in aqueous environments," *Microelectronic Engineering*, vol. 87, no. 1, pp. 56–61, 2010.

[157] W. Kern, "The evolution of silicon wafer cleaning technology," *Journal of the Electrochemical Society*, vol. 137, no. 6, p. 1887, 1990.

[158] P. Degenaar, B. L. Pioufle, L. Griscom, A. Tbrier, Y. Akagi, Y. Morita, Y. Murakami, K. Yokoyama, H. Fujita, and E. Tamiya, "A method for micrometer resolution patterning of primary culture neurons for spm analysis," *The Journal of Biochemistry*, vol. 130, no. 3, pp. 367–376, 2001.

[159] Y. Grohens, J. Schultz, and R. Prud'Homme, "Pmma conformational changes on γ-alumina powder: influence of the polymer tacticity on the configuration of the adsorbed layer," *International journal of adhesion and adhesives*, vol. 17, no. 2, pp. 163–167, 1997.

[160] A. B. Dahlin, *Plasmonic biosensors: an integrated view of refractometric detection*, vol. 4. Ios Press, 2012.

[161] S. A. Maier, *Plasmonics: fundamentals and applications*. Springer Science & Business Media, 2007.

[162] D. Barber and I. C. Freestone, "An investigation of the origin of the colour of the lycurgus cup by analytical transmission electron microscopy," *Archaeometry*, vol. 32, no. 1, pp. 33–45, 1990.

[163] E. Kretschmann and H. Raether, "Radiative decay of non radiative surface plasmons excited by light," *Zeitschrift für Naturforschung A*, vol. 23, no. 12, pp. 2135–2136, 1968.

[164] A. Otto, "Excitation of nonradiative surface plasma waves in silver by the method of frustrated total reflection," *Zeitschrift für Physik A Hadrons and nuclei*, vol. 216, no. 4, pp. 398–410, 1968.

[165] J. Homola and M. Piliarik, "Surface plasmon resonance (spr) sensors," in *Surface plasmon resonance based sensors*, pp. 45–67, Springer, 2006.

[166] L. S. Jung, C. T. Campbell, T. M. Chinowsky, M. N. Mar, and S. S. Yee, "Quantitative interpretation of the response of surface plasmon resonance sensors to adsorbed films," *Langmuir*, vol. 14, no. 19, pp. 5636–5648, 1998.

[167] D. L. Rupert, C. Lässer, M. Eldh, S. Block, V. P. Zhdanov, J. O. Lotvall, M. Bally, and F. Höök, "Determination of exosome concentration in solution using surface plasmon resonance spectroscopy," *Analytical chemistry*, vol. 86, no. 12, pp. 5929–5936, 2014.

[168] G. E. Perlmann and L. Longsworth, "The specific refractive increment of some purified proteins," *Journal of the American Chemical Society*, vol. 70, no. 8, pp. 2719–2724, 1948.

[169] G. Sauerbrey, "Verwendung von schwingquarzen zur wägung dünner schichten und zur mikrowägung," *Zeitschrift für physik*, vol. 155, no. 2, pp. 206–222, 1959.

[170] A. Janshoff, H.-J. Galla, and C. Steinem, "Piezoelectric mass-sensing devices as biosensors—an alternative to optical biosensors?," *Angewandte Chemie International Edition*, vol. 39, no. 22, pp. 4004–4032, 2000.

[171] S.-Z. Yao and T.-A. Zhou, "Dependence of the oscillation frequency of a piezoelectric crystal on the physical parameters of liquids," *Analytica chimica acta*, vol. 212, pp. 61–72, 1988.

[172] E. Nilebäck, *QCM-D–with focus on biosensing in biomolecular and cellular systems.* Chalmers University of Technology, 2013.

[173] F. Höök, B. Kasemo, T. Nylander, C. Fant, K. Sott, and H. Elwing, "Variations in coupled water, viscoelastic properties, and film thickness of a mefp-1 protein film during adsorption and cross-linking: a quartz crystal microbalance with dissipation monitoring, ellipsometry, and surface plasmon resonance study," *Analytical chemistry*, vol. 73, no. 24, pp. 5796–5804, 2001.

[174] J.-C. Tinguely, Ø. I. Helle, and B. S. Ahluwalia, "Silicon nitride waveguide platform for fluorescence microscopy of living cells," *Optics express*, vol. 25, no. 22, pp. 27678–27690, 2017.

[175] A. Gorin, A. Jaouad, E. Grondin, V. Aimez, and P. Charette, "Fabrication of silicon nitride waveguides for visible-light using pecvd: a study of the effect of plasma frequency on optical properties," *Optics Express*, vol. 16, no. 18, pp. 13509–13516, 2008.

[176] J. Halldorsson, N. B. Arnfinnsdottir, A. B. Jonsdottir, B. Agnarsson, and K. Leosson, "High index contrast polymer waveguide platform for integrated biophotonics," *Optics Express*, vol. 18, no. 15, pp. 16217–16226, 2010.

[177] J. DeChancie and K. Houk, "The origins of femtomolar protein- ligand binding: hydrogen-bond cooperativity and desolvation energetics in the biotin-(strept) avidin binding site," *Journal of the American Chemical Society*, vol. 129, no. 17, pp. 5419–5429, 2007.

[178] M. Sjöberg, M. Mapar, A. Armanious, V. P. Zhdanov, B. Agnarsson, and F. Höök, "Time-resolved and label-free evanescent light-scattering microscopy for mass quantification of protein binding to single lipid vesicles," *Nano Letters*, vol. 21, no. 11, pp. 4622–4628, 2021.

[179] L. d. Haan and T. R. Hirst, "Cholera toxin: a paradigm for multi-functional engagement of cellular mechanisms," *Molecular membrane biology*, vol. 21, no. 2, pp. 77–92, 2004.

[180] N. Ohtomo, T. Muraoka, A. Tashiro, Y. Zinnaka, and K. Amako, "Size and structure of the cholera toxin molecule and its subunits," *Journal of Infectious Diseases*, vol. 133, no. Supplement_1, pp. S31–S40, 1976.

[181] C. Fasting, C. A. Schalley, M. Weber, O. Seitz, S. Hecht, B. Koksch, J. Dernedde, C. Graf, E.-W. Knapp, and R. Haag, "Multivalency as a chemical organization and action principle," *Angewandte Chemie International Edition*, vol. 51, no. 42, pp. 10472–10498, 2012.

[182] H. Gao, W. Shi, and L. B. Freund, "Mechanics of receptor-mediated endocytosis," *Proceedings of the National Academy of Sciences*, vol. 102, no. 27, pp. 9469–9474, 2005.

[183] A. Gallud, M. J. Munson, K. Liu, A. Idstrom, H. M. Barriga, S. Tabaei, N. Aliakbarinodehi, M. Ojansivu, Q. Lubart, J. J. Doutch, *et al.*, "Time evolution of peg-shedding and serum protein coronation determines the cell uptake kinetics and delivery of lipid nanoparticle formulated mrna," *bioRxiv*, 2021.

[184] S. Block, B. J. Fast, A. Lundgren, V. P. Zhdanov, and F. Höök, "Two-dimensional flow nanometry of biological nanoparticles for accurate determination of their size and emission intensity," *Nature communications*, vol. 7, no. 1, pp. 1–8, 2016.